ABSTRACT

Title of Document: HIGH-PERFORMANCE TUBULAR
EVAPORATOR UTILIZING HIGH ASPECT
RATIO MANIFOLD MICROCHANNELS

Vibhash Chandra Jha,
Doctor of Philosophy, 2012

Directed By: Michael Ohadi, Professor
Department of Mechanical Engineering

Heat recovery using absorption chillers has not been economical for small scale applications due to high capital requirements and heavy weight/volume as deterring factors for its expanded use in waste heat-to-cooling applications. Development of advanced, high performance heat and mass exchanger components can significantly improve the competitive edge of heat activated absorption cooling systems, particularly with respect to weight reduction and size/volume of these systems. The main contribution of this thesis is demonstration of a novel high performance micro-grooved evaporator, as well as a solution heat exchanger, for use in a small-scale ammonia-water absorption cooling system. A compact tubular evaporator was developed which uses an innovative manifold/fluid feed system combined with a

micro-grooved evaporator to realize substantially higher (4 to 5 fold) overall heat transfer coefficient of the evaporator; while requiring much less refrigerant charge per ton of cooling, when compared to conventional state of the art systems. The experimentally measured heat transfer coefficients reported in this study are record high, while pressure drops for the given capacity are modest.

Additional contributions of the study included a detailed numerical study of single-stage absorption cycle with multiple cycle design enhancements to identify the controlling system parameters. A single-phase numerical study for manifold microchannel design was carried out to understand the effect of important geometrical parameters in support of design and development of the evaporator. The tubular evaporator was successfully fabricated and tested to the system pressure of 500 psi on the refrigerant-side and was experimentally evaluated with several microgroove surface made of aluminum and nickel alloys, and also with different flow header enhancements using R134a/water pair. For the experiments conducted, the microchannel width was typically in the range of 30-100 µm with a maximum aspect ratio of 10. The refrigerant flow rate was varied within 5-30 g/s and water flow rate was varied within 150-600 ml/s obtaining wide range of cooling capacity between 1- 5 kW for 2-12 °C LMTDs. The overall heat transfer coefficients greater than 20,000 W/m^2-K was obtained which is roughly 4-5 times higher than state of art for given application. A maximum pressure drop of 200 mbars on water-side and 100 mbars on the refrigerant-side was observed at maximum mass flow rates.

An alternative method for the evaporator design was also explored in form of flat plate evaporators which can further provide improved overall heat transfer coefficients. Manifold microchannels were used on both sides of the plates, with the aim to achieve overall heat transfer coefficient greater than 50,000 W/m^2-K.

The new micro-grooved evaporator has the potential to introduce a game-changing evaporative surface, with precise flow delivery and high heat transfer coefficients, driven by a combination of thin film evaporation, as well as convective boiling on the heat transfer surface.

DEVELOPMENT OF TUBULAR EVAPORATOR UTILIZING HIGH ASPECT RATIO MICROCHANNELS

By
Vibhash Chandra Jha

Dissertation submitted to the Faculty of the Graduate School of the
University of Maryland, College Park, in partial fulfillment
of the requirements for the degree of
Doctor of Philosophy
2012

Advisory Committee:
Professor Michael Ohadi, Chair
Professor Marino di Marzo
Associate Professor F. Patrick McCluskey
Associate Professor Bao Yang
Assistant Professor Ebrahim Al Hajri, Co-Advisor and external committee member
Professor Kyu Yong Choi, Dean's Representative

Dedication

To my parents whose constant love and support has always motivated me…

Acknowledgments

First and foremost, I would like to thank Dr. Michael Ohadi for his constant help and encouragement throughout my entire graduate studies. Apart from his valuable guidance, he has been a great mentor and extremely supportive of all my decisions.

I would like to thank Dr. Serguei Dessiatoun for helping me prepare the roadmap for the current research work. He has been a tremendous help in the whole design, fabrication and experimental testing process. The endless discussions, often on a daily basis have greatly enhanced my problem solving skills. I am highly indebted for this experience forever. I would also like to sincerely thank Assistant Professor Dr. Ebrahim Al Hajri for his constant support and continuous interaction on a regular basis. His technical feedback and guidance is appreciated.

I would like to thank Dr. Amir Shooshtari for weekly review of the work and giving valuable feedbacks for improving it.

I am also grateful to my friends at the Smart and Small Thermal Systems Laboratory for providing a fun and enjoyable atmosphere. It was a pleasure to work with Raphael Mandel, Meera Mahadevan, Josh Fody, Harish Ganapathy, Rohit Andhare, Radoslaw Kuzmicki, Chris De Wilder and Ratnesh Tiwari.

And lastly, I am grateful to the Petroleum Institute (United Arab Emirates) for providing the financial support for this project and the Energy Concepts Company (ECC) for their assistance with independent testing of the evaporator used in the current study.

TABLE OF CONTENTS

LIST OF TABLES

LIST OF FIGURES

NOMENCLATURE

$\dot{m}$	Mass flow rate, kg/s
A	Base heat transfer area, m^2
Bo	Boiling number
C	Specific heat Capacity, J/K
COP_{Carnot}	COP of the Carnot Cycle
COP_{VCRS}	COP of vapor compression cycle
D_h	Hydraulic Diameter, m
f	friction coefficient
Gr	Grashof Number
h	Enthalpy at the state point, J
h_w	Water-side heat transfer coefficient, W/m^2-K
L	Total length of the HX Tube , m
m	Total mass at the state point, kg
Nu	Nusselt Number
Pr	Prandtl Number
Q	Cooling capacity, W
Ra	Rayleigh Number
Re	Reynolds number
S	Entropy at the state point, J/K
T	Temperature at the state point, °C
T_H	Higher temperature of the reversible Carnot cycle, °C
T_L	Lower temperature of the reversible Carnot cycle, °C
U	Overall heat transfer coefficient, W/m^2-K
W	Work input, W
We	Weber Number
x	Ammonia fraction at the state point

ACRONYMS

2-d	Two dimensional
abs	absorber
ch	channel
con	condenser
COP	Coefficient of performance
des	desorber
evap	evaporator
fin	Fins for both side of the HX tube
GMS	Grams per second
GPM	Gallons per minute
HTC	Heat Transfer Coefficient
i	HX tube inner
in	input to the system
inlet	inlet to the system
LMTD	Log Mean Temperature Difference, °C
max	maximum
min	minimum
o	HX tube outer
out	output from the system
overall	total for the HX tube
P	pump

r	ratio
rec	rectifier
SHX	Solution Heat Exchanger
surr	surrounding
sys	system
tot	total
tube	HX tube

GREEK SYMBOLS:

α	Thermal diffusivity, m^2/s
Δ	Difference
ε	Heat exchanger effectiveness
ρ	Density, kg/m^3
η	Fin efficiency
ν	Kinematic viscosity, m^2/s
τ	Shear stress vector, Pa
σ	Surface tension, N/m; Area expansion ratio
μ	Viscosity, Pa-s
χ	Vapor Quality at the state point

SUBSCRIPTS

f	Fin of the HX tube
c	Channel of the HX tube
Micr	microchannel
Man	manifold
SCR	Solution circulation ratio
NTU	Number of Transfer Units
HX	Heat exchanger/Evaporator
r	refrigerant
w	water
base	Base of the channel

CHAPTER 1: INTRODUCTION

This chapter provides introduction to the current research work and background behind the selection of the problem. Further, a summary of research objectives and dissertation organization is provided.

1.1 Background and Motivation

In most recent years, a substantial focus is being placed on energy efficiency and optimum energy utilization processes in just about all energy-intensive industries. Based on a US Department of Energy report (2008), some 20 to 50% of industrial energy is lost as waste heat in the form of exhaust gases, cooling water and heat losses from hot equipment and heated surfaces [1]. Utilization of waste heat can make a significant impact in the overall improvement of most energy conversion processes. Numerous technologies are commercially available for large-scale industries to tap this waste heat and improve their energy productivity. In some cases, waste heat recovery technologies have increased the energy efficiency by as high as 50%. However, cost-effective recovery and utilization of waste heat from such industries requires high performance heat and mass exchangers, due to the small temperature/density gradients in the process-induced waste heat streams.

Typically waste heat recovery system has three essential components: a) a waste heat source(s) b) a recovery technology and c) use of the recovery energy. Figure 1-1 shows the essential components with a few examples of each category. Waste heat temperature is an important parameter of the waste heat sources and is a determinant in whether the recovered heat is usable. Work potential (based on Carnot efficiency) is another parameter that dictates the maximum energy taken out of the heat source for driving a heat engine.

Figure 1-1: Waste heat recovery components

Current heat recovery practices show some interesting and useful trends that provide a focus for research. The trends are as follows:

1) Waste heat recovery systems are constrained by factors such as temperature limits and cost. Though heat recovery systems have been installed in large scale industries, the quantity of heat recovery doesn't match its full potential. The key barriers are the material limits or cost associated with changing the high-grade heat to low-grade heat.
2) Most unrecovered heat is at low temperatures. Roughly 60% of the unrecovered waste heat is of low quality (temperature below 232 °C). Low-grade heat has less economical and thermal value, but the large quantity of this heat source makes it quite attractive both for research and also from an environmental perspective. Low-grade heat can be used for running refrigeration cycles for upgrading the heat, space heating, or refrigeration cooling.

3) Some industrial sectors, such as chemical plants, produce a large amount of waste heat through chemical compositions. But it is not economical to extract it because of the fouling characteristics of chemicals on the heat exchangers.
4) There is a significant amount of heat loss from nontraditional heat sources such as hot product streams and hot equipment surfaces.

Typically waste heat sources can be classified according to the exhaust temperature, and thus the source's usability can be defined. Table 1-1 shows the classification with typical recovery methods.

Table 1-1: Temperature classification of waste heat sources

Temperature range	Example sources	Temp(^{o}C)	Advantages & Disadvantages	Typical recovery methods
High (> 650 ^{o}C)	Glass melting furnace Steel electric furnace Hydrogen plants	1300-1540 1370-1650 650-980	High-quality energy, High heat flux, Higher power generation Thermal stresses on heat exchanger components, and increased chemical activities	Steam generation Combustion air preheats
Medium (230-650 ^{o}C)	Gas turbine exhaust Steam boiler exhaust IC engines	370-540 230-480 320-590	More compatibility with heat exchanger materials Practical for power generation	Steam generation Organic Rankine cycle
	Exhaust gases from gas-fired	70-230	Large quantities	Space and domestic

Low (< 230 °C)	boilers, ethylene furnaces Cooling water from furnace doors, IC engines, Condensers, Data Centers	30-120	available from numerous product streams.	water heating Upgrading heat Organic Rankine cycle

A typical distribution of the unrecovered waste heat losses is shown in Figure 1-2. The figure shows that almost 60% of the waste heat comes from low-grade heat. Despite low-grade heat having low working potential, 30% of the waste heat can be utilized.

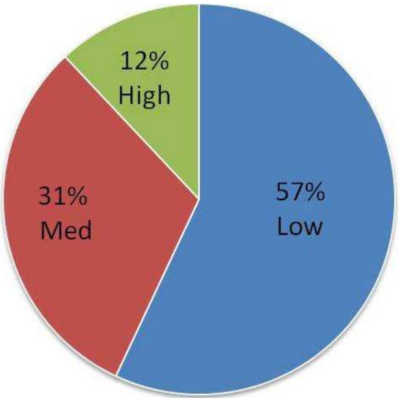

Figure 1-2: Total unrecovered waste heat based on different temperature groups

Heat recovery technologies use several heat exchangers in the form of recuperators, regenerators, heat wheels, heat pumps, and waste heat boilers. Figure 1-3 shows some common heat exchangers used in the waste heat recovery industries.

Low grade waste heat recovery due of its large availability becomes quite attractive. However, there are several challenges for recovering it like corrosion of heat exchanger surface in case of chemical plant discharges and large heat exchange surface requirement due to low thermal gradient. Heat recovery technologies include economizers, contact condensation recoveries, thermo compressors, transport membrane condenser, heat pump cycles like absorption cycles, compression cycles, and gas cycles, etc.

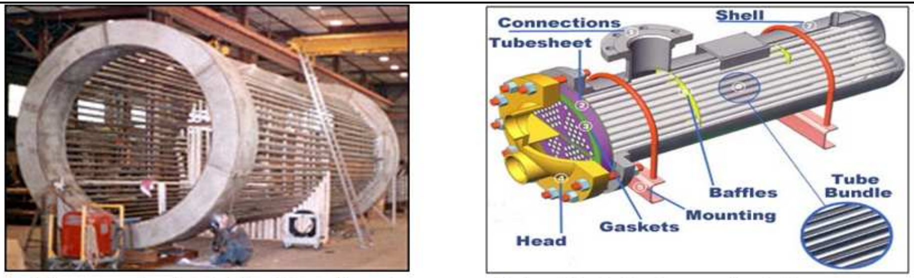

Radiation recuperator : Adapted from Hamon Thermal Transfer Corporation

Shell and tube heat exchanger : Adapted from Southwest Thermal Technology Inc.

Falling film evaporator: Adapted from Weinzhou Buieno Machinery Ltd.

Steam condensers: Adapted from Scam-Spa.it

Plate heat exchangers: Adapted from Modern energy technologies Ltd.

Figure 1-3: Some of the heat exchangers used in industries

Economizers can be typically used for preheating the fluid for boiler systems, power plants or heating, venting and air conditioning (HVAC). In case of boilers, it can be provided to utilize the flue gases heat for boiling the boiling feed water. In air pre heater systems, it can be used for heating the combustion air [2].

Direct condensation recovery involves cooling of flue gases by direct mixing of the flue gases with cooling fluid. These systems does not require any wall interface as in typical heat exchanger, hence heat transfer coefficients are higher and size of the equipment is small. However, there is a challenge that cooling fluid can get contaminated with contaminants in flue gases.

Thermo-compressor works on the principle of compressing low pressure gas by mixing with high pressure gas and using it at the intermediate pressure. The basic principle involves acceleration of high pressure steam through a nozzle into high velocity field. This entrains the low pressure steam and the mixture is recompressed in a divergent venturi. It is typically used in evaporators where boiling stream is recompressed and used into a heating steam.

Transport membrane condensers is an innovative concept demonstrated by Gas Technology Institute for efficient energy recovery from low pressure and low temperature flue gases using ceramic membranes [3]. Like direct contact heat recovery, this has been used successfully to extract water from flue gases without contamination. However, it needs more research for widespread implementation.

Heat pumps are the very popular breed of waste heat recovery units where heat is moved from a lower temperature to higher temperature using mechanical work or high temperature heat source. Application includes refrigerators, air conditioners and reversible-cycle heat pumps. The basic principle involves cycle movement of working fluid which carries heat from lower temperature at evaporator to condenser at higher temperature. Some external work has to be provided in form of mechanical work in case of vapor compression system or low grade heat input in case of absorption refrigeration system. Hence, where abundance of low grade waste heat is available, absorption chillers carries a huge potential. However, due to considerably large size of heat and mass exchangers used in the cycle, smaller absorption have not been very successful in the market due to the initial cost, bulky system and low COP. But with increasing electricity prices and environmental concerns, it is gaining demand again. And there is a clear need of making compact heat exchangers so that it can be more portable and more economical especially for small to medium size applications. Companies and institutes like Ago AG, EAW, ILK Dresden, Invensor, Punk, Sonneklima GmBH, Solarnext, Sortech AG, etc. are already developing small capacity absorption chillers for home air conditioning units.

Several design concepts such as shell & tube, falling film, plate heat, etc. are being used in industry for design of heat and mass exchangers for running refrigeration cycles. Usually, they are attributed to poor heat transfer coefficients and hence require much larger surface area. In last few decades, much focus have been put on microchannel technology because of availability of high surface area to volume ratio which leads to order of magnitude higher heat transfer coefficients. However, pressure drop penalty have restricted its high volume manufacturability and the research have been mostly limited to academia. An interesting novel concept called manifold microchannel technology was introduced years back to tackle the problem of pressure drop and increase the COP of such finer channels based systems. A systematic treatise has been provided in further chapters to scan through available research and demonstrate its usability for the design of much compact heat and mass exchangers.

1.2 Research Objectives

The main goal and the research objectives of this dissertation are as follows:

a) Prepare a working simulation model for a small scale absorption chiller system and identify critical parameter affecting the overall COP of the system.

b) Conduct a comprehensive review of evaporator design and enhancement in the open literature and demonstrate viability and novelty of the manifold microchannel technology for design of compact heat and mass exchangers for low heat flux applications.

c) Systematic study of single-phase fluid flow and heat transfer for a quarter-symmetry manifold microchannel element and identify all critical parameters influencing heat transfer coefficient and pumping power.

d) Development of a proof-of-concept prototype for a 5kW cooling capacity tubular evaporator based on manifold microchannel design philosophy, which was successfully tested for much higher pressure and is compatible with ammonia as the refrigerant.

e) Development of a novel flat plate evaporator based on single manifold microchannel concept which aligns with conventional plate heat exchanger design but provides much better heat transfer coefficients values, in support for further reduction of size/volume and weight of the heat and mass exchangers for absorption refrigeration cycles.

1.3 Dissertation Organization

Chapter 1 provides the background and motivation for the research being conducted. A basic introduction to waste heat recovery technology and its application is provided, followed by establishing the need for efficiently utilizing low grade waste heat though use of miniaturized absorption chiller systems which requires innovative compact design for heat and mass exchangers. Chapter 2 provides a brief introduction of the absorption cooling system and the basic fundamentals behind it. Results of simulation study carried out for single-stage cycle to identify the critical parameters are shown to support evaporator and solution heat exchanger design for the cycles. Chapter 3 provides a comprehensive review for evaporator and single-phase heat exchanger design available in literature. Further, review on microchannel evaporators and manifold microchannel design is provided establishing its importance in terms of heat transfer coefficient and pressure drop characterization. Chapter 4 is dedicated to single-phase numerical study of manifold microchannel system identifying critical geometrical and flow parameters influencing the evaporator design. Preliminary numerical optimization is provided using Dynamic-Q method integrated with commercial numerical solver. Chapter 5 covers detailed design of tubular evaporator and the experimental setup used for testing the prototype. Chapter 6 focuses on the experimental results obtained for several iterations in the design phase. Results are presented for aluminum microgroove tube with 1st generation manifold, improved (2nd generation) manifold and nickel microgrooved tube with improved headers. The last section of the chapter provides a brief introduction to the flat plate evaporator design and fabrication. A preliminary study was conducted and it would progress as future developmental work. Chapter 7 provides a summary of the findings and conclusions, as well as the suggested future work to continue further research in this area.

CHAPTER 2: ABSORPTION REFRIGERATION SYSTEM

This chapter starts with an introduction to heat pumps in general and compares vapor compression with absorption refrigeration system to emphasize the benefit of latter for waste heat recovery applications. Further, a study of single-stage absorption cycle with system level design enhancements was conducted using EES and important parameters are identified and discussed. The design of heat exchangers is critical for improving the COP of the cycle which would be discussed in further chapters.

2.1 Heat Pumps

Heat pumps, as introduced in the first chapter, are typically categorized into vapor compression and absorption refrigeration systems. Vapor compression refrigeration cycles are mostly used for HVAC applications. They are also used for domestic and commercial refrigeration. A schematic of a simple vapor compression cycle with a corresponding P-h diagram is shown below in Figure 2-1.

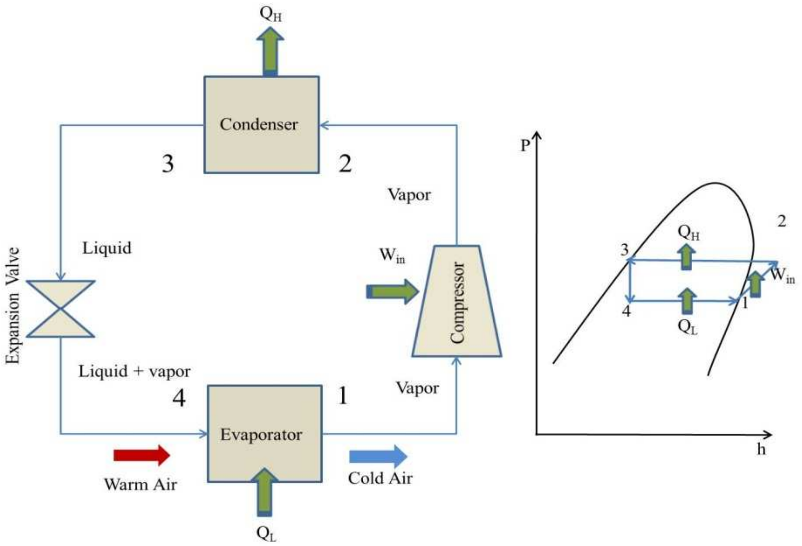

Figure 2-1: Schematic of a typical single-stage vapor refrigeration cycle

A saturated liquid vapor refrigerant mixture with low quality enters the evaporator and heat is exchanged with the process fluid at constant temperature. Saturated vapor exits the evaporator and enters the compressor, where work is added at constant entropy, and saturated vapor exits at higher pressure. Next, the saturated vapor is condensed at constant pressure, and saturated liquid exits the condenser. Finally, the saturated liquid goes through an isenthalpic process, and liquid vapor exits the expansion valve with reduced pressure. The cycle repeats. Typical refrigerants for domestic and commercial refrigeration are R-134a, R-600a, R-404A, etc. For building heating and cooling R-507 and R-717 are also used. The performance of the cycle is measured by parameter called "coefficient of performance (COP)". COP is the ratio of refrigeration capacity and the work/heat input to the system. For a reversible Carnot cycle, COP for cooling is defined as

$$COP_{Carnot} = \frac{T_L}{T_H - T_L} \tag{2-1}$$

This is the maximum COP for the cyclic devices, which can theoretically go to infinity but are limited due to second law of thermodynamics. For a typical single-stage vapor compression cycle, COP for cooling application and cycle efficiency is defined as:

$$\mathrm{COP_{VCRS}} = \frac{Q_L}{W_{in}} = \frac{h1 - h4}{h2 - h1}$$

$$\eta_R = \frac{COP_{VCRS}}{COP_{Carnot}} \tag{2-2}$$

where Q_L is the heat extracted at evaporator (also known as refrigeration capacity) and W_{in} is the work input for the compressor. For a typical household refrigerator, COP is around 5 and for an air-conditioner it is between 2 to 3. The actual vapor compression cycle is slightly different the discussed ideal cycle, as thermodynamic states do not remain constant and no state transition happens in an ideal way, which leads to further decrease in COP.

The absorption refrigeration cycle is another form of heat pump which uses a heat source to provide the energy needed to drive the cooling system. This is a popular alternative to compression refrigeration where electricity is expensive, unavailable and unreliable, compressor noise is problematic, and surplus heat is available for running the desorber. COP for single-stage absorption cycle is typically less than 0.5; however with some improvements and a multi stage cycle; COP can be greater than one.

A comparison between compression and absorption system is shown in Table 2-1 which demonstrates why the latter is preferred where ample waste heat is available.

Table 2-1: Comparison between compression and absorption system [4]

Compression System	Absorption system
Work operated and high COP	Heat operated and low COP
COP and refrigeration capacity very sensitive to evaporator temperatures	Performance not sensitive to evaporator temperatures
Performance is sensitive to evaporator superheat.	Evaporator superheat is not important.
COP reduces considerably at part loads	COP does not reduce significantly with loads
Liquid at exit of evaporator may damage compressor	Liquid at exit is undesirable for performance issues; but not a serious concern

Many moving parts – a reliability concern. Regular maintenance required	Few moving parts like pump and hence low maintenance required
Higher noise and vibration	Less noise and vibration
Large systems are bulky and small systems are compact	Small systems are bulky and large systems are compact
Economical when electricity is available	Economical where low cost fuel and waste heat is available
Most of the refrigerants are HFCs which are expensive and have high ozone depletion and global warming potential. As per Montreal protocol, their use will be prohibited by 2020!	No such issues as it uses salt solution like LiBr, ammonia water pairs, etc. which are naturally occurring and pose no danger to environment.

The above listed benefits of absorption refrigeration system over compression system make it an attractive field of research. The system is discussed in detail in the next section.

2.2 Absorption Refrigeration System

As discussed in the previous section, absorption refrigeration is just another type of heat pump which requires a heat source to provide the energy for driving the system. Although absorption cooling is used for conventional cooling in buildings, it is particularly applicable for cooling applications where heat is supplied from the waste heat generated by a gas turbine engine, solar energy, or any other source providing low-grade heat such as process plants or IC engines. There are other heat driven technologies in literature like adsorption (solid/vapor), magnetic refrigeration, and

Stirling cycles, but absorption systems are one of the oldest and most widely applied [5].

The heat driven heat pumps can be typically categorized as Type 1 and Type II heat pumps. In Type I pumps, heat input is at highest temperature level and the output is either refrigeration at the lowest temperatures or heating at intermediate temperatures. In Type II pumps, heat input is at intermediate temperature and product heat output is at the highest temperature level. Type II pumps are also known as heat transformers or temperature amplifiers. One basic difference between Type I and Type II is that the evaporator and absorber work at higher pressures in Type I pumps and at lower pressures in Type II pumps. Type I pumps are more popular and widely used in commercial buildings as water chillers for air conditioning applications. Type II pumps have been demonstrated in a few industrial applications but are not very economical. For low-grade waste heat recovery, Type I is more suitable, and therefore discussion will be limited to this type of pump.

The most widely used available absorption technologies used in the market are either water/lithium bromide chillers or ammonia/water chillers. A comparison is shown in Table 2-2 below [5].

Table 2-2: Comparison between working fluid pairs for VARS

Water/Lithium bromide chillers	Ammonia water chillers
Has been widely used since 1950’s	Used since late 1800’s. Used for ice production prior to vapor compression technology
Water is refrigerant. Does not require rectifier due to low vapor of salt.	Ammonia is used as refrigerant. Requires rectifier as water is volatile.

Typically used as water chillers for air condition applications. Main competing technology is vapor compression chillers.	Used for large tonnage industrial applications requiring low temperatures for process work. Also sold as air-cooled and gas-fired air conditioning component, solar cooling.
0.7 < COP < 1.2	Typically around 0.5. However, a triple effect-two stage-absorption air conditioner can show a COP of 1.7.
Cannot operate below zero and dangers of crystallization. Works at sub atomic pressures.	Can work at much lower temperatures. Works at higher pressures.
Mostly compatible with all materials, but corrosion can be a concern due to presence of aqueous salt solution. Good compatibility with most rubber and polymer compounds.	Ammonia is toxic at high ppm and not compatible with copper. But is inexpensive, environmentally compatible and has excellent thermodynamic properties.

Due to the excellent thermodynamic properties of ammonia-water pair and operation at sub-zero temperatures, it is a good choice for running the cycle. It also works at large pressure difference between high pressure and low pressure components, which is preferable for compact heat exchanger designs. Also, ammonia/water systems are becoming an important component of integrated energy conversion system in which the complete system produces electricity, heat and cold.

A schematic for single-stage ammonia/water absorption refrigeration cycle is shown in Figure 2-2.

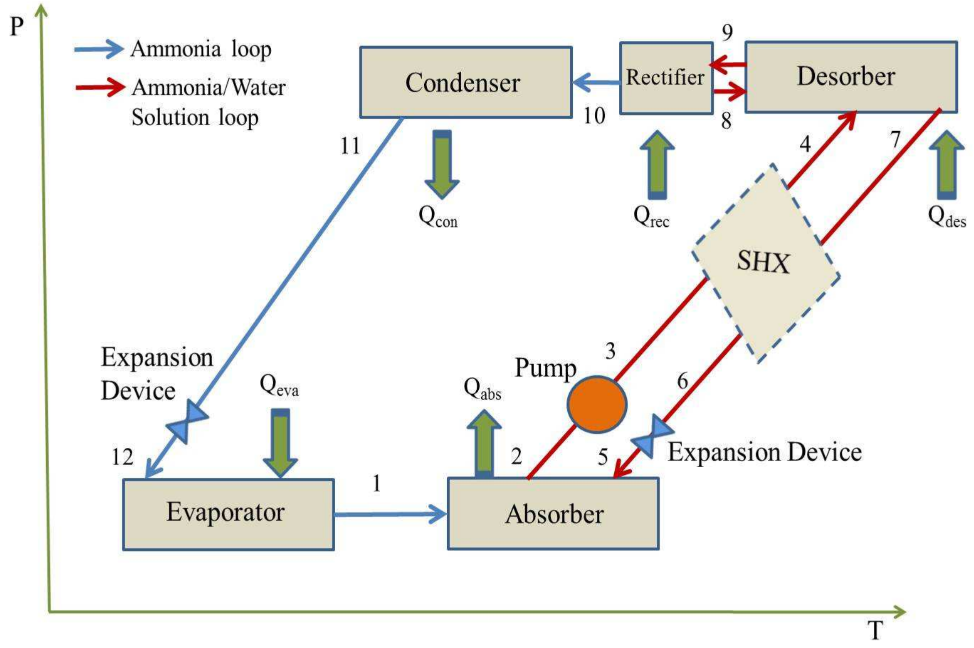

Figure 2-2: Schematic of a Type I single-stage ammonia/water absorption refrigeration cycle

In comparison to components of vapor compression systems, the compressor is replaced with an absorber/desorber system which contains a refrigerant and absorbent solution. For the ammonia/water cycle, ammonia works as refrigerant and water is the absorbent solution.

Details of the components and their thermodynamic state are discussed briefly below.

1) **Evaporator** –This has the function of evaporating the refrigerant (ammonia) usually at constant saturation temperature. The inlet to the evaporator (state 12) is usually liquid and vapor mixture at low quality while outlet from evaporator (state 1) is saturated or superheated vapor. The enthalpy is gained due to the heat load provided at evaporator, which is also the refrigeration capacity. There can be some temperature glide (decrease in temperature) due to pressure drop (caused by friction) inside the evaporator.

2) **Absorber –** The rich ammonia vapor leaving the evaporator (state 1) goes for absorption into the weak solution (less concentration of ammonia in water) available at state 5. The absorption process takes place in the absorber and makes it a critical component of the cycle. Complex heat and mass transfer with chemical kinetics is involved in the process. Ammonia dissolves in the water well releasing NH4+ and OH- ions. The reaction is highly exothermic (releases heat) which can increase the solution temperature and hence can slow down the absorption process, if not removed efficiently. The new rich solution (higher concentration of ammonia in water) is available at state 2 for further processing.
3) **Pump –** A pump provides the external mechanical work needed to pump the rich solution to higher pressure at state 3. But the work input is quite low in comparison to the compressor of vapor compression system.
4) **SHX (Solution heat exchanger) –** The solution heat exchanger is another critical component that has major role in affecting the performance (COP) of the cycle. Its main function is to reduce the heat input to the desorber by preheating the incoming cold rich solution. On the returning path, it also precools the hot weak solution recycled from the desorber.
5) **Desorber –** The function of desorber is to evaporate the ammonia from the rich solution and direct it to the condenser through the rectifier. It operates at high pressure and high temperature and requires a high heat input. The weak solution is recycled back to the absorber through solution heat exchanger. As

water is volatile, some of the amount gets evaporated along with ammonia which is undesirable.

6) **Rectifier –** The rectifier is required in the case of the ammonia-water solution to completely remove the water vapor before reaching the condenser. Water vapor can condense on the condenser surface and decrease condenser performance. The ammonia mass fraction exiting the rectifier is critical, as COP heavily depends on it. A small reduction in ammonia concentration amplifies the COP decrease.
7) **Condenser** – Saturated/superheated ammonia vapor gets condensed to saturated liquid at same higher pressure. It is similar to the vapor compression system.
8) **Expansion device –** An expansion device is needed for reducing the pressure and usually the process in this device is an isenthalpic process. It is used between states (6-5) for reducing the pressure of weak solution and also between states (11-12) for reducing the pressure of liquid ammonia available at the exit of condenser.

Mass balance and energy balance for each component is shown below (‘m’ refers to total mass flow rate, ‘x’ is the concentration of ammonia and ‘h’ is the enthalpy). If enthalpy is known at all state points, the system has 25 equations and 25 unknowns which can be solved for finding mass flow rates and ammonia concentration at each state points. The number of equations and unknowns will increase for complex cycles.

The cycle works on two pressures: the condenser & desorber at higher pressure and evaporator & absorber at lower pressure. As it is a Type I pump, it also works on three temperatures: evaporator at lower temperature, absorber and condenser at intermediate temperatures, and desorber and rectifier at higher temperatures. The rectifier temperature is little lower than the absorber temperature. But here for the sake of simplicity, it was assumed to be the same.

From the first law of thermodynamics, energy has to be conserved:

$$Q_{evap} + Q_{des} - Q_{con+abs+rec} + W_P = 0 \tag{2-3}$$

From the second law of thermodynamics, total entropy change is the sum of entropy change in the system and surroundings:

$$\Delta S_{tot} = \Delta S_{sys} + \Delta S_{surr} \geq 0 \tag{2-4}$$

Based on temperature estimates and various energy transfers, a simplified energy flow diagram can be made as shown in Figure 2-3.

As the refrigeration cycle is a closed system, the total entropy change on the working fluid of the system is zero.

$$\Delta S_{sys} = 0$$

$$\Delta S_{surr} = -\frac{Q_e}{T_e} - \frac{Q_{des}}{T_g} + \frac{Q_{abs}}{T_o} + \frac{Q_{con}}{T_0} - \frac{Q_{rec}}{T_g} \geq 0 \tag{2-5}$$

$$Q_g\left(\frac{T_G-T_o}{T_G}\right)\geq Q_e\left(\frac{T_o-T_e}{T_e}\right)+Q_{rec}\left(\frac{T_G-T_o}{T_G}\right)-W_P \tag{2-6}$$

Absorber

$$m_1+m_5=m_2;m_5x_5+m_1x_1=m_2x_2;m_1h_1+m_5h_5=m_2h_2+Q_{abs}$$

Solution expansion Valve

$$m_5=m_6;x_5=x_6;h_5=h_6$$

Pump

$$m_2=m_3;x_2=x_3;m_2h_2+W_P=m_3h_3$$

Solution heat exchanger

$$m_3=m_4;x_3=x_4;m_7=m_6;x_7=x_6;m_3h_3+m_7h_7=m_4h_4+m_6h_6$$

Desorber

$$m_4+m_8=m_9+m_7;m_4x_4+m_8x_8=m_9x_9+m_7x_7;m_4h_4+m_8h_8+Q_{des}=m_9h_9+m_7h_7$$

Rectifier

$$m_9=m_8+m_{10};m_9x_9=m_8x_8+m_{10}x_{10};m_9h_9+Q_{rec}=m_8h_8+m_{10}h_{10}$$

Condenser

$$m_{11}=m_{10};x_{11}=x_{10};m_{10}h_{10}=m_{11}h_{11}+Q_{con}$$

(2-7)

Refrigerant expansion valve

$$m_{11}=m_{12};x_{11}=x_{12};h_{11}=h_{12}$$

Evaporator

$$m_{12}=m_1;x_{12}=x_1;m_1h_1=m_{12}h_{12}+Q_{eva}$$

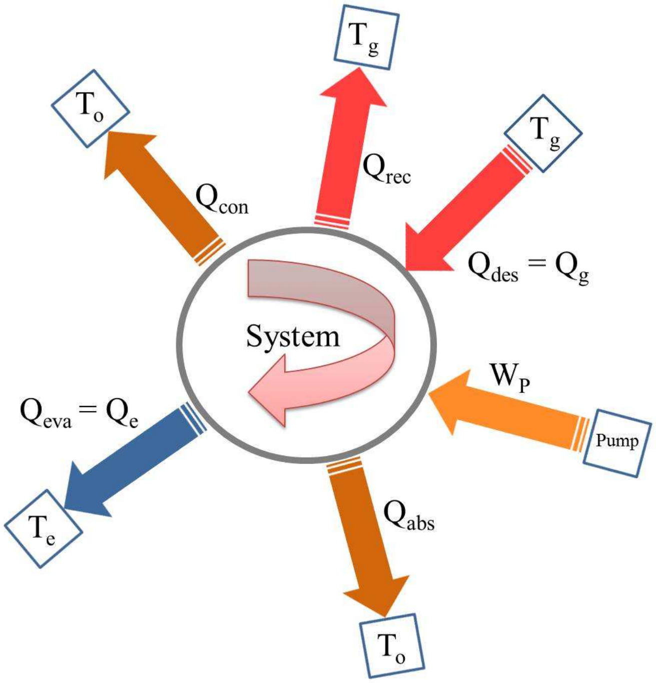

Figure 2-3: Energy transfer in a simplified VARS

Since the solution pump work is negligible and rectifier heat output can be neglected also (for the sake of simplicity, as it is not significant compared to the condenser and absorber outputs), COP can be derived as

$$COP_{ideal,VARS} \leq \left(\frac{T_e}{T_0 - T_e}\right)\left(\frac{T_g - T_o}{T_g}\right) \tag{2-8}$$

So, the maximum COP of an ideal VARS cycle (totally reversible) is

$$COP_{ideal,VARS} = \frac{Q_e}{Q_g} = \left(\frac{T_e}{T_o - T_e}\right)\left(\frac{T_g - T_o}{T_g}\right) = COP_{Carnot}.\eta_{Carnot} \tag{2-9}$$

The COP can be also considered as a combined system consisting of a Carnot heat engine and a Carnot refrigerator. The actual COP of a VARS will be much less than this because various irreversibilities exist in the actual cycle.

There are various ways to utilize the rejected heat that cannot be used in the cycle for single-stage. Utilization of the rejected heat can lead to improved COP. One way is to use the condensate precooler, which subcools the liquid entering the evaporator. This leads to a reduction in enthalpy at the evaporator entry and no change in exit enthalpy, providing more refrigeration capacity.

However, the precooler superheats the vapor entering the absorber and can lead to bigger absorber size, lower heat rejection temperature at the absorber or lower mass fraction of solution streams which in turn can lead to higher desorber temperature. Another way to use the rejected heat is to use the rectifier heat output for preheating the cold rich solution before it enters the solution heat exchanger. As the waste rectifier heat is getting utilized in the cycle itself, it increases the COP of the cycle. There are many other ways to improve the COP by using double-stage or triple-stage cycles and minimizing the waste output. But these come with other penalty in terms of size, cost and reliability. So, there is a tradeoff between performance and cost.

2.3 Single-Stage Absorption Cycle Simulation

The motivation behind this investigation is to develop a low-cost, heat actuated cooling system with applications for a military generator waste heat recovery unit, small scale micro-CHP and transport refrigeration systems. The electrical generator for supporting military operation consume large amount of fuel with the majority of power used for electronic equipment cooling and HVAC applications. An efficient waste heat recovery unit utilizing the low-grade heat available from the exhaust gases can considerably reduce the fuel consumption and increase electrical generation capacity. In such a unit, COP must be increased, a wide range of ambient temperatures must be accommodated, and low weight per ton of chilling must be achieved. The heat exchangers alone can consume up to 75% of the gross weight for such recovery units. Hence, a novel design must be incorporated to reduce their size with increasing COP. A comprehensive cycle simulation is needed to ascertain the importance of all system parameters and how they can be tweaked to achieve the desired outcome. The simulation was carried out using Engineering Equation Solver, and the following cycles have been considered and characterized in terms of system parameters.

a) Single-stage ammonia-water absorption cycle

b) Single-stage ammonia-water absorption cycle with precooler

c) Single-stage ammonia-water absorption cycle with precooler and integrated rectifier

2.3.1 Single-stage ammonia-water absorption cycle

The single-stage cycle comprises basic components of the ammonia water cycle described in the previous sections. There are twelve thermodynamic state points available as shown in Figure 2-4 where nine inputs are needed in order to solve the whole cycle. The following inputs have been used:

a) Evaporator Exit Temperature ($T_{evap,outlet}$, °C)

b) Evaporator exit vapor quality ($\chi_{evap,outlet}$)

c) Mass flow rate through the pump ($\dot{m}_{pump}$)

d) Absorber exit temperature ($T_{abs,outlet}$,°C)

e) Condenser exit temperature ($T_{con,outlet}$,°C)

f) Solution heat exchanger mass fraction difference (Δx)

g) Solution heat exchanger pump efficiency (η_P)

h) Solution heat exchanger effectiveness (ε_{SHX})

i) Rectifier ammonia mass fraction output ($x_{rect,outlet}$)

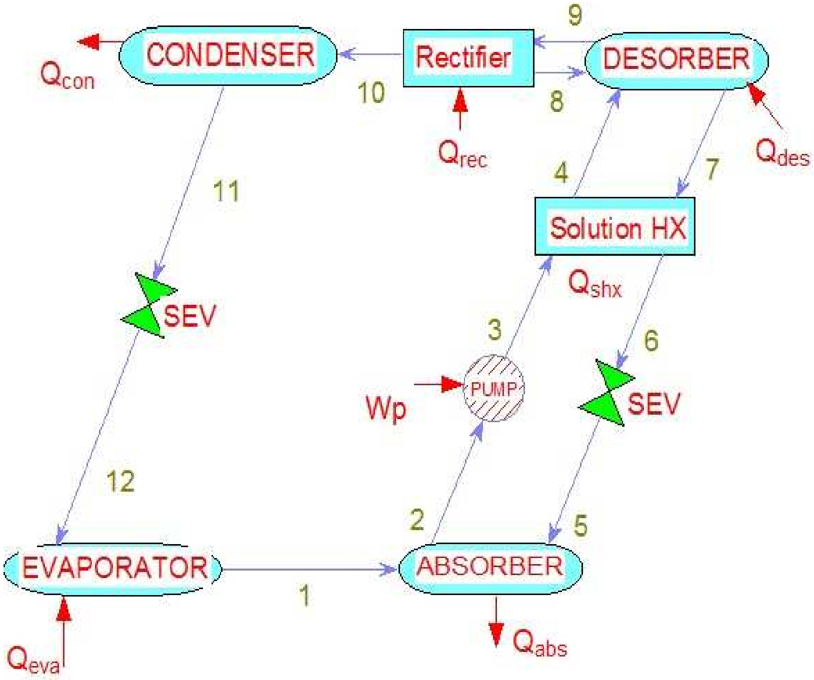

Figure 2-4: Single-stage ammonia-water cycle in EES

The solution heat exchanger pump efficiency (η_P) is needed to calculate the pumping power defined by (W_P):

$$W_P = \left(P_{ARC\_high} - P_{ARC\_low}\right)\left(\frac{\dot{m}_{pump}}{\rho \eta_P}\right) \tag{2-10}$$

where P_{ARC_high} is the highest operating pressure of the cycle, P_{ARC_low} is the lowest operating pressure of the cycle, $\dot{m}_{pump}$ is the mass flow rate to solution pump and ρ is the density of the rich solution mixture passing through the solution heat exchanger.

The solution heat exchanger effectiveness is defined by:

$$\varepsilon_{SHX} = \left(\frac{T_7 - T_6}{T_7 - T_3} \right) \tag{2-11}$$

where T_7 is the temperature of the lean mixture coming out of desorber, T_6 is the temperature of the lean mixture coming out of solution heat exchanger and T_3 is the temperature of the rich mixture going into the solution heat exchanger.

The following outputs for the cycle have been monitored and further studied:

a) Solution circulation ratio, SCR

b) Solution pump power , W_P (kW)

c) Cooling capacity of solution heat exchanger, Q_{SHX}(kW)

d) Heat dissipated by absorber, Q_{abs}(kW)

e) Heat input to rectifier, Q_{rec}(kW)

f) Heat input to desorber, Q_{des}(kW)

g) Condenser cooling capacity, Q_{con}(kW)

h) Evaporator cooling capacity, Q_{eva}(kW)

i) Coefficient of performance, COP

where solution circulation ratio, SCR is defined using ammonia mass fraction at the state points shown in Figure 2-2.

$$SCR = \frac{x_{10} - x_7}{x_4 - x_7} \tag{2-12}$$

All cooling capacities and heat dissipation for heat and mass exchanger components are defined by conventional first order equations using mass flow rate, specific heat capacity and temperature difference.

Coefficient of performance is defined by:

$$COP = \frac{Q_{eva}}{Q_{des} + W_P} \tag{2-13}$$

2.3.1.1 Baseline Case

A baseline case was solved based on the requirement of an existing unit running at independent ammonia-test facility. For proprietary reasons, details related to the actual cycle configuration cannot be provided and discussed. But the original cycle was reduced to a single-stage cycle and the data was used to carry out all further simulation work. Further in the chapter, COP comparisons would be provided too to show the improvement based on cycle enhancements.

$$\begin{array}{llll} T_{evap,inlet} & = 8.77\,^{\circ}C; & \Delta x & = 0.1 \\ \chi_{evap,outlet} & = 0.8902; & x_{rect,outlet} & = 0.9896 \\ \dot{m}_{pump} & = 0.0874\,kg/s; & \eta_{pump} & = 1 \\ T_{abs,inlet} & = 64.9\,^{\circ}C; & \varepsilon_{SHX} & = 0.8 \\ T_{con,outlet} & = 64.9\,^{\circ}C & & \end{array} \tag{2-14}$$

The following results were obtained in terms of output parameters after solving the cycle.

$$
\begin{aligned}
&SCR = 7.47; && Q_{des} = 29.27\ kW \\
&W_p = 0.2473\ kW; && Q_{con} = 12.81\ kW \\
&Q_{SHX} = 27.44\ kW; && Q_{eva} = 9.673\ kW \\
&Q_{abs} = 21.79\ kW; && COP = 0.3277 \\
&Q_{rec} = 4.596\ kW &&
\end{aligned}
\tag{2-15}
$$

These results provided the important design objectives for the evaporator and solution heat exchanger which will be discussed in further chapters. Based on these results, 5 kW was the target object for the evaporator design and 20 kW for the solution heat exchanger. Further, it was also required that COP >0.5 can be achieved for better thermal performance of the cycle, which would require integration of heat exchanger components in the form of a precooler and integrated rectifier.

2.3.1.2 Influence of Solution Heat Exchanger Effectiveness

Heat exchanger effectiveness is a critical parameter affecting the COP of the absorption cycle. In heat exchanger analysis, when inlet and outlet temperatures for both streams are known, the conventional LMTD method can be used. In the absence of these parameters, NTU (Number of Transfer Units) methods have to be used [6].

Effectiveness, ε is typically a function of NTU and ratio of heat capacity rates.

$$
\begin{aligned}
&\varepsilon = f\left(NTU, C_r\right) \\
&C_r = \frac{C_{\min}}{C_{\max}}
\end{aligned}
\tag{2-16}
$$

where C_{min} and C_{max} are minimum and maximum heat capacity rate of the fluid streams respectively. NTU is defined by:

$$NTU = \frac{UA}{C_{\min}} \tag{2-17}$$

where U is the overall heat transfer coefficient of the heat exchanger and A is the base heat exchange surface area.

For a parallel flow heat exchanger, heat exchanger effectiveness is given by:

$$\varepsilon = \frac{1 - \exp[-NTU(1 + C_r)]}{1 + C_r} \tag{2-18}$$

For a counter flow heat exchanger, it is given by:

$$\varepsilon = \frac{1 - \exp[-NTU(1 - C_r)]}{1 - C_r \exp[-NTU(1 - C_r)]} \tag{2-19}$$

When $C_r = 1$; it reduces to

$$\varepsilon = \frac{NTU}{1 + NTU} \tag{2-20}$$

For two-phase heat exchangers such as evaporators and condensers, $C_r = 0$ as energy change in the two-phase fluid is independent of temperature change and heat capacity theoretically tends to infinity. The effectiveness is also independent of flow arrangement and hence the effectiveness equation reduces to:

$$\varepsilon = 1 - \exp(-NTU) \tag{2-21}$$

Based on the above relations, it can be seen that UA significantly impacts the effectiveness of the heat exchanger. This means that the better the overall heat transfer coefficient, the more effective the heat exchanger. As the objective of the cycle is to also reduce the size and weight, it becomes imperative to achieve better overall heat transfer coefficient through novel deigns methods.

Figure 2-5 shows the variation of cooling capacity and heat input/output for all the heat and mass exchanger components with solution heat exchanger effectiveness. Heat input to the desorber and heat output from the absorber significantly decreases with increase in SHX effectiveness, and SHX cooling capacity increases. However evaporator cooling capacity, condenser heat output and rectifier heat input requirements does not change as SHX parameter change only affect ammonia-water loop. The pump power requirement is low and the solution circulation ratio remains constant. Due to the significant decrease in desorber heat input, COP significantly increases, as shown in Figure 2-6.

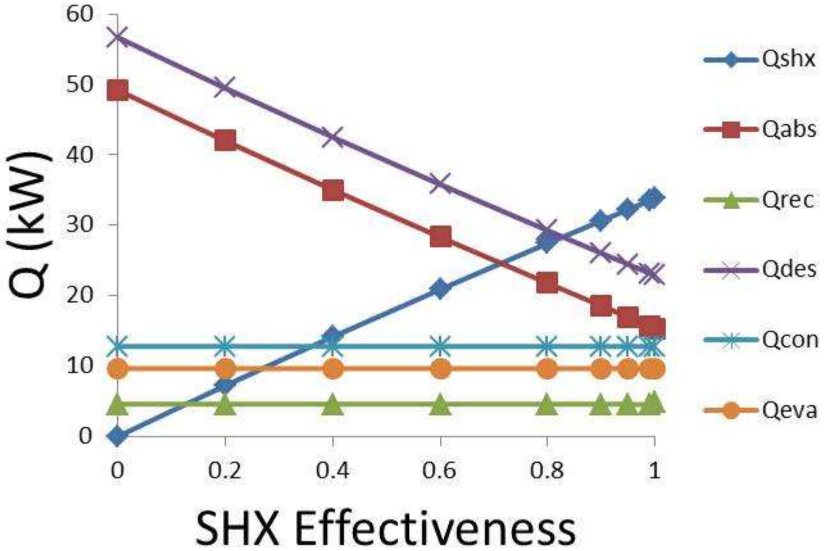

Figure 2-5: Heat transfer rate variation with solution heat exchanger effectiveness

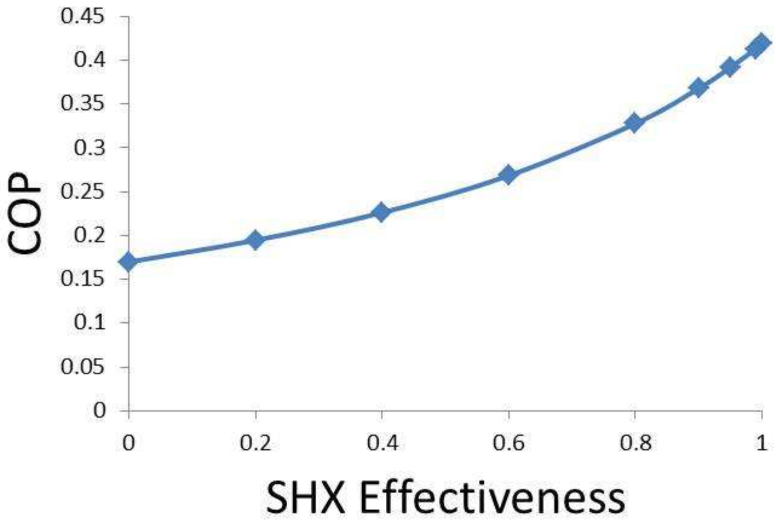

Figure 2-6: COP variation with solution heat exchanger effectiveness

2.3.1.3 Influence of Evaporator Exit Vapor Quality

Evaporator exit quality is generally desired to be as high as possible. But the desorber heat input requirement as shown in Figure 2-7 is in the bottom range which significantly affects the COP. For exit vapor quality from 0.89 to 0.99, the lower system pressure decreases by 6 times (from 541 kPa to 90 kPa) which affect all the components. It is observed from the simulation data that when evaporator exit quality increases, keeping the absorber exit temperature constant, a much leaner solution is entering the solution pump. Hence, to maintain the same rectification mass fraction output, more heat is needed at the desorber. This in turns also increases the cooling capacity of the SHX as the much leaner hot solution is leaving the desorber to the solution pump.

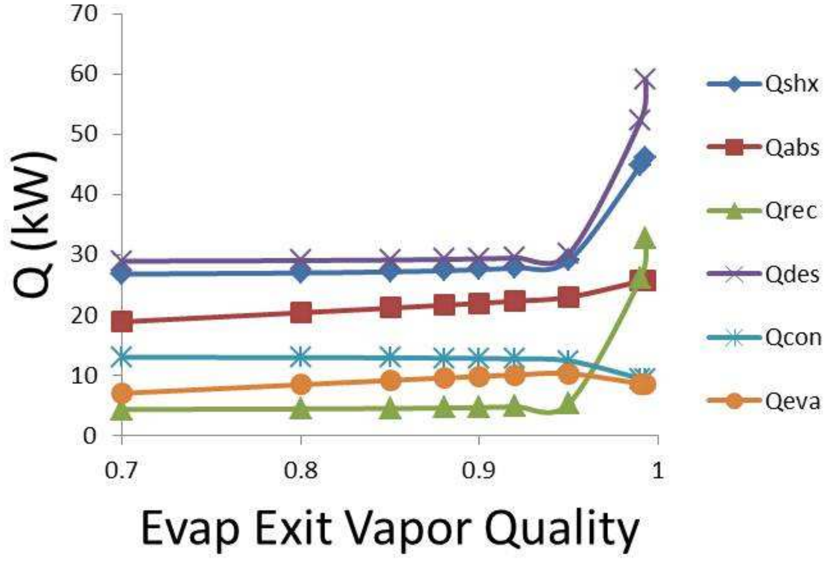

Figure 2-7: Heat transfer rate variation with evaporator exit vapor quality

The evaporator capacity tends to dip in the same range despite large enthalpy difference as less mass flow rate of ammonia is available from the condenser. The COP curve goes through a peak and it decreases with change in exit quality away from the peak as shown in Figure 2-8.

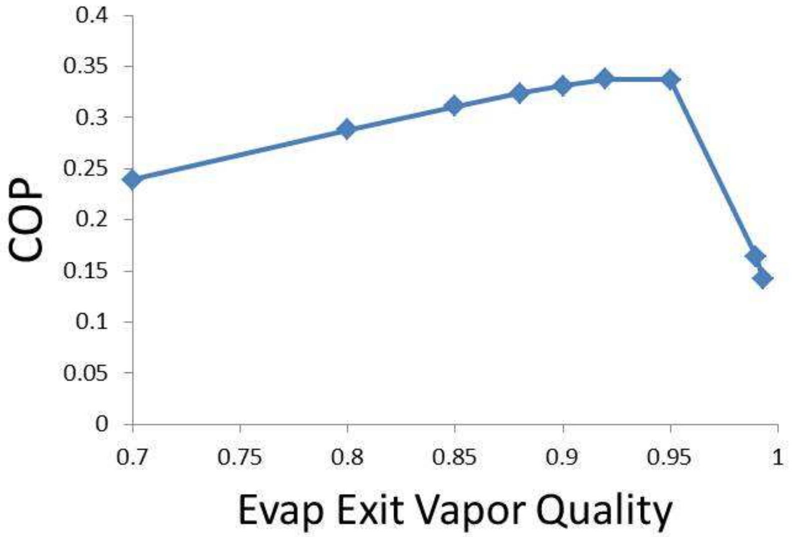

Figure 2-8: COP variation with evaporator exit vapor quality

2.3.1.4 Influence of ammonia mass fraction output from rectifier

Ammonia mass fraction output from the rectifier has the highest sensitivity to COP among all input parameters as it directly affects the performance of condensers and evaporator. The higher the water content in the two-phase cycle, the more performance degradation, as the vapor pressure of ammonia is much higher than water. The water can occupy the significant heat transfer area in the evaporator and due to low sensible heat rate; it can degrade the evaporator output quality. In the current simulation case as the evaporator output and quality were kept constant, the cooling capacity of evaporator and condenser were not affected but the rectifier and desorber heat input shot up as shown in Figure 2-9.

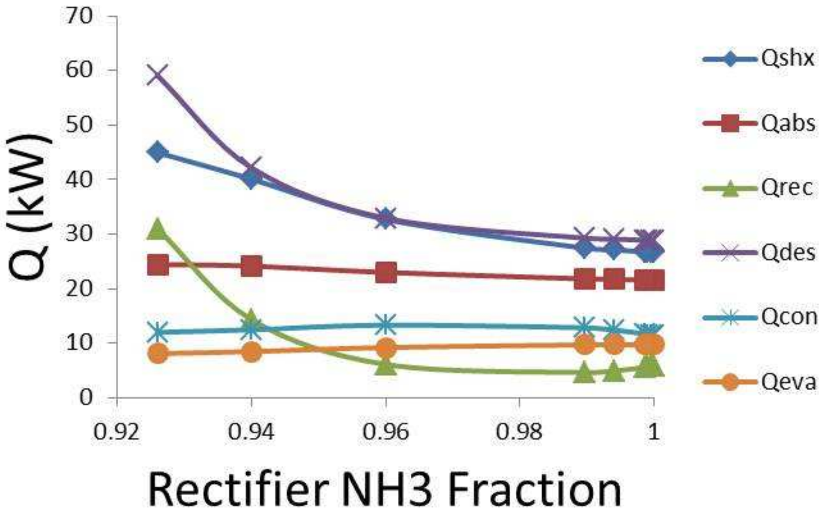

Figure 2-9: Heat transfer rate variation with NH_3 mass fraction output from rectifier

COP decreases by 144% with only 8% decrease in rectification as shown in Figure 2-10 which makes the rectifier optimum functioning critical for the whole cycle.

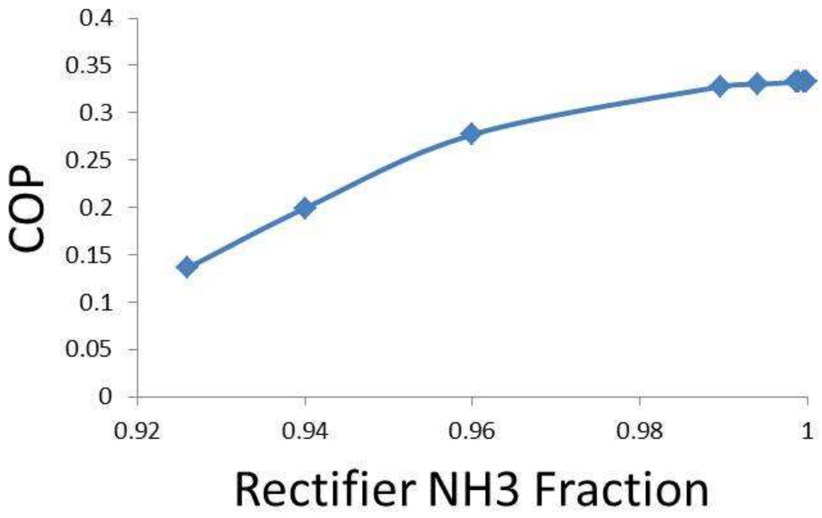

Figure 2-10: COP variation with NH_3 mass fraction output from rectifier

2.3.1.5 Influence of rich and lean mixture concentration difference

The concentration difference across the solution heat exchanger affects all the components of the cycle and the heat transfer rate almost linearly increases with increasing concentration difference as shown in Figure 2-11.

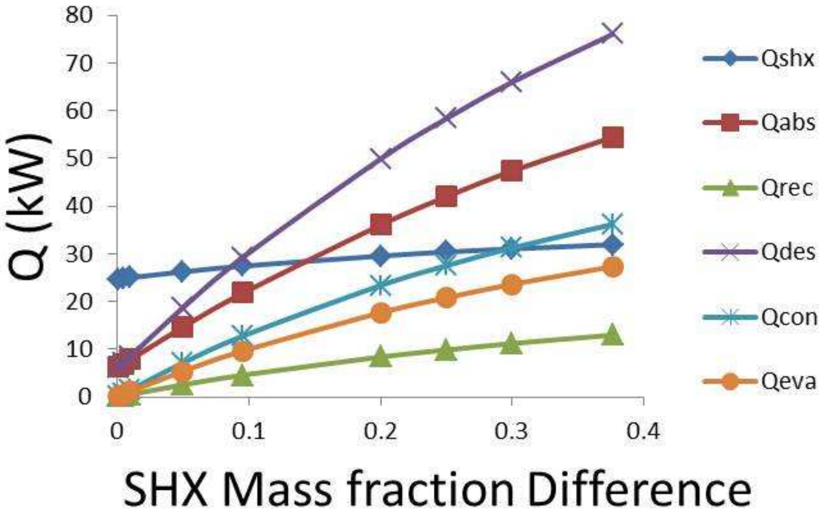

Figure 2-11: Heat transfer rate variation with NH3 mass fraction difference across SHX

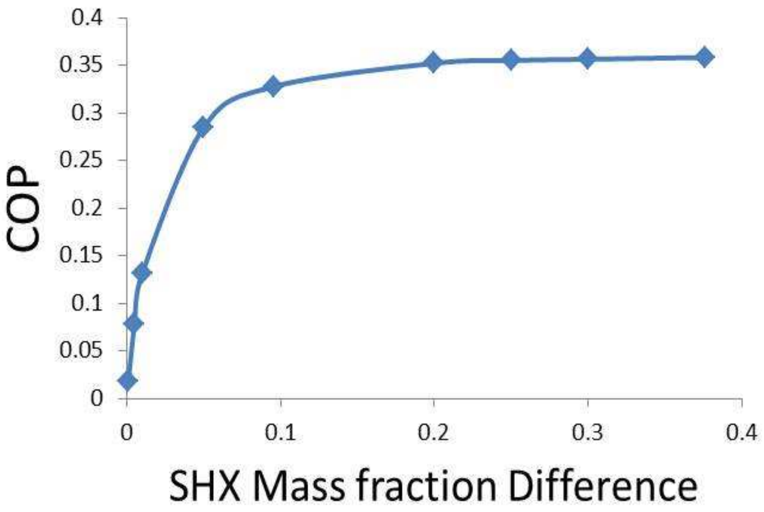

Figure 2-12: COP variation with NH3 mass fraction difference across SHX

The solution heat exchanger capacity does not change much, as the enthalpy difference across both solution streams remains constant. When the concentration difference reaches lower values, the solution circulation ratio increases exponentially and COP decreases drastically. It is further observed that COP fairly remains constant in the wider range as shown in Figure 2-12.

2.3.1.6 Influence of evaporator exit temperature

Evaporator temperature has very similar trend compared to ammonia mass fraction output from the rectifier. As the evaporator temperature increases, the desorber heat input decreases significantly and the evaporator capacity increases moderately, as shown in Figure 2-13. Both effects lead to enhanced COP and leads to a favorable design for the current simulation. The rectifier heat input significantly decreases to close to zero for evaporator temperature closer to 35 °C. For the same temperature, it can be seen in Figure 2-14 that COP > 0.5, which was the design objective for this case. However, the penalty for this may be that it leads to a higher system pressure requirement.

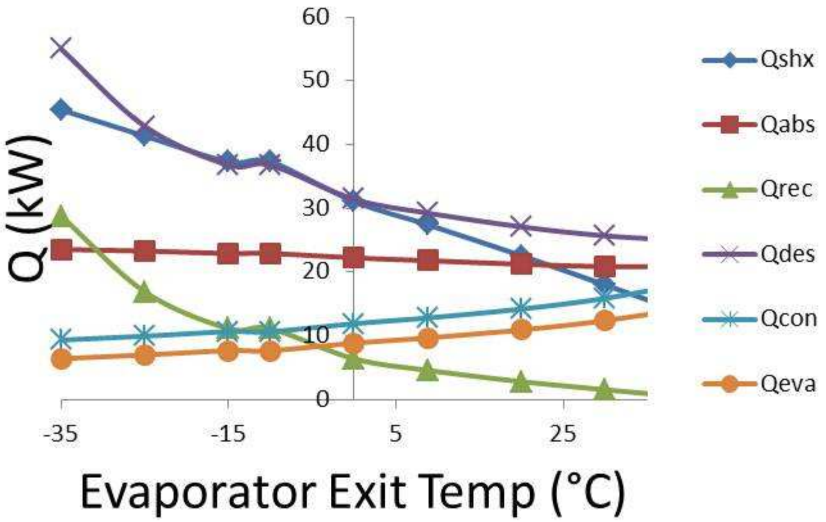

Figure 2-13: Heat transfer rate variation with evaporator temperature

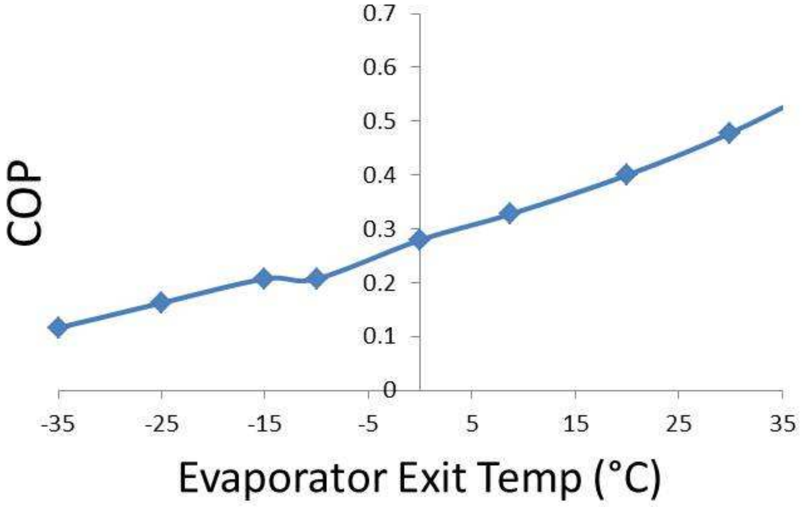

Figure 2-14: COP variation with evaporator temperature

2.3.1.7 Influence of solution pump flow rate

The mass flow rate through solution pump linearly affects all the components and COP remains constant for the data studied as shown in Figure 2-15 & Figure 2-16 respectively.

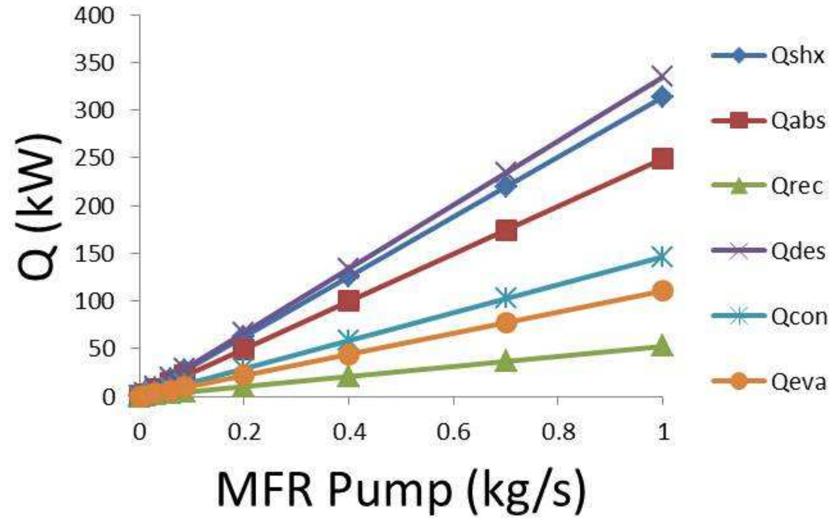

Figure 2-15: Heat transfer rate variation with solution pump mass flow rate

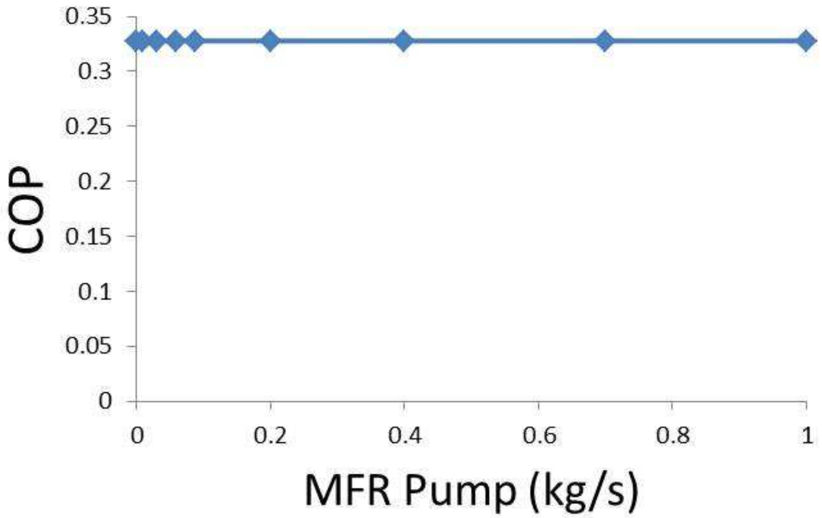

Figure 2-16: COP variation with solution pump mass flow rate

2.3.1.8 Influence of rich solution temperature exiting from absorber

The rich solution temperature exiting from the absorber affects the solution circulation ratio and the evaporator temperature considerably. As more enthalpy is made available in the solution stream for a constant evaporator temperature and exit quality, heat dissipated from absorber goes down, as shown in Figure 2-17.

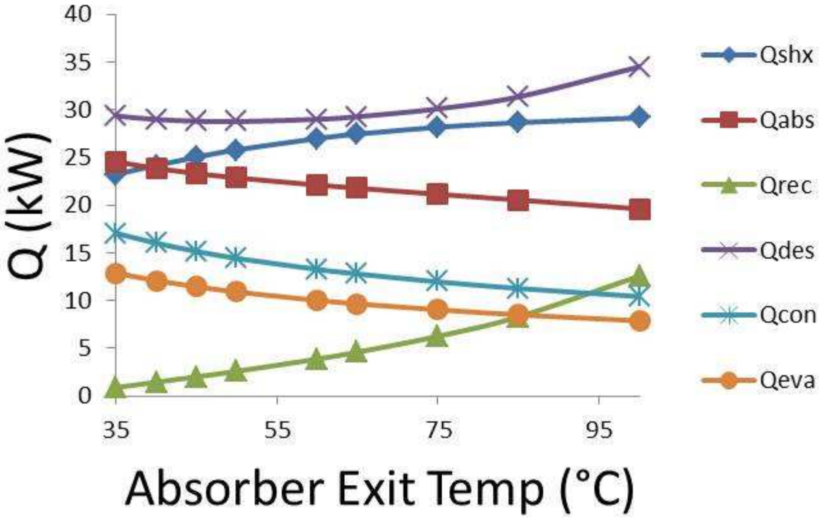

Figure 2-17: Heat transfer rate variation with absorber exit temperature to the pump

As the desorber heat input and SHX capacity remain fairly the same with decreasing evaporator cooling capacity, COP decreases by half, as shown in Figure 2-18.

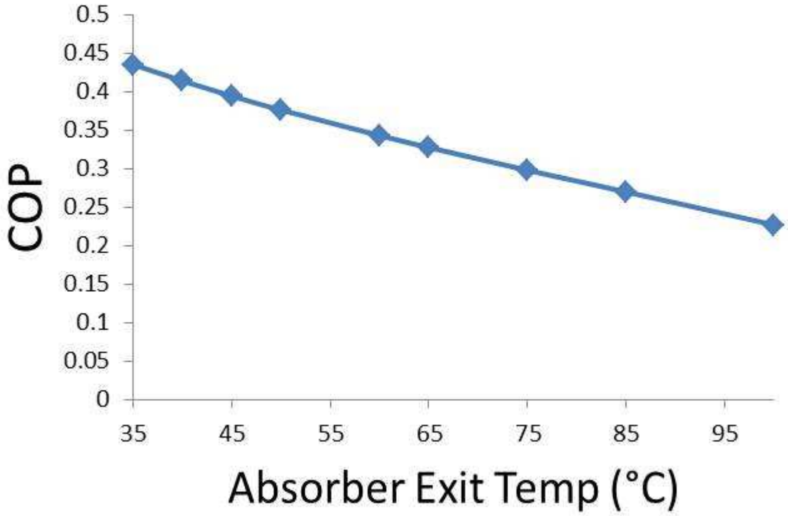

Figure 2-18: COP variation with absorber exit temperature to the pump

2.3.1.9 Influence of condenser exit temperature

Higher condenser exit temperature significantly decreases the condenser capacity which in turns also affects the evaporator cooling capacity. SHX cooling capacity, desorber heat input and absorber heat dissipation also increase, as shown in Figure 2-19.

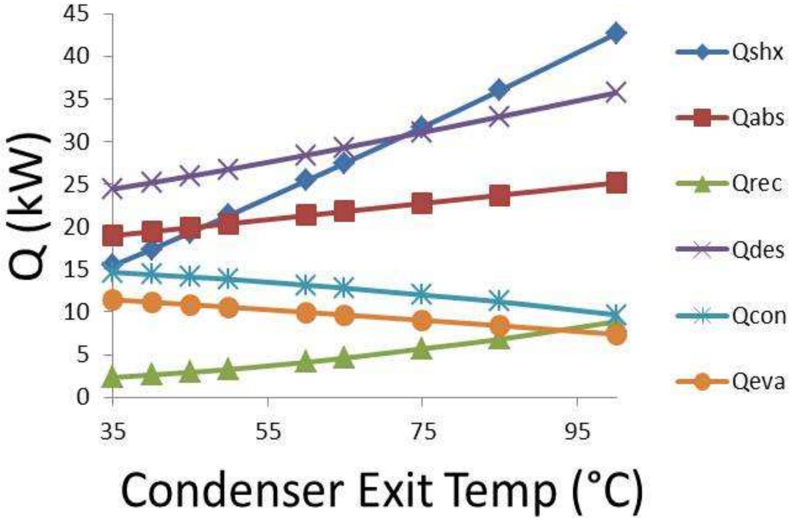

Figure 2-19: Heat transfer rate variation with condenser exit temperature

COP has a similar trend to the absorber exit temperature, as shown in Figure 2-20.

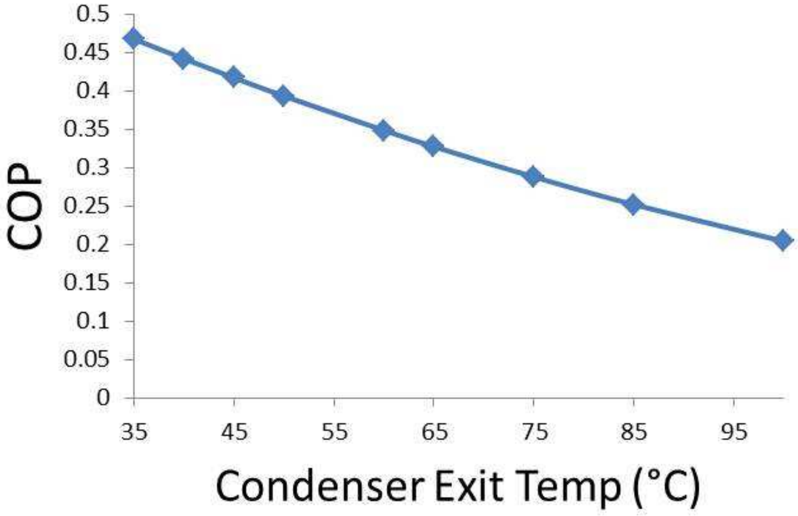

Figure 2-20: COP variation with absorber exit temperature to the pump

2.3.1.10 Influence of pump efficiency

Pump efficiency doesn’t affect the heat rate of any of the components, but lower efficiency increases pumping power which in turn affects the COP. However, pumping power is much lower compared to heat input, so the effect may not be noticeable unless working at much lower efficiency. The heat rate curves and COP are shown in Figure 2-21 and Figure 2-22.

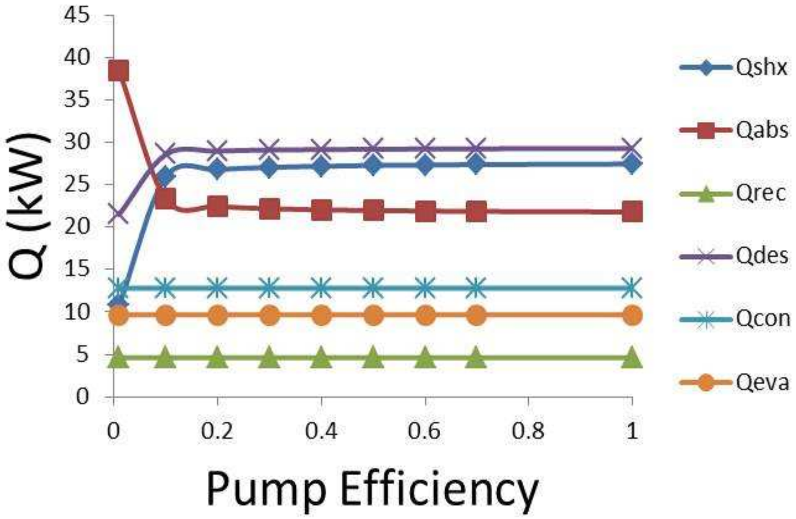

Figure 2-21: Heat transfer rate variation with pump efficiency

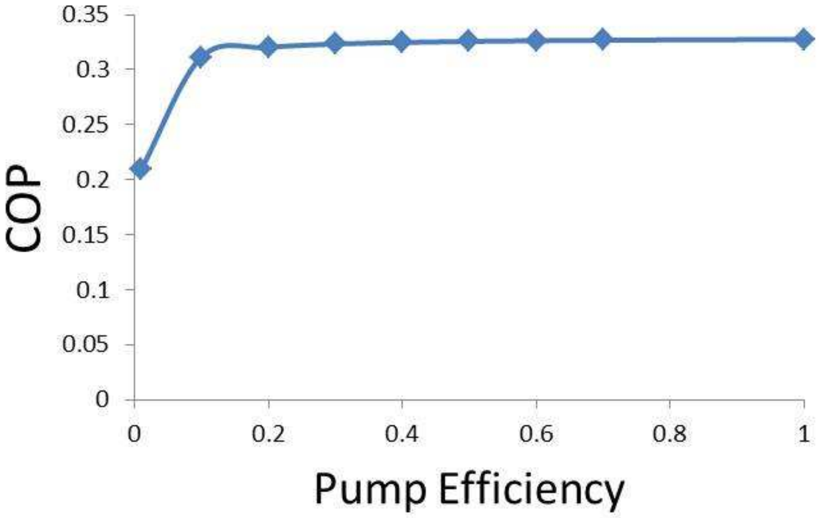

Figure 2-22: COP variation with pump efficiency

2.3.2 Single-stage ammonia-water absorption cycle with precooler

The precooler is added in the loop as shown in Figure 2-25 to utilize the ammonia enthalpy input to the evaporator for preheating the ammonia input to the absorber. The heat exchange in the process serves two objectives: a) It precools the ammonia input to the evaporator; and b) it superheats the evaporator exit vapor which in turns favors the absorber. Both of the these factors helps in widening the enthalpy difference across evaporator, which in turn increase the evaporator cooling capacity and greatly enhance the COP, as shown in Figure 2-23 & Figure 2-24. It can be seen that COP can be increased by 37% with the addition of a precooler. A precooler with zero effectiveness represents the earlier baseline case.

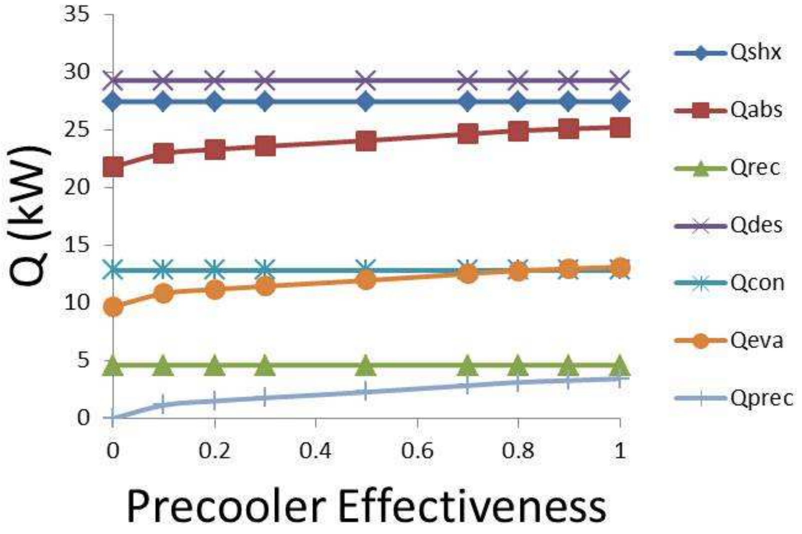

Figure 2-23: Heat transfer rate variation with precooler effectiveness

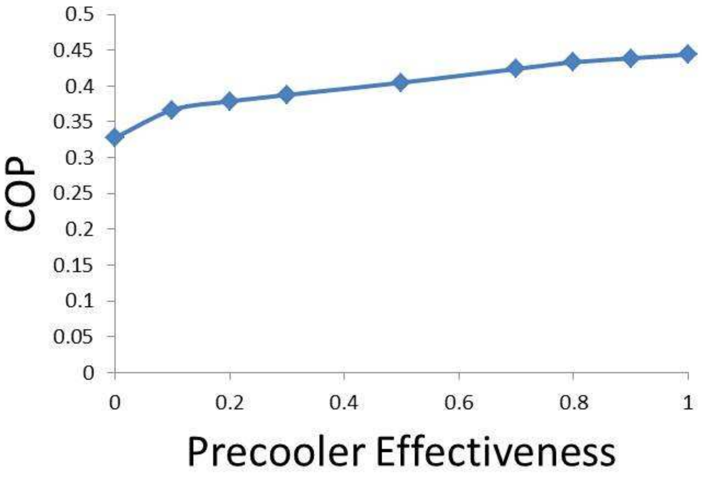

Figure 2-24: COP Variation with precooler effectiveness

2.3.3 Single-stage ammonia-water absorption cycle with precooler and integrated rectifier

The COP of the cycle can be further enhanced by preheating the rich solution mixture by utilizing the heat from the rectifier. This helps to increase the solution heat exchanger effectiveness by reducing the thermal gradient of the solution streams, which in turn enhances the COP as discussed in earlier sections.

A schematic of the full cycle is shown in Figure 2-25.

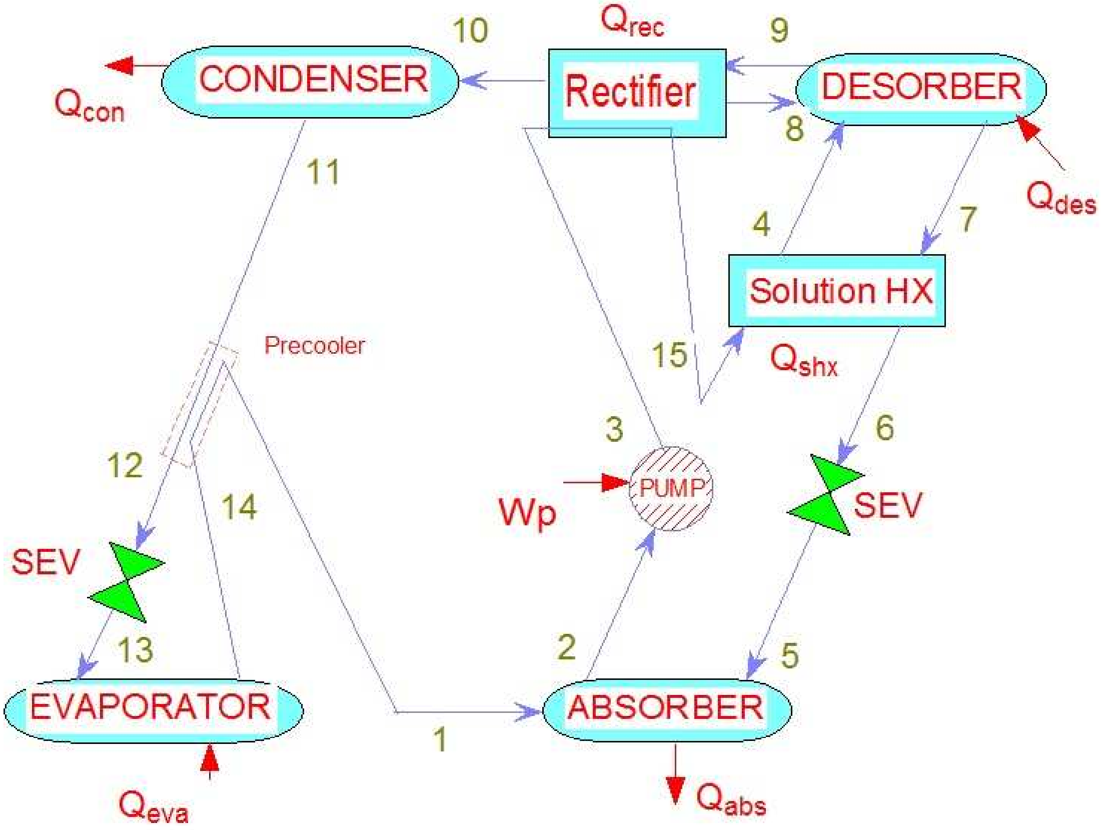

Figure 2-25: Single-stage cycle with precooler and integrated rectifier model in EES

A simulation study was carried out by changing the SHX and precooler effectiveness to check the COP limits. The results are shown in Figure 2-26 and Figure 2-27.

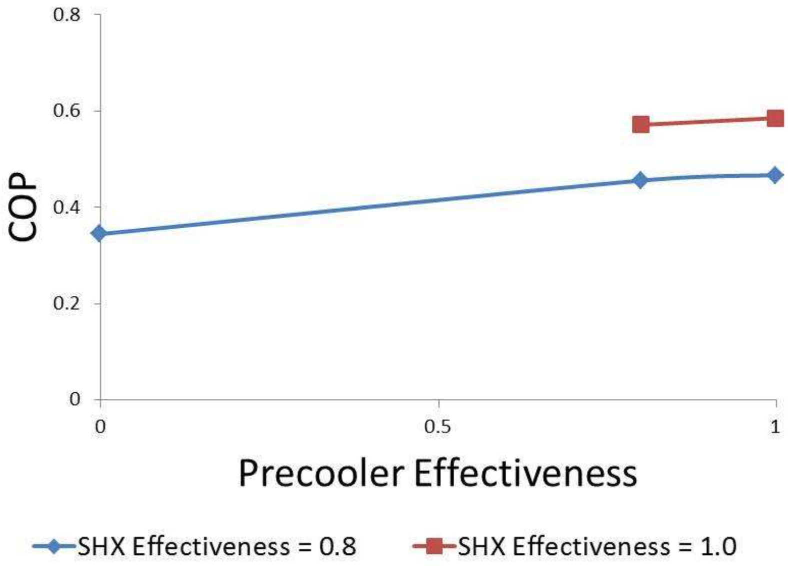

Figure 2-26: COP comparisons with baseline

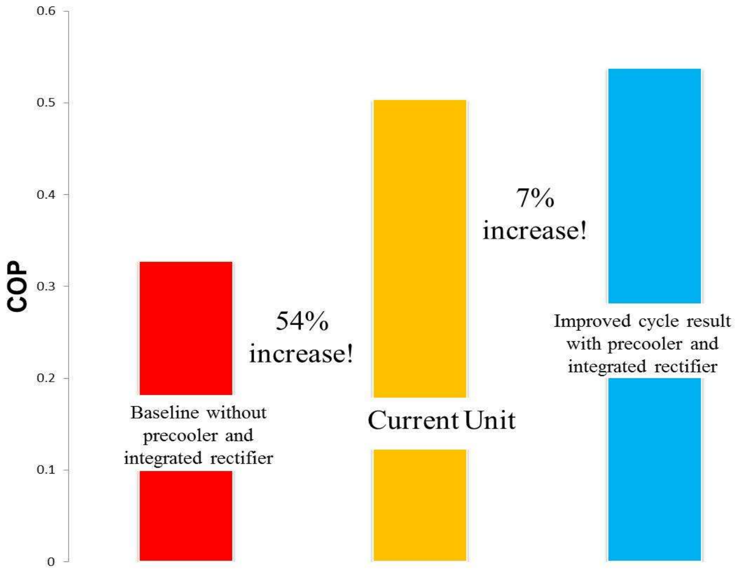

Figure 2-27: Enhancement of COP over existing unit

It can be seen that a maximum COP of 0.5854 can be achieved assuming a fully effective precooler and SHX which is 78% greater than the original baseline value of 0.3227. The current existing unit (at ammonia test-loop facility) had SHX effectiveness of 0.9434 and precooler effectiveness of 0.8706. Using same values for the simulation cycle, it can be seen that COP can be further enhanced by a modest 7%.

2.4 Summary

From the study, it is quite evident that numerous system parameters can significantly affect the COP of an ammonia absorption cycle. As the ammonia-water properties are empirically determined and heavily influenced with thermodynamic state parameters, it is difficult to obtain correlations for performance index. From the limited simulation study performed in current work, the following important conclusions can be drawn:

a) SHX and precooler effectiveness heavily influence the cycle performance. The more effective the heat exchangers, the better the COP of the cycle. Hence, novel design with low thermal resistance compact heat exchangers is needed in the absorption cycle.

b) There is an optimum exit vapor quality for the evaporator where maximum COP can be achieved.

c) Rectifier ammonia mass fraction output is highly critical for overall functioning of the cycle. COP of the cycle is very sensitive to this which makes the efficient rectifier design important for the system.

d) The higher the evaporator exit temperature; the better the COP of the cycle. However this causes a higher system pressure penalty. An optimum space should exist.

e) Higher absorber and condenser temperature significantly decrease the COP.

Based on the above conclusions, further focus was put on component level design specifically for improving the design of evaporator and solution heat exchanger in terms of achieving higher overall heat transfer coefficient. It is shown in further chapters that microchannel technology is a promising candidate for the two-phase heat exchangers design and has been studied for the current development. The next chapter will review existing design methodologies for the evaporator with more focus on review of the literature on microchannel evaporator/heat exchanger design.

CHAPTER 3: LITERATURE REVIEW OF EVAPORATORS DESIGN ENHANCEMENT

This chapter surveys traditional designs of evaporators widely used across industries. More attention is given to microchannel heat exchangers/evaporators and manifold microchannel design available in literature.

A basic review of important correlations used for characterizing two-phase microchannels and single-phase minichannels is also provided in the last section.

As described in Chapter 2, evaporators are an integral part of any refrigeration cycle whose basic function is to evaporate the refrigerant and provide cooling. The basic working principle of an evaporator is the same as a single-phase heat exchanger with the exception that the two-phase process is involved on the refrigerant-side. Refrigerant flowing through the evaporator absorbs energy as it cools a fluid (usually water or air). The saturated refrigerant (usually at a quality of 10% or low) enters the evaporator and exits in saturated or superheated form (depending on design such as flooded or direct expansion coils). The most conventional flow arrangements are co-current and counter-current type. There is more complex flow patterns like cross flow arrangements as well. Typical temperature profiles for co-flow (parallel) and counter flow are shown below in Figure 3-1.

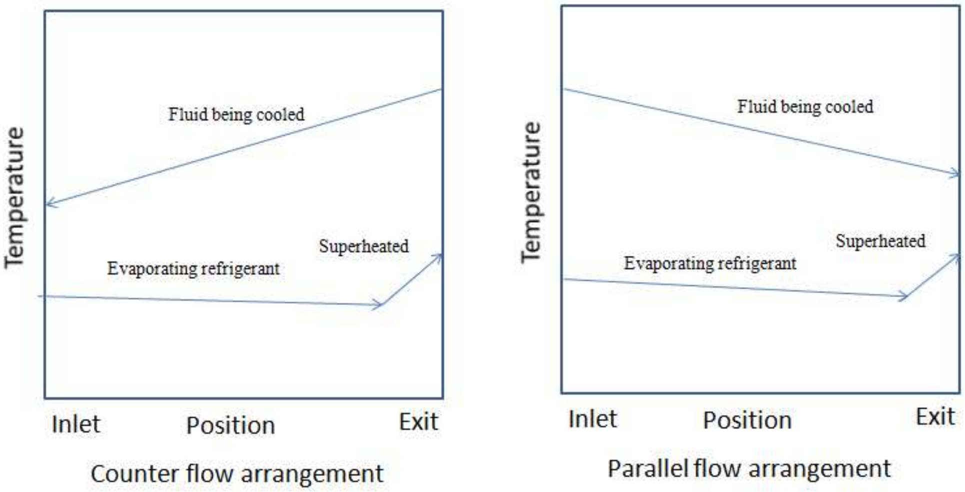

Figure 3-1: Typical temperature profiles for an evaporator

It can be seen from the figures that despite gaining heat, temperature at the exit of the evaporator slightly dips (before superheating) because of the pressure drop. As the pressure decreases, the saturation temperature also decreases.

A typical schematic of the evaporator heat exchange process is shown in Figure 3-2:

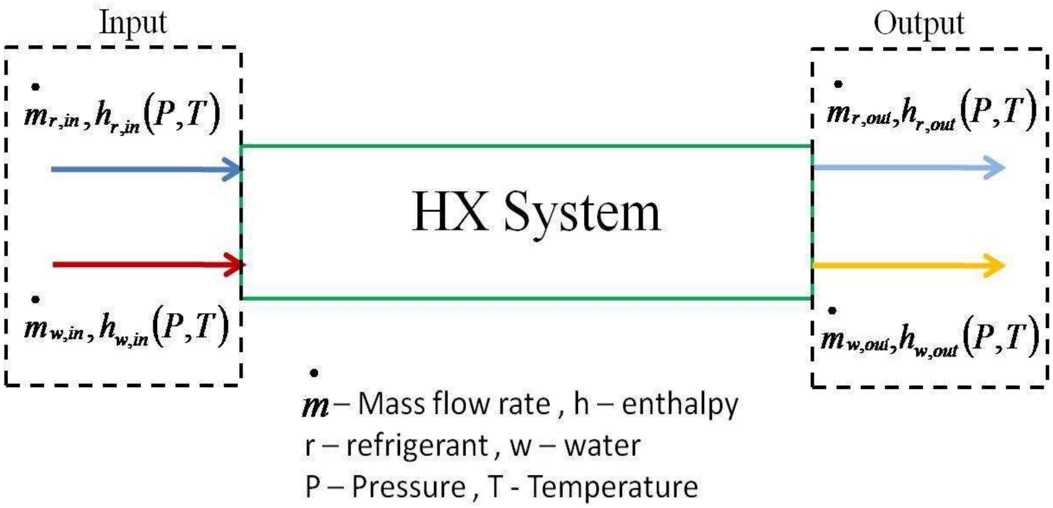

Figure 3-2: Typical evaporator system

The mass balance of the system can be written as

$$\begin{gathered} Mass \quad Balance \\ \dot{m}_{r,in} = \dot{m}_{r,out} \quad ; \quad \dot{m}_{w,in} = \dot{m}_{w,out} \end{gathered} \tag{3-1}$$

If there are no energy losses outside to the system, energy balance can be written as:

$$\begin{gathered} Energy\ Balance \\ \dot{m}_w(h_{w,in} - h_{w,out}) = \dot{m}_r(h_{r,out} - h_{r,in}) = UALMTD \\ LMTD = \frac{(T_{w,in} - T_{r,in}) - (T_{w,out} - T_{r,out})}{\ln\left(\dfrac{(T_{w,in} - T_{r,in})}{(T_{w,out} - T_{r,out})}\right)} \end{gathered} \tag{3-2}$$

where U is overall heat transfer coefficient; A is total heat exchange area; and LMTD is log mean temperature difference.

On the water-side, specific heat can be treated as constant as there is not much temperature difference at the inlet and outlet. On the refrigerant-side, saturated liquid will enter the HX and saturated vapor or vapor/liquid mixture will exit. Evaporator temperature is typically considered as the saturated temperature of the refrigerant.

Using following assumptions as given below:

a) Change in kinetic energy and potential energy both for refrigerant and water is small and is therefore neglected.

b) Properties like specific heat of water are constant in single-phase for small gradient.

c) LMTD correction factor is taken as 1.

Energy balance can be simplified as:

$$\dot{m}_w C_{P,w}(T_{w,in} - T_{w,out}) = \dot{m}_r (h_{r,out} - h_{r,in}) = UA\frac{(T_{w,in} - T_{w,out})}{\ln\left(\frac{T_{w,in} - T_{sat}}{T_{w,out} - T_{sat}}\right)}$$

$$T_{w,out} = T_{sat} + \left(T_{w,in} - T_{sat}\right)e^{-\left(\frac{UA}{\dot{m}_w C_{P,w}}\right)}$$

$$h_{r,out} = h_{r,in} + \left(\frac{\dot{m}_w C_{P,w}}{\dot{m}_r}\right)\left(T_{w,in} - T_{w,out}\right) \tag{3-3}$$

For superheated exits, pressure would no longer be constant, and an appropriate correlation has to be used to take this factor into account to find the temperature and enthalpy relation. Further, due to non-linear complexities, the equation has to be solved iteratively. Heat exchanger effectiveness is another important term to gauge the performance and is typically defined as:

$$\eta = \frac{T_{w,in} - T_{w,out}}{T_{w,out} - T_{r,in}} \tag{3-4}$$

When the outlet water temperature reaches saturation temperature of the refrigerant, the evaporator theoretically has 100% efficiency.

3.1 Classification of evaporator designs

Evaporators are most commonly used in refrigeration and air conditioning applications or in the process and chemical industries. Based on the literatures, a comprehensive list is shown in Figure 3-3 for the most common evaporators used in industry [7].

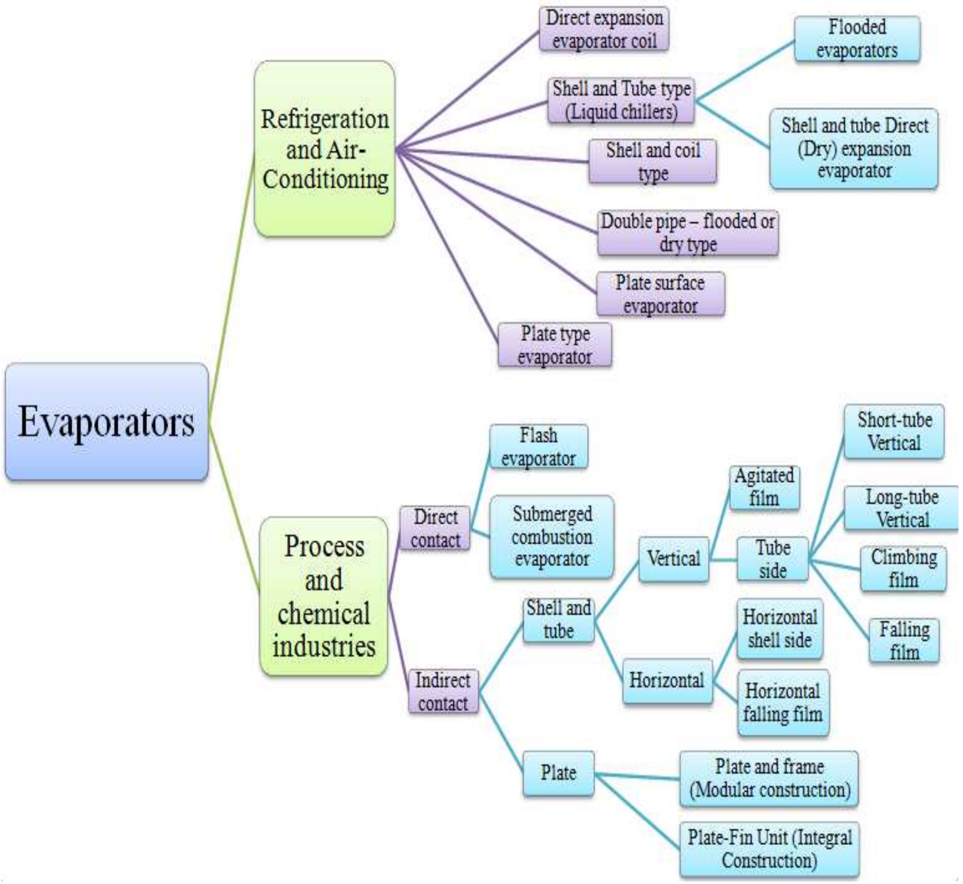

Figure 3-3: Common types of evaporators used in industries

3.1.1 Direct Expansion Evaporator Coil

The evaporator coils used in the present designs often consist of plate-finned tubes with refrigerant flowing inside the tubes and air flowing over the outer tube surface. The capacity of evaporator coils can vary from several fractions of tons for small refrigeration applications to hundreds of tons for large building air conditioning applications. For the outer tube side, both natural convection and forced convection can be used. There are a number of techniques, such as increasing surface roughness, and using swirl flow devices and extended surfaces, by which the inside tube can be augmented to improve the surface area and increase the heat transfer coefficient.

However, more surface roughness and swirling can lead to more pressure drop, which should be minimal to avoid reducing COP. Extended surfaces such as high profile fins, micro fins, annular offset fins, and intersecting fins, are used for HVAC applications. Micro fins are most popular as they give two to three times higher heat transfer coefficients than smooth tubes and it requires less material. However, pressure drop increases by one to two orders. Air-side heat transfer typically occurs with large large circular fins. Based on design considerations and applications, the fins can be further divided into plain, wavy or triangular fins. Coils can be dry or wet type. In the wet type, surface temperature is reduced below the dew point of air and the coil becomes wet, which can affect the heat transfer coefficient. Several designs and correlations have been discussed in literature for different configurations [8-17].

3.1.2 Shell and Tube Flooded Evaporators

Flooded shell-and-tube evaporators cools liquids flowing through tubes by transferring heat to the evaporating refrigerant on the shell side. Tubes are covered with a saturated mixture of liquid and vapor. The refrigerant at low quality (10% or low) enters the shell side through a distributor that evenly distributes the refrigerant over all tubes. As boiling occurs and bubbles rise, the quality of refrigerant increases from the bottom to the top. Level control is needed to make sure that the top row of the tube is completely immersed in refrigerant. This type is more often used with centrifugal compressors. Heat transfer on outside of tubes is dominated by the nucleate and convective boiling regimes. Heat transfer can be augmented using fine pitch finned tubes. Wolverine Tube company makes integral finned tubes with fin densities as high as 40 fins per inch with high aspect ratios. The same company has also provided the high aspect ratio microchannel tubes for the current tubular design which is discussed in later chapters.

3.1.3 Shell and Tube Direct/Dry Expansion Evaporators

Shell and tube direct/dry expansion evaporators are also a form of liquid chillers that are more popular compared than flooded evaporators. The major difference is that a refrigerant flows inside the tubes and a superheat vapor is obtained at the exit. These are used typically with positive displacement compressors such as reciprocating and screw. These heat exchangers are usually designed for horizontal evaporation. The refrigerant enters the heat exchanger through an inlet port and then goes inside the tubes. Micro-fin tubes are also used here for enhancing the heat transfer coefficient on the inner side.

3.1.4 Shell and Coil Type Evaporator

Shell and coil evaporators have a smaller capacity than shell and tube chillers and are usually of the dry-expansion type with refrigerant flowing inside the tubes and chilled liquid in the shell. One or more spiral shaped bare coils can be enclosed in a steel shell based on the cooling capacity requirements.

3.1.5 Double Pipe Type Evaporator

This design consists of two concentric tubes where refrigerant flows through the annular passage and chilled fluid flows through the inner tube. It can be used in flooded as well as dry mode. This requires more space than conventional design and also requires insulation as refrigerant is flowing outside. But the flow is counter type and hence provides higher heat transfer coefficients.

3.1.6 Plate Surface Evaporator

Plate surface evaporators are also known as bonded type evaporators. Two flat plates are embossed in such a fashion that a passage is created for the refrigerant flow. They are used in household refrigerators. There is another type where a thin serpentine tube is sandwiched between plates and the remaining space is either vacuumed or filled with a eutectic solution to make good thermal contact. The design is commonly used in refrigerated trucks.

3.1.7 Plate Type Evaporator

These evaporators are used when a close temperature approach (0.5 K or less) is required between refrigerant and the fluid being chilled. They are widely used in dairy plants for chilling milk. Heat transfer coefficients as high as 4500 W/m^2K for ammonia/water and 3000 W/m^2k for R-22/water are reported. The capacity can be easily changed by increasing or decreasing the number of plates. Arima et al. reported heat transfer coefficient value of 8,000 W/m^2-K for ammonia evaporation with the use of vertical plate evaporator [18].

3.1.8 Horizontal falling film evaporator

Falling film evaporators are used extensively in the chemical, food and process industries. Horizontal evaporators are used typically for desalination of water and in refrigeration technology. The liquid to be evaporated is sprayed on the outside of a horizontal tube bundle and the heating fluid flows inside the tubes. The liquid outside forms a thin film around the tubes and provides high heat transfer coefficients. Distribution of the fluid becomes simpler which can be a huge advantage for the design.

3.1.9 Vertical falling film evaporator

These are used more often than horizontal falling film and work under gravity. The feed liquid is arranged to fall as a thin film down the inside of the tubes and the heating fluid flows on the shell side of the heat exchanger. The main disadvantage of the falling film design is the non-uniform distribution of fluid in and around the circumference of the tube, but it has usually better heat transfer coefficients compared to the shell and tube designs. These evaporators work successfully at lower values of temperature difference between the hot and cold sides of the heat exchanger.

3.1.10 Climbing/rising film evaporator

The climbing evaporator design works on the thermo-siphon principle and has a very similar design as falling film except that the inlet feed liquid comes through the bottom and exits at the top. A pump is used for pumping the feed liquid. The flow in the tubes is relatively low, so a large fraction is vaporized quickly. This results in high vapor velocity, causing the annular vapor-liquid flow. As the annular liquid film is thin, these evaporators provide excellent heat transfer coefficient. They are generally inexpensive to manufacture and requires less floor space.

3.1.11 Agitated thin film evaporator

In the agitated thin film design, the heating liquid flows around the outer jacket and the feed liquid is sandwiched between outer thin jacket and inner revolving rotor. The rotor helps in making a uniform thin film which leads to higher heat transfer coefficient.

3.1.12 Submerged combustion evaporator

These are direct contact evaporator where combustion takes place inside the liquid. This is associated with heat exchange because of the absence of any heat exchanger material. There is no corrosion or fouling issues, but the major disadvantage is the contamination of liquid through direct contact.

3.1.13 Flash evaporator

Flash evaporators were originally applied for producing distilled water in ships and also were also used for desalination of water. There is no external heat transfer surface and hence no fouling problem occurs. Water is heated and introduced into a chamber, which is kept at lower pressure than corresponding saturated pressure of heated water. Upon entering a chamber, a small portion is instantly evaporated in a flash, which is then passed through moisture separator to remove any entrained liquid and condensed to form distilled water.

There are additional classifications of heat exchangers available in literature. Most of the design discussed here is quite established in industry but not enough documented literature is available in terms of performance or heat and mass transfer characterization because of proprietary restrictions. It is not possible to compare all design in terms of a common performance index as each one has its own advantages and disadvantages. For ammonia/water absorption systems, falling film evaporator are used in large industries because of good heat transfer coefficients. For small capacity absorption systems, plate evaporators are widely used because of design compactness and excellent heat transfer coefficients. Another breed of heat exchangers based on microchannel technology has been widely discussed in literature. Microchannel heat exchangers have very high surface area/volume (10,000 - 50,000 m^2/m^3) compared to 300 – 600 m^2/m^3 of conventional heat exchangers. Also, heat transfer coefficients associated with such designs are much higher due to smaller hydraulic diameters. Further sections of the chapter briefly discuss the literature work available related to microchannel evaporator designs.

3.2 Review of microchannel evaporators

In last decade, microchannel technology has gained popularity for electronics cooling for high heat flux dissipation. Some of the important review papers by Morini et al., Thome et al., Garimella et al., Kandlikar et al. discuss the thermal transport phenomena related to both single-phase and two-phase flow inside microchannels and compare several experimental results in a comprehensive way [19-24]. As the microchannels are associated with smaller hydraulic diameters and flow boiling utilizes latent heat, very high heat transfer coefficients are obtained. The same technology has been utilized for the development of microchannel evaporators. Few works in the literature demonstrate successfully running a small refrigeration cycle for cooling electronic packages at laboratory scale.

Companies like Delphi have been developing high efficiency microchannel evaporators [25]. The evaporators are constructed of brazed aluminum and consists of three components- a flat microchannel tube, fins and two refrigerant manifolds joined together. These evaporators are suitable for use in residential air conditioning, commercial cooling/heating and refrigeration applications. Hermetically sealed microchannel heat exchangers have also been developed at Velocys for cryogenic applications, high temperature reactions and distillation.

A comparison has been drawn among widely used heat exchangers as shown in Table 3-1 showing the superiority of microchannel technology over other technologies.

Table 3-1 : Heat exchanger performance comparison

Parameter	**Microchannel HX**	**Shell & Tube HX**	**Compact HX**
Surface area per unit volume (m^2/m^3)	10,000-50,000	50-100	850-1500
HTC (liquid, W/m^2K)	> 7000	~ 5000 (tube side)	3000-7000
Approach temperature	< 10 ^oC	~ 20 ^oC	~ 10 ^oC

Kim et al. developed and verified a heat exchanger finite volume model for evaluating the thermal performance of a microchannel evaporator for a CO_2 mobile air-conditioning system. Heat transfer and pressure drop correlations were evaluated for both wet and dry air and refrigerant-sides. Several correlations for both air and refrigerant-sides have been compared for folded multi-louvered fin geometry. The numerical model has good agreement in terms of cooling capacity (± 2.6%) and refrigerant-side pressure drop (± 13.6%) [26].

Mudawar et al. did an extensive study for evaluating two-phase heat transfer coefficient and pressure drop for a microchannel heat sink using R134a as the working fluid. The microchannels were formed by machining 231 µm wide x 731 µm deep grooves on the copper surface. Mass flux from 127-654 kg/m^2-s and heat flux in the range of 31.6-93.8 W/cm^2 was tested. Heat transfer coefficient in excess of 50,000 W/m^2-K was observed but was found to decrease sharply with increasing vapor quality. With increasing heat fluxes, heat transfer coefficient was observed to increase. Pressure drop in excess of 200 mbars was observed as well. Key findings of the study were the dominance of the bubbly flow and nucleate flow boiling regimes at lower heat fluxes leading to lower vapor quality ($x_e < 0.05$). High fluxes produced medium quality ($0.05 < x_e < 0.55$) or high quality ($0.55 < x_e < 1.0$) flows where heat transfer was dominated by annular film evaporation. The pressure drop generally increased with increasing mass flux but there was an appreciable diminution where complete conversion to vapor took place inside the micro-channels [27].

Yun et al. measured convective boiling heat transfer coefficients and two-phase pressure drops of R410A in rectangular microchannels with hydraulic diameters of 1.36 mm and 1.44 mm. Mass fluxes was varied between 200 to 400 kg/m^2-s and heat flux was varied between 10-20 kW/m^2, as the saturation temperatures were maintained at 0, 5 and 10 °C. The experimental data for heat transfer coefficient was within a deviation of 18% with the existing correlation for large diameter tubes but pressure drop had similar trend. Heat transfer coefficient in excess of 20,000 W/m^2-K and maximum pressure drop of 100 mbar per meter was observed. With increasing saturation temperature, heat flux and mass flux, heat transfer coefficient was found to generally increase for medium and higher vapor qualities [28].

Mongia et al. developed a small-scale refrigeration system for cooling high-power components in notebook form factors. The refrigeration system was based on vapor compression cycle and had miniaturized components with iso-butane as the working fluid. A COP > 2.25 was achieved. A copper based evaporator with parallel microchannels of 80 µm size was used to cool the hotspot. The condenser was designed to achieve thermal resistance of 0.5 °C/W and was controlled mainly by heat transfer on the air side [29].

Joshi et al. evaluated design and thermo-hydraulic performance of high heat flux evaporators suitable for interfacing the microprocessor chip with a cascaded R134a/R508b vapor compression refrigeration system at –80 °C. A different set of compact evaporator design was examined for a heat flux ranging between 20 W/cm^2 and 100 W/cm^2. The microchannel evaporator consisted of 13 channels that were 1.2 mm deep and 400 µm wide with a spacing of 800 µm. Heat transfer coefficient in excess of 45,000 W/m^2-K was observed at a refrigerant flow rate of 70 g/min. Pressure drop was observed between 50-100 mbar for a varied heat flux range of 20-100 W/cm^2 [30].

Edvin et al. did an experimental study on phase change cooling of high heat flux electronics utilizing an innovative phase change technique involving force-fed evaporation and condensation. High-performance micro-structured surfaces consisting of alternating fins and channels coupled with the force-fed mechanism were used for the evaporator and condenser. The force-fed mechanism provided a highly vigorous micro-channel convective heat transfer environment and low pressure drop due to smaller flow lengths. For the evaporator, heat flux levels above 300 W/cm^2 with wall heat transfer coefficients more than 45,000 W/m^2-K using HFE-7100 as the working fluid. For the condensation mode, heat fluxes up to 56 W/cm^2

with heat transfer coefficients of 32,000 W/m^2-K were achieved using the same fluid. Pressure drop was at a maximum of 10 mbar at mass flux of 25 kg/m^2-s for condenser test section. The force-fed method utilizes an inlet header placed on top of the micro-structured surface to direct the working fluid on the heat transfer surface. The liquid evaporates as it passes a short distance through the micro-channel and the vapor flows out of the channel back into the header, which has specific channels for directing vapor out of the area. The result is the formation of a liquid vapor flow pattern that provides a continuous supply of liquid working fluid beneath the escaping vapor [31].

Hrjnak et al. developed microchannel heat exchangers for charge minimization in air-cooled ammonia condensers and chillers. Microchannel tubes of hydraulic diameter of 700 µm were tested and compared with other designs. Air side heat transfer coefficients of 60-180 W/m^2-K were obtained at an air velocity between 1-5 m/s. The microchannel condenser charge per capacity ratio was found to be 76% less than the macrochannel serpentine condenser. As the microchannel design was light weight and made of aluminum, it is suitable use for automobile applications [32].

Cao et al. developed a counter flow microchannel plate heat exchanger utilizing the similar flow principle of corrugated plate heat exchanger. Channels with 400 µm size were etched on stainless steel plates. Maximum volumetric heat transfer coefficient of 5.2 MW/m^3-K with a corresponding pressure drop of less than 20 kPa under a Reynolds number of 65 was reported [33].

Anurjew et al. presented different microstructure devices used for evaporation and generation of steam. They found that long, straight microchannels are not optimal for evaporation. A new design based on circular blanks, including numerous circular or elliptic sidewalls, showed the full evaporation and superheating [34].

Qi et al. developed two retrofitted compact and high efficient microchannel heat exchangers. The microchannel heat exchangers were reported to be 15% less in weight and size for condenser design. The evaporator had a maximum cooling capacity close to 6 kW at air volume flow rate of 500 m^3/hr with a pressure drop of 160 Pa. Maximum refrigerant mass flow rate was 160 kg/hr with a pressure drop of 90 kPa. The condenser had the maximum heat rejection rate close to 11 kW at air velocity of 4.5 m/s with a maximum pressure drop of 130 Pa. Maximum refrigerant-side pressure drop was 110 kPa at 150 kg/hr charge flow rate [35].

Thome et al. tested three different micro-evaporator cooling cycles: one with a pump, one with a compressor and one with a hybrid of the two together for cooling a computer blade server. For an evaporating temperature of 60 °C, subcooling of 5K and outlet vapor quality of 30%, the predicted CHF was about 2.2 times the maximum heat flux of the blade server using fins that had 170 µm wide channels, 170 µm fin height and fin thickness. The accuracy in predicting critical heat flux was around 20% [36].

A summary of the above literature is shown in Table 3-2.

Table 3-2: Literature summary of microchannel evaporators

Authors	Type of Study	Hydraulic diameter	Reynolds number; Flow regime; Fluid	Max HTC; Min thermal Resistance; Max pressure drop ; Max heat flux
Kim & Bullard, 2001	Numerical	~mms	CO_2/Air	300 Pa for air, 300 kPa for CO_2

Owhaib et al., 2004	Experimental	1.7,1.224,0.826 mm	R134a	15000 W/m^2-K
Lee & Mudawar, 2004,2005	Review	Wide	R134a	57000 W/m^2-K; 21000 Pa
Yun et al., 2006	Experimental	1.36,1.44 mm	R410A	20000 W/m^2-K; 50 kPa/m
Mongia et al.,2006	Experimental	350 µm	Multiple	0.28 °C/W
Lee & Mudawar,2006	Experimental	349 µm	R134a	100 W/cm^2; 125 kPa
Trutassanawin et al., 2006	Experimental	-	R134a	0.60 °C-cm^2/W
Wadell et al., 2007	Experimental	600 µm	R134a/R508b	30000 W/m^2-K; 30 mbars
Baummer et al., 2008	Experimental	77-142 µm	HFE-7100	100000 W/m^2-K; 300 W/cm^2
Hrnjak et al., 2008	Experimental	0.7 mm	Ammonia/air	110-192 W/m^2-K
Brix et al., 2009	Experimental	0.96 mm	R134a	0.05 bars
Cao et al., 2009	Experimental	301-392 µm	10-70; Water	5.2 MW/m^3-K; 29 kPa
Qi et al., 2009	Experimental	~ mms range	Air	100 Pa
Anurjew et al., 2010	Experimental	-	Water	-
Qi et al., 2010	Experimental	~ mms range	R134a/Air	180 Pa
Marcinichen et al., 2010	Experimental	-	R134a, R245fa	-
Khan & Fartaj, 2010	Review	0.001-4.1 mm	Wide	-

The current work described in this thesis is based on the manifold microchannel philosophy as mentioned in the work of Edvin et al. with the difference that it is being used for low heat flux. The design has existed in literature for last decade and has sizable advantage in terms of reducing the pressure drop. A comprehensive summary of the manifold microchannel design is provided in the further section.

3.3 Review of manifold microchannel designs

Manifold microchannel design has been in existence for the last decade and several novel concepts have been tested at the laboratory scale. The earliest work for the study of fluid flow and heat transfer is available in the work of Harpole and Eninger [37]. They developed a two dimensional flow/thermal numerical model of the micro-channel heat sink and were able to demonstrate cooling of 1 kW/cm^2 heat flux with water methanol mixture with top surface temperature of 25 °C. Microchannels were etched on silicon and a diamond sheet was attached to further maintain the uniform heat flux utilizing its isotropic properties. Several design parameters with respect to geometry and fluid flow were proposed to achieve a heat transfer coefficient of 100,000 W/m^2-K within a total pressure drop of 2 bars. They recommended combining the heat exchanger into the heat source to minimize the overall thermal resistance. The pressure drop in the header and manifold was not considered in the 2-d model, but they recommended keeping the manifold flow areas larger.

Copeland et al. performed a numerical study of a manifold microchannel heat sink. The heat sink was made of silicon and was cooled by a fluorocarbon liquid. The assembly was modeled using a unit cell bounded by the centerlines of the manifold inlet and outlet channels and those of the microchannels and heat sink walls. Three dimensional finite element models of single manifold microchannels were used to simulate fluid and heat transfer behavior. A parametric study was conducted for various geometrical and flow parameters including inlet velocity, microchannel flow length, microchannel depth, microchannel width, fin width and heat flux. The simulation was carried out for both constant heat flux and constant temperature boundary conditions. The model neglected the pressure losses at inlet and outlet of the microchannels due to flow contraction and expansion complexities. The results indicated high heat transfer regions near the inlet. At higher inlet velocities, secondary maxima in heat transfer were also observed at the microchannel base below the inlet and also at top of the microchannel near the exit. It was shown that channel length had nearly no effect on thermal resistance, though the pressure drop reduced significantly with reducing flow length [38].

Kim et al. performed an experimental study of manifold microchannel heat sinks using forced air. They investigated the effects of geometrical parameters on the thermal performance of the heat sinks for optimal design. The thermal resistances of the manifold design were also compared with those of traditional microchannel design. The experimental results indicated that thermal resistances of the manifold design are strongly influenced by the pumping power, microchannel width, and manifold inlet/outlet channel width and microchannel aspect ratio. The microchannel thickness and the depth had a weak effect on the results. It was also observed that thermal resistance of the heat sinks decreased with increasing microchannel depth and thickness-width ratio. Further, under the optimal conditions of the geometrical parameters, the thermal resistance and pressure drop was observed to be 35% lower than the traditional design [39].

Poh and Ng performed numerical analysis for fluid flow and heat transfer inside manifold microchannels. A numerical model was prepared in ANSYS and 16 different set of parameters were studied. Pressure, temperature and velocity contour plots were obtained and analyzed. The results were compared with an analytical model and a large dependence on flow rate was found. However, weak dependence was found with the microchannel aspect ratio. Thermal resistance was found to increase with decrease in inlet velocity, channel width and channel depth. It was concluded that the results of two models are not very accurate as interfacial effects were neglected in the finer narrow channels. Effects of coolants also needed to be analyzed, as gaseous and liquid coolants can differ significantly flow phenomena. As uniform heat flux does not exist for micro-scale devices, a conjugate analysis would also be needed [40].

Ryu et al. did a three-dimensional analysis for evaluating the thermal performance of the manifold heat sink and used the steepest descent algorithm for obtaining the optimal geometrical dimensions. The optimal channel depth, channel width, fin thickness, and inlet/outlet width ratio yielded the lowest thermal resistance for the specified number of manifolds and a given pumping power. It was concluded that 95% of the heat is removed through the fin surface and the lowest temperature was found in the vicinity of the channel entrance point. The hottest point was observed near the inlet and outlet stagnation points in the channel base. It was claimed that thermal resistance is lowered by 50% for identical heat load and pumping power when compared to traditional microchannel heat sink design. Channel width and channel depth were found to be more critical parameters affecting the thermal performance. A power-law dependence on pumping power was found to exist for optimal dimensions and corresponding thermal resistance. However, Reynolds number did not affect the optimal aspect ratio of the channel cross-section [41].

Jang & Kim experimentally investigated the thermal characteristics of a microchannel heat sink with impinging jet which closely resembles the manifold design. In order to evaluate the cooling performance, pressure drops across the microchannel heat sink and base temperature distributions were measured. A correlation for the pressure drop and thermal resistance was demonstrated to be within 10% of the experimental result. It was concluded that cooling performance of an optimized manifold heat sink with an impinging jet is enhanced by 21% when compared to an optimized microchannel heat sink when pumping power is 0.08W and channel height is 2.2 mm [42].

Jankowski et al. tested two different methods by integrating microchannel coolers for reducing overall thermal resistivity. In the first approach, they tried direct fluid impingement on the die using the silicon manifold microchannel design. For the second design, they fabricated a standard parallel microchannel design into an aluminum nitride substrate. As non-optimum microchannel design was used, both design had comparable performance for operating pressures below 35 kPa. Both devices were tested for flow rates ranging from 40-60 mL/min with thermal resistivity obtained in order of 0.13-0.19 °C-cm^2/W [43].

Wang et al. performed ANSYS CFX simulation of a manifold heat sink and concluded that it has a higher heat transfer efficiency/rate than conventional structures. Infrared test were performed to determine the dependence of substrate steady-state temperature on flow rate where water was used as the working fluid. The maximum heat flux input of the microchannel heat sink was found to be 75% lower than the conventional unit cell for a normal working temperature of 353 K under the same boundary conditions. They demonstrated a maximum heat flux input of 104000 W/m^2 for 6.7 ml/min with surface temperature of 80.2 °C [44].

Wang and Ding presented their previous work for a manifold heat sink integrated with a high-efficiency copper heat spreader and made some additional conclusions. The temperature rise along the flow direction was found to decrease significantly, a result of entrance effects in the transverse channel arrays. The effect was demonstrated through higher heat fluxes obtained near the traverse channel array inlet. The manifold design was found to have much better heat transfer efficiency than conventional heat sinks for all the boundary conditions considered [45].

Xia et al. studied the effect of surfactants on friction pressure drop in a specifically designed manifold microchannel heat sink. A cross section of 100 µm x 300 µm with a length of 10.0 mm microchannel was used. An anionic surfactant of 100 ppm sodium dodecyl sulphate (SDS with 95% purity grade) aqueous solution and a new type of 300 ppm green non-ionic alkyl polyglycoside (APG1214 with 98% purity grade) aqueous solution were used as working fluids. It was found that drag reductions were dependent on flow velocities and fluid temperatures. The drag reduction was not significant for laminar flow but increased in the transition flow regime. It was concluded that temperature rise can promote drag reductions in the presence of SDS and APG. APG was found to be better than SDS at high temperatures for drag reductions [46].

Haller et al. performed the simulation and experimental investigation of pressure loss and heat transfer in microchannel networks containing bends and T-junctions. The test structure was made of silicon, and the pressure loss and heat transfer for

Reynolds numbers ranging from 10 to 3000 were investigated. The results demonstrated that enhancement in heat transfer can be achieved by redirecting and splitting the fluid. Due to vortices present in the curved flow, the temperature gradient was found to increase at the wall, leading to enhanced heat transfer. However this enhancement came at a high pressure loss penalty. It was further concluded that shapes with higher pressure losses have higher effectiveness. It was not feasible to find a mathematical model to evaluate the pressure losses of the distributed laminar flow with vortices in bent microchannels. More experimental evaluations of different shape and aspect ratio would be necessary to calculate pressure losses for more complex structures [47].

Kermani et al. fabricated and tested a novel manifold microchannel heat sink for cooling concentrated solar cells. The microchannels were micro-fabricated and integrated on the backside of the silicon substrate, and the manifold was fabricated on another silicon substrate. Manifolds were etched in 1 mm thick silicon wafer having depth of 500 µm. The inlet and outlet holes were made on the back side of the wafer having 1 µm thermally grown silicon oxide. Microchannels were etched in 0.5 mm thick silicon wafer with 200 µm depth. The experimental results demonstrated that heat transfer coefficients of 65480 W/m^2-K can be achieved at a flow rate of 1.1 g/s and a heat flux of 75 W/cm^2 can be achieved using water as the cooling fluid. For all cases, flow was in the thermal entry region and the Nusselt number was not constant. Moderate pressure drops were recorded during the experiments that corresponded to moderate pumping power requirements for the cooling system. It was suggested that in order to have high heat transfer coefficient and low pressure drop, microchannel and manifold channel dimensions need to be optimized. [48].

Escher et al. conducted an experimental investigation on an ultrathin manifold heat sink which consisted of impinging liquid slot-jets fed with liquid coolant. A closed fluid loop for precise hydrodynamic and thermal characterization of six different test vehicles was also built. The influence of the number of manifolds systems, microchannel width, volumetric flow rate and the pumping power on the hydrodynamic and thermal performance of heat sink was studied. A design with 12.5 manifold systems and 25 µm wide microchannels as the heat transfer microstructure provided optimum choice of design parameters. A total thermal resistance between maximum heater temperature and fluid inlet temperature of 0.09 cm^2-K/W with a pressure drop of 0.22 bars on a 2 x 2 cm^2 chip was demonstrated for a volumetric flow rate of 1.3 l/min. Cooling power densities of more than 700 W/cm^2 for a maximum temperature difference between the chip and fluid inlet of 65 K were demonstrated. The heat sink height did not exceed 2 mm and included a 500 µm thick thermal test chip structured by 300 µm deep microchannels for heat transfer. The influence of elevated fluid temperatures demonstrates enhancement of heat sink cooling efficiency of more than 40% for a temperature rise of 50 K [49].

Sharar et al. fabricated, tested and provided the experimental results for a four-chip aluminum nitride direct-bonded-copper manifold microchannel cooler with water at 25 °C and 80 °C and three vehicular coolant fluids at 80 °C with a maximum allowable pressure drop of 5 psig. The total stack resistivities varied from 0.316-0.628 K-cm^2/W within 5 psig limits depending on the coolant fluid used. It was concluded that geometric optimization and comprehensive manifold study is needed to implement manifold microchannel cooler in a real hybrid vehicle system [50].

Cetegen provided a detailed study of a manifold microchannel system for both single and two-phase fluids in his dissertation [31]. A numerical study for single-phase heat transfer and fluid flow was carried out using Gambit & ANSYS Fluent, and parametric analysis related to important geometrical and fluid flow parameters was performed. Effects of fin thickness, fin height, microchannel width, inlet and outlet feed channel width, microchannel length, microchannel surface base thickness and manifold height were studied for the practical fabrication limitations. The fins were fabricated through micro deformation technology of Wolverine Inc. The sample geometry was numerically investigated for fluid flow and heat transfer behavior. At lower Reynolds numbers, fluid flow occurred through a bypass zone between inlet and outlet feed channels at the top of the microchannel. The effect in turn created dead zones at the bottom of the microchannel and significantly affected the heat transfer rate. Increasing the mass flow rate and Reynolds number pushed the fluid core to the bottom of the microchannels and created a fluid recirculation zone on the top part of the channel. An increase in fluid velocity also helped create secondary flows which appeared in the form of vortex pairs in the microchannel cross section. Further, effects of geometrical parameters on pumping power were studied for fixed heat transfer coefficients values. It was concluded that geometrical parameters had conflicting effects on fluid flow and heat transfer behavior and hence an optimum point or space should exist. But due to large number of parameters, it was difficult to obtain the optimal conditions. An attempt was made to optimize the geometry using

Approximation Assisted Optimization coupled with a numerical solver. The following important conclusions were made from the single-phase study:

- At lower Reynolds numbers, the optimum design favors larger fin heights, high fin aspect ratio and larger hydraulic diameters. Larger feed channel dimensions preferred with inlet channels slightly smaller than outlet channels.
- At higher Reynolds numbers, both heat transfer coefficients and pumping power have a monotonic increasing trend. In general, the optimum design favors smaller microchannel and manifold dimensions.
- Due to smaller microchannel length and conductive structures, thermal gradients along longitudinal direction are smaller, which is beneficial to attain uniform surface temperature.
- The optimum values can be further reduced for higher Reynolds numbers if it micro deformation technology is feasible for such smaller channel dimensions.

A summary of the above literature is provided in Table 3-3.

Table 3-3: Literature summary of manifold microchannel design

Authors	Type of Study	Hydraulic diameter (µm)	Reynolds number; Flow regime; Fluid	Max HTC; Min Thermal Resistance; Max Pressure drop ; Max Heat Flux
Harpole & Eninger,1991	Numerical	15-66	15-400; Water	1000000 W/m^2-K 1 kW/cm^2, 1-2 bars
Copeland et al., 1996	Analytical, Numerical	113-226	Laminar; Water	0.27 °C/W, 0.1216 bars
Kim et al.,1998	Experimental	700-2000	Laminar; Air	0.2 °C/W, 4200 Pa

Ng & Poh, 1999	Numerical	113-226	10-800; Laminar; Water	0.34 °C/W, 4333 Pa
Ryu et al., 2003	Numerical	10-60	1-100; Laminar; Water	0.031 °C/W
Jang & Kim, 2005	Experimental	343-379	0-500; Air	30000 W/m^2-K , 409.8 Pa
Jankowski et al., 2007	Experimental	40-760	Laminar; Water	0.131 °C-cm^2/W, 35 kPa
Wang et al., 2007	Experimental	134	Laminar; Water	203000 W/m^2
Xia et al., 2008	Experimental	200	100-3500; Aqueous Surfactant Solution	-
Haller et al., 2009	Experimental, Numerical	10-3000	10-3000; Water	11000 W/m^2-K; 340 mbars
Kermani et al., 2009	Experimental	36,67	Laminar; Water	75 W/cm^2, 22 kPa
Escher et al., 2010	Experimental	46	Laminar; Water	700 W/cm^2; 0.09 cm^2-K/W
Jankowski et al., 2010	Experimental	272	Laminar; Water	0.316 K-cm^2/W; 7 psig
Cetegen, 2010	Numerical, Experimental	21-60	HFC	1230 W/cm^2; 330000 W/m^2-K;

3.4 Tubular evaporator single-phase and two-phase correlations for heat transfer coefficient and pressure drop

The system under the current study is a microchannel-based evaporator that involves flow boiling physics inside microchannels at the refrigerant-side. Significant literature is available regarding the two-phase flow regime inside the microchannels; which influence the heat transfer process. Most of these investigations are empirical in nature due to complex nature of the fluid flow combined with evaporation. With the use of manifold guided flow, entrance region effects are also present, which makes any present model inapplicable. On the inner side of the heat exchanger, fluids flow through comparably bigger triangular minichannels, which is essentially single-phase flow through small channels. Limited correlations are available in the literature to determine the fluid flow and heat transfer behavior for both kinds of flow and geometry. Better method in terms of numerical simulation can be used to get more accurate results. In further chapters, various numerical simulation results will be presented based on header types which help in evaluating in the water-side heat transfer coefficient. Experimental testing of the evaporator is non-intrusive and all the flow and temperature conditions are measured at the inlet and outlet of the flow. A data reduction method is provided in the form of correlations to determine the overall heat transfer coefficient using overall cooling capacity; base heat transfer area and log mean temperature difference.

The tubular evaporator design is the combination of a several small heat exchanger surfaces working alternately in the co-current and counter-current modes. As the measurements are non-intrusive due to the pressurized nature of the system, parameters cannot be evaluated at internal geometries. An approximate data reduction based on average inlet and outlet conditions is used to evaluate overall heat transfer coefficient and pressure drop. Also, it is important to consider the energy losses to the surrounding environment, which can be evaluated using a thermal resistance network. A schematic of the fluid flow is shown below in Figure 3-4.

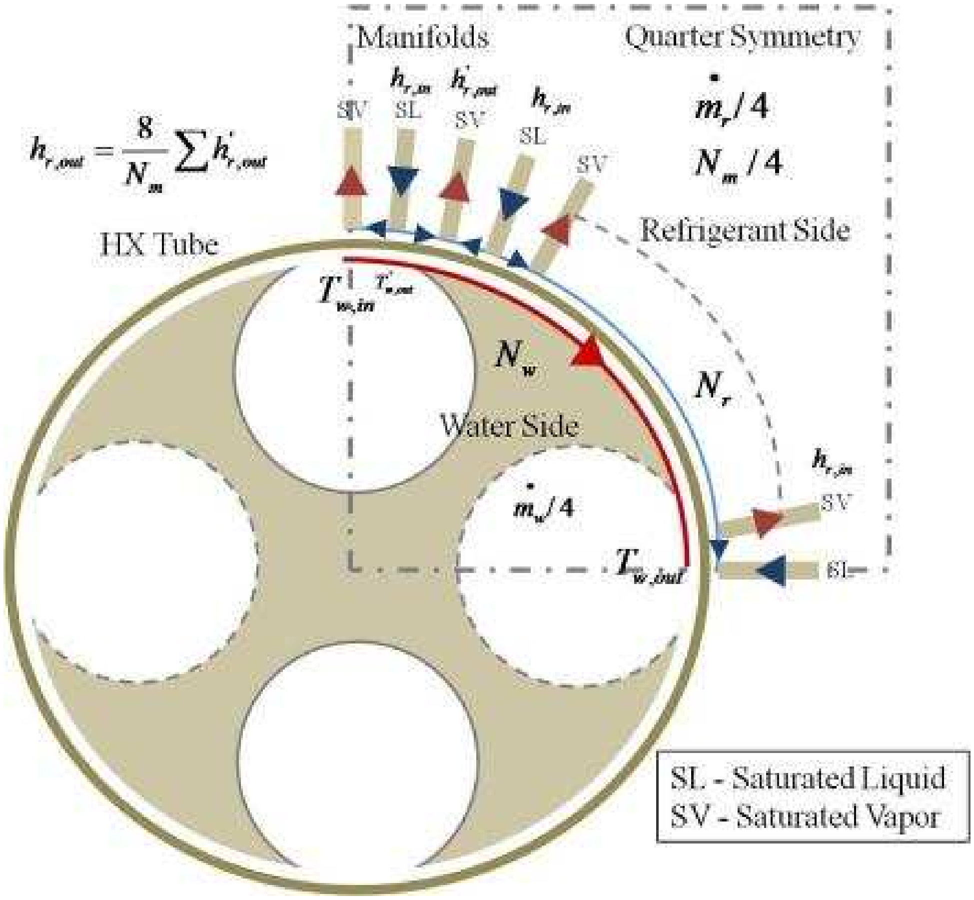

Figure 3-4: Schematic of the fluid flow

As seen in the schematic above, water enters through the solid circular region perpendicular to the page and travels along the surface of the tube and comes out of the dashed circular region. Due to the quarter-symmetry nature of the heat exchanger process, the mass flow rate is assumed to be equally divided in all the four quarters.

On the refrigerant-side, multiple U-channel flow would be present. Saturated refrigerant liquid enters through alternate inlet manifolds and saturated or superheated vapor exits through the alternate outlet manifolds. It is assumed that inlet mass flow rate is equally divided across all inlet manifolds and also along the length of the tube for sake of simplicity. The ultimate objective is to achieve a uniform manifold microchannel elemental volume, which will be discussed in Chapter 4 and can be scaled for calculating the overall cooling capacity.

Some important assumptions have been made as follows:

a) Flow length on both sides was assumed to be the same for the sake of simplicity. Flow is uniform and symmetric circumferentially and axially in all channels. For the saturated vapor/liquid mixture exit, flow arrangement (parallel/counter-current) will not affect the LMTD value. But for superheated exits, it would be considered.

b) Heat loss is assumed to occur through natural convection to ambient from the outer tube surface area, as it is not insulated. However, heat loss would be much smaller considered for cooling capacity, which is studied here. It is also assumed there is no thermal gradient between the outer tube and HX tube surface so that the primary heat exchanger surface remains the microgroove surface.

c) Fouling resistance is assumed to be negligible for calculating overall thermal resistance.

If the symmetric unit cell is considered based on the manifold flow symmetry in circumferential direction, the following thermal resistance network can be prepared as shown in Figure 3-5.

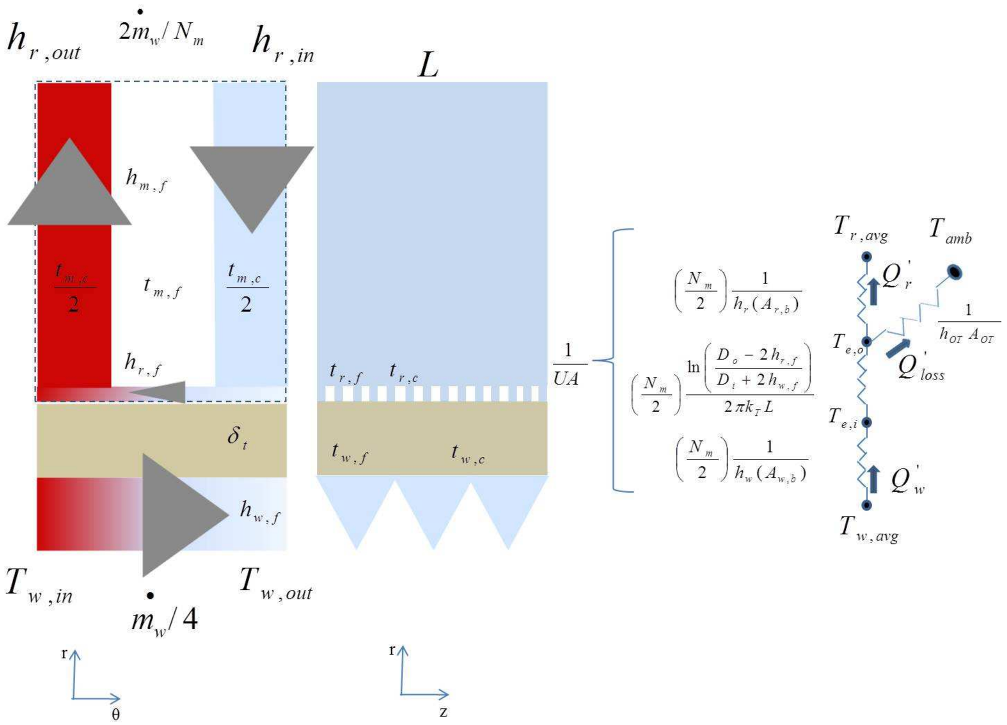

Figure 3-5: Unit cell thermal resistance network

The thermal resistance consists of three individual resistances: water-side convection resistance, tube conduction resistance and refrigerant-side convection resistance.

If the total surface area is considered, overall thermal resistance can be written in the form of:

$$\frac{1}{U_{overall}A_{base}}=\frac{1}{h_rA_{base}}+\frac{\ln\left(\frac{D_o-2h_{r,f}}{D_i+2h_{w,f}}\right)}{2\pi k_{tube}L_{tube}}+\frac{1}{h_wA_{base}} \qquad (3\text{-}5)$$

where $U_{overall}$ is the overall heat transfer coefficient, A_{base} is the common base area of the tube, h_r is the refrigerant-side heat transfer coefficient, h_w is the water-side heat transfer coefficient, D_o is the outer tube radius with microchannels, D_i is the inner tube radius without minichannels, $h_{r,f}$ is the height of the outer microchannels, $h_{w,f}$ is the height of the inner minichannels, k_{tube} is the tube thermal conductivity and L_{tube} is the axial length of the tube.

In the next section, correlations are provided to evaluate these heat transfer coefficients. However, wherever applicable, numerical simulation is used to obtain more accurate estimates. The scope of the section is limited to a few important correlations found in the literature and is not a comprehensive survey. It is suggested to refer to original articles to obtain detailed information regarding the experimental findings and method of establishing empirical correlations.

3.4.1 Single-phase heat transfer and pressure drop correlations for flow inside triangular cross sections

This section provides the available correlations in literature for triangular channel flow in single-phase. The correlations are empirical in nature and have been mostly established for macro channels. The most accurate method to evaluate heat transfer coefficient for smaller channels is the numerical simulation method which is discussed in further chapters.

Nusselt number, Reynolds number and Prandtl number for single-phase flow are given by:

$$Nu_w = \frac{h_w D_{h,w}}{k_w}; \quad \mathrm{Re}_w = \frac{\dot{m}_w D_{h,w}}{A_{w,c}\mu_w}; \quad \mathrm{Pr}_w = \frac{\mu_w C_{p,w}}{k_w} \tag{3-6}$$

Campbell and Perkins provided a Nusselt number correlation for developing turbulent flow in an equilateral triangular channel with constant temperature and adiabatic wall boundary condition [51]. The friction factor and Nusselt number are given in terms of average wall temperature T$_w$ and mean bulk fluid temperature T$_m$.

$$f = \frac{0.079}{\mathrm{Re}^{1/4}}\left(\frac{T_w}{T_m}\right)^{-0.4+\left(x/D_h\right)^{-0.67}} \qquad 14.5 < \frac{x}{D_h} < 72 \ ; 1.10 < \frac{T_w}{T_m} < 2.11$$

$$Nu_{x,H1} = 0.021\mathrm{Re}^{0.8}\,\mathrm{Pr}^{0.4}\left(\frac{T_w}{T_m}\right)^{0.7}\phi \tag{3-7}$$

$$\phi = \left[1+\left(\frac{x}{D_h}\right)^{-0.7}\left(\frac{T_w}{T_m}\right)^{0.7}\right] \ 6 < \frac{x}{D_h} < 123 \ ; \ 1.10 < \frac{T_w}{T_m} < 2.11$$

Shah and London provided a fully developed laminar flow correlation for an equilateral triangular channel [52].

$$\begin{aligned} Nu_{H2} &= 1.892; \quad f\,\mathrm{Re} = 13.333 \quad \textit{for no rounded corners} \\ Nu_{H2} &= 2.196; \quad f\,\mathrm{Re} = 14.057 \quad \textit{for one rounded corner} \end{aligned} \tag{3-8}$$

Malak et al. provided a friction factor correlation for fully developed flow turbulent flow in an equilateral triangular channel [53].

$$f = \frac{0.0425}{\mathrm{Re}^{0.2}} \quad \textit{for} \ \ 4000 < \mathrm{Re} < 80000 \tag{3-9}$$

Altemani and Sparrow conducted experiments on an equilateral triangular duct and developed the following correlation [54].

$$Nu = 0.019\ \mathrm{Re}^{0.781} \quad \textit{for} \quad 4000 < \mathrm{Re} < 80000 \tag{3-10}$$

Philips (1987) provided a generalized correlation for evaluating pressure drop for smaller channels, given by: [55]

$$\Delta p_w = \frac{\rho_w u_m^2}{2}\left[\left(\frac{A_c}{A_P}\right)^2 (2K_{90}) + (K_c + K_e) + \frac{4 f_w L}{D_{h,w}} + K(x)\right] \tag{3-11}$$

where A_p is the plenum area; K_{90} is the loss coefficients at 90 degree bends; K_c and K_e are the contraction and expansion coefficients; and K(x) is pressure drop defect. Based on recommendation of Kays & London (1984) and Philips (1990), $K_{90} = 1.2$ and K_c and K_e is derive from their graph [56, 57].

For triangular ducts, K(x) can be replaced with Hagenbagh’s factor $K(\infty) = 1.818$ for no-cornered 60° triangular fins and $K(\infty) = 1.698$ for single-corner 60° triangular fins [52].

3.4.2 Two-phase heat transfer and pressure drop correlations for flow inside microchannels.

As the refrigerant-side involves two-phase flow inside microchannels, a few important correlations are identified that closely represents the microchannel flow for the straight rectangular geometry. Although due to presence of manifolds, changing flow area and entrance region effects, exact flow behavior cannot be captured with these correlations, these correlations provide a fair idea in regard to flow boiling physics inside the finer channels.

The important non-dimensional numbers for two-phase flow are defined as:

$$\mathrm{Re}_{LO} == \frac{GD_{h,r}}{A_{r,c}\mu_{l,r}} \quad \mathrm{Re}\,ynolds\ Number$$

$$Co = \left[\frac{1-x}{x}\right]^{0.8}\left(\frac{\rho_{v,r}}{\rho_{l,r}}\right)^{0.5} \quad Convection\ \ Number$$

$$Bo = \frac{q''}{Gh_{fg}} \quad Boiling\ \ \ Number \tag{3-12}$$

$$\mathrm{Pr}_{l,r} = \frac{\mu_{l,r}C_{pl,r}}{k_{l,r}} \quad \mathrm{Pr}\,andtl\ \ Number$$

$$We_{fo} = \frac{G^2D_{h,r}}{\rho_{l,r}\sigma_r} \quad Weber\ \ \ Number$$

Lazarek and Black performed the saturated flow boiling study for R113 for a hydraulic diameter of 3.15 mm and a mass flux range of 140-740 kg/m^2-s. Heat transfer coefficient was found to be relatively independent of vapor quality but a strong function of Nusselt number, Reynolds number and Boiling number. [58] The following heat transfer correlation was proposed:

$$Nu = 30\,\mathrm{Re}^{0.857}\,Bo^{0.714} \tag{3-13}$$

Tran et al. developed saturated flow boiling correlation using R12 for rectangular channels with hydraulic diameter of 2.4 mm. It was found that nucleate boiling dominated the heat transfer mechanism and heat transfer coefficient was found to be independent for quality > 0.2. No strong mass flux dependence was found. Mass fluxes were in the range of 44-832 kg/m^2-s and heat flux was in the range of 3.6-129 kW/m^2 [59].

$$h = (8.4x10^{-5})(Bo^2We_l)^{0.3}\left(\frac{\rho_l}{\rho_v}\right)^{-0.4} \tag{3-14}$$

Yan and Lin did an experimental investigation of the evaporation of heat transfer and pressure drop for R134a for smaller channel having hydraulic diameter of 2.0 mm. Heat transfer coefficient was found to be inconsistent with vapor quality and influenced by mass flux, heat flux and saturation temperature [60]. Following correlation was proposed:

$$h_{tp} = \left(C_1 C_o{}^{C2} + C_3 Bo^{C4} Fr_{l0}\right)(1 - X_m)^{0.8} h_l \tag{3-15}$$

Bao et al. performed the study of R11 and HCFC123 in a smooth copper tube with a hydraulic diameter of 1.95 mm. Experimental heat transfer coefficients in the range of 1-18 W/m^2-K were found with mass flux range of 50-1800 Kg/m^2-s, heat flux range of 5-200 kW/m^2, vapor quality of 0-0.9 and system pressure range of 200-500 kPa. Nucleate boiling was found to dominate for wide range of flow conditions. Heat transfer coefficient was found to be independent of mass flux and vapor quality but a strong function of heat flux and system pressure [61].

$$h = 2.23 q''^{0.735} \tag{3-16}$$

Yu et al. studied the two-phase pressure drop, boiling heat transfer and critical heat flux in a small horizontal tube having hydraulic diameter of 2.98 mm and 0.91 m heated length. Inlet temperatures from ambient to 80 °C and mass fluxes in the range of 50-200 kg/m^2-s were investigated at the system pressure of 200 kPa. Nucleate boiling dominates over a large mass flux and quality range [62].

$$h = 6{,}400{,}000 (BoWe)^{0.27} \left(\frac{\rho_l}{\rho_v}\right)^{-0.2} \tag{3-17}$$

Kandlikar and Steinke, Kandlikar and Subramaniam developed two-phase flow boiling correlations for microchannels for a wide range of Reynolds number [63, 64].

$$For\,\mathrm{Re}_{LO} > 100, \quad h_{TP} = \max(h_{TP,NBD}, h_{TP,CBD})$$

$$h_{TP,NBD} = 0.6683\,Co^{-0.2}(1-x)^{0.8} h_{LO} + 1058.0\,Bo^{0.7}(1-x)^{0.8} F_{FL} h_{LO}$$

$$h_{TP,CBD} = 1.136\,Co^{-0.9}(1-x)^{0.8} h_{LO} + 667.2\,Bo^{0.7}(1-x)^{0.8} F_{FL} h_{LO}$$

$$10^4 \le \mathrm{Re}_{LO} \le 5x10^6 \qquad h_{LO} = \frac{\mathrm{Re}_{LO}\,\mathrm{Pr}_{l,r}\,(f_r/2)(k_{l,r}/D_{h,r})}{1+12.7(\mathrm{Pr}_{l,r}^{2/3}-1)(f_r/2)^{0.5}}$$

$$3000 \le \mathrm{Re}_{LO} \le 10^4 \qquad h_{LO} = \frac{(\mathrm{Re}_{LO}-1000)\,\mathrm{Pr}_{l,r}\,(f_r/2)(k_{l,r}/D_{h,r})}{1+12.7(\mathrm{Pr}_{l,r}^{2/3}-1)(f_r/2)^{0.5}}$$

$$100 \le \mathrm{Re}_{LO} \le 1600 \qquad h_{LO} = \frac{Nu_{LO}\,k_{l,r}}{D_{h,r}} \quad ; \quad f_r = \left[1.58\ln(\mathrm{Re}_{LO}) - 3.28\right]^{-2}$$

$$\mathrm{Re}_{LO} \le 100 \quad h_{TP} = h_{TP,NBD} = 0.6683\,Co^{-0.2}(1-x)^{0.8} h_{LO} + 1058.0\,Bo^{0.7}(1-x)^{0.8} F_{FL} h_{LO}$$

(3-18)

h_{LO} is the single-phase liquid heat transfer coefficient. F_{FL} is the fluid surface parameter which can be assumed to be 1 in case of unavailability.

Mudawar et al. combined several experimental data for water, R134a and developed following correlation [27, 65]:

$$\mathrm{Re}_{l,r}=\left(\frac{2\overset{\bullet}{m}_w}{N_m}\right)\left(\frac{D_{h,r}}{A_{r,c}\mu_{l,r}}\right)\left(\frac{x_e}{2}\right)\qquad \mathrm{Re}_{v,r}=\left(\frac{2\overset{\bullet}{m}_w}{N_m}\right)\left(\frac{D_{h,r}}{A_{r,c}\mu_{v,r}}\right)\left(1-\frac{x_e}{2}\right)$$

$$\left(\frac{dp}{dz}\right)_l=\frac{2f_lG^2(1-x_e/2)^2}{D_{h,r}\rho_{l,r}}\qquad \left(\frac{dp}{dz}\right)_v=\frac{2f_vG^2(x_e/2)^2}{D_{h,r}\rho_{v,r}}$$

$$f_l=Po/\mathrm{Re}_{l,r}\ ;\ f_v=Po/\mathrm{Re}_{v,r}$$

$$0\le x_e\le 0.05\qquad h_{tp}=3.856X^{0.267}h_{sp,f}\ ;\quad X^2=\frac{\left(\frac{dp}{dz}\right)_l}{\left(\frac{dp}{dz}\right)_v},h_{sp,f}=\frac{Nu_3k_{l,r}}{D_{h,r}}$$

$$X_{vv}=\left(\frac{\mu_l}{\mu_v}\right)^{0.5}\left(\frac{1-x_e}{x_e}\right)^{0.5}\left(\frac{\rho_v}{\rho_l}\right)^{0.5}\qquad X_{vt}=\left(\frac{f_l\,\mathrm{Re}_{v,r}^{0.25}}{0.079}\right)^{0.5}\left(\frac{1-x_e}{x_e}\right)^{0.5}\left(\frac{\rho_v}{\rho_l}\right)^{0.5}$$

$$0.05\le x_e\le 0.55\quad h_{tp}=436.48Bo^{0.522}We_{fo}^{0.351}X^{0.665}h_{sp,f}\ ;\ Bo=\frac{q''}{Gh_{fg}}\ ;\ We_{fo}=\frac{G^2D_{h,r}}{\rho_{l,r}\sigma_r}$$

$$0.55\le x_e\le 1.0\qquad h_{tp}=\max\{(108.6X^{1.665}h_{sp,g}),h_{sp,g}\}$$

$$h_{sp,g}=\frac{Nu_3k_{v,r}}{D_{h,r}}\text{ for laminar gas flow }\ ;\ h_{sp,g}=0.023\,\mathrm{Re}_v^{0.8}\,\mathrm{Pr}_v^{0.4}\text{ for turbulent gas flow}$$

(3-19)

X is the Lockhart-Martinelli parameter. X_{vv} is for laminar liquid and laminar vapor flow. X_{vt} is for laminar liquid and turbulent vapor flow.

Mudawar et al. provided two-phase pressure drop correlation for microchannel where total pressure drop is essentially the sum of all pressure drops due to such as contraction and expansion loss at inlets and exits, friction and acceleration pressure drops for two-phase and pressure drop due to vapor [27, 66].

$$
\begin{gathered}
\Delta p_r = \Delta p_{tot} = \Delta P_c - \Delta P_e + \frac{\sum_{i=1}^{N_M/8} \{(\Delta P_f + \Delta P_a)_{tp} + \Delta P_{sp,g}\}_i}{(N_M/8)} \\
\textit{where} \\
\Delta P_c = \frac{G^2}{2\rho_f}\left[\left(\frac{1}{C_C}-1\right)^2 + \left(1-\frac{1}{\sigma_c^2}\right)\right]\left[1+\frac{(\rho_f-\rho_g)x_{e,in}}{\rho_g}\right] \quad ; \quad \Delta P_e = G^2\sigma_e(1-\sigma_e)\left(\frac{1}{\rho_f}\right)\left[1+\frac{(\rho_f-\rho_g)x_{e,out}}{\rho_g}\right] \\
\Delta P_f = \frac{2G^2L_{tp}}{D_h x_{e,out}} \int_{x_{e,in}}^{x_{e,out}} f_f(1-x_e)\left(\frac{1}{\rho_f}\right)\phi_f^2 dx_e \quad ; \quad \phi_f^2 = 1+\frac{C}{X}+\frac{1}{X^2}, X^2 = \frac{(dp/dz)_f}{(dp/dz)_g} \\
C_{vv} = 2.16\,\mathrm{Re}_{fo}^{0.047} We_{fo}^{0.60} \text{ (Laminar liquid-laminar vapor)} \quad ; \\
C_{vt} = 1.45\,\mathrm{Re}_{fo}^{0.25} We_{fo}^{0.23} \text{(Laminar liquid-turbulent vapor)} \\
\Delta P_a = G^2\left\{\left[\frac{x_{e,out}^2}{\rho_g\alpha_{out}} + \frac{(1-x_{e,out})^2}{\rho_f(1-\alpha_{out})}\right] - \left[\frac{x_{e,out}^2}{\rho_g\alpha_{in}} + \frac{(1-x_{e,in})^2}{\rho_f(1-\alpha_{out})}\right]\right. \quad ; \quad \alpha = \left[1+\left(\frac{1-x_e}{x_e}\right)\left(\frac{\rho_g}{\rho_f}\right)^{2/3}\right]^{-1} \\
\Delta P_{sp,g} = \frac{2L_{sp}}{D_h} f_{sp,g} G^2 \left(\frac{1}{\rho_g}\right) \quad ; \\
f_{sp,g}\,\mathrm{Re}_{sp,g} = 24\left[1-1.3553\beta+1.9467\beta^2-1.7012\beta^3+0.9564\beta^4-0.2537\beta^5\right] \ \mathrm{Re}_g < 2000 \\
f_{sp,g} = 0.079\,\mathrm{Re}_g^{-0.25} \ 2000 < \mathrm{Re}_g < 20{,}000 \ ; \ f_{sp,g} = 0.046\,\mathrm{Re}_g^{-0.2} \ \mathrm{Re}_g > 20{,}000 \ ; \\
\mathrm{Re}_{fo} = \frac{GD_h}{\mu_f} ; \mathrm{Re}_f = \frac{G(1-x_e)D_h}{\mu_f} ; \mathrm{Re}_g = \frac{Gx_eD_h}{\mu_g}, We_{fo} = \frac{G^2D_h}{\sigma\rho_f}
\end{gathered}
\tag{3-20}
$$

3.4.3 Heat transfer correlations for natural convection for outer tube

As the temperature gradient will be low with the use of insulation, not much heat loss is expected, and so the standard heat transfer Churchill Chu correlation for vertical plates can be used:

$$
\begin{gathered}
Ra_L = Gr_L \,\mathrm{Pr}_{air} = \frac{g\beta(T_e - T_{amb})L^3}{\nu_{air}\alpha_{air}} \\
Nu_{OT} = \frac{h_{OT}L}{k_{air}} = 0.68 + \frac{0.67{Ra_L}^{1/4}}{\left[1+\left(0.492/\mathrm{Pr}_{air}\right)^{9/16}\right]^{4/9}} \quad Ra_L \le 10^9
\end{gathered}
\tag{3-21}
$$

This correlation can be used for vertical cylinders if following condition satisfies: [6]

$$
\frac{D_o}{L} \ge \frac{35}{Gr_L^{1/4}}
\tag{3-22}
$$

3.5 Summary

In this chapter, a detailed review of different type of conventional evaporator design with a focus on microchannel-based evaporators was provided. A section was devoted to a special microchannel-based design called manifold microchannel technology, which is the basic design philosophy behind the tubular evaporator, on which the further study is based. In the last section, a few important correlations were reviewed to provide the underlying physics for fluid flow and heat transfer inside microchannels. However, due to the complex geometry and fluid flows, none of these correlations are applicable for the present case. From the literature studies, it is evident that that a more systematic study is needed to establish the effect of important geometrical and fluid flow parameters to predict heat transfer behavior inside a manifold guided channel. Due to the larger number of parameters, it is difficult to find a generalized solution that would be beneficial for all design cases. Hence, the next chapter focuses on a single-phase numerical study of quarter-symmetry manifold microchannel cell using ANSYS IcePAK to validate the findings obtained in the literature studies. An attempt at a parametric optimization which would serve as a guideline for future developments is also given.

CHAPTER 4: SINGLE-PHASE STUDY OF MANIFOLD MICROCHANNEL SYSTEM

This chapter focuses on manifold microchannel design principle and a numerical study of important geometrical and flow parameters which govern the fluid flow and heat transfer behavior. Further, brief attention is given to optimization using the Dynamic-Q method for a fixed mass flow rate inside the manifold microchannel elemental cell. All the studies have been done using ANSYS IcePAK ensuring grid independence of the model.

A manifold microchannel system consists of a microgroove surface attached to a manifold surface on the top perpendicularly aligned with microchannel fins. The function of the manifold is to guide the flow in a particular way to reduce the flow length and pressure drop. A schematic of the manifold microchannel system is shown in Figure 4-1.

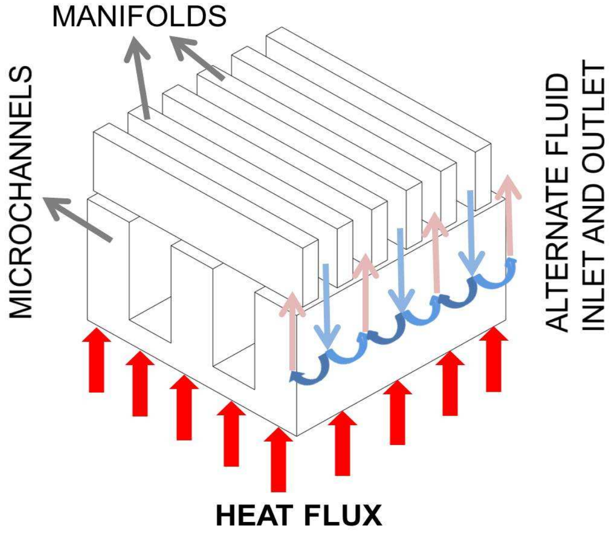

Figure 4-1: Manifold microchannel system schematic

Heat is provided at the base of the microchannels which are typically made of highly conductive materials. Fluid enters alternatively through a series of manifolds attached to the top of the channels. Manifold is usually made of poor conductive materials and is made of light weight material. As multiple feeds are present, flow length at the bottom of the microchannel is reduced, which helps in reducing the pressure drop without sacrificing heat transfer coefficient. As the flow length is much smaller compared to traditional microchannel flow, flow still remains in the developing region and average heat transfer coefficient increases sharply. Multiple flows turns and flow area reduction leads to significant mixing of the flow which further enhances the heat transfer coefficient based on mass flux provided.

Another advantage of the design is that it leads to a reduction of the thermal gradient usually associated with a straight flow, which makes the manifold microchannel system a very promising candidate for removing hot spots and in applications such as chip cooling, where uniform heat flux is critical for smooth functioning of the device.

4.1 Numerical Study

A systematic study was conducted using ANSYS IcePAK to evaluate the critical geometrical and flow parameters that influence the fluid flow and heat transfer behavior. A quarter-symmetry elemental volume cell was chosen for the study that accurately represents the overall system, as shown in Figure 4-2 . The boundary conditions are shown in Figure 4-3.

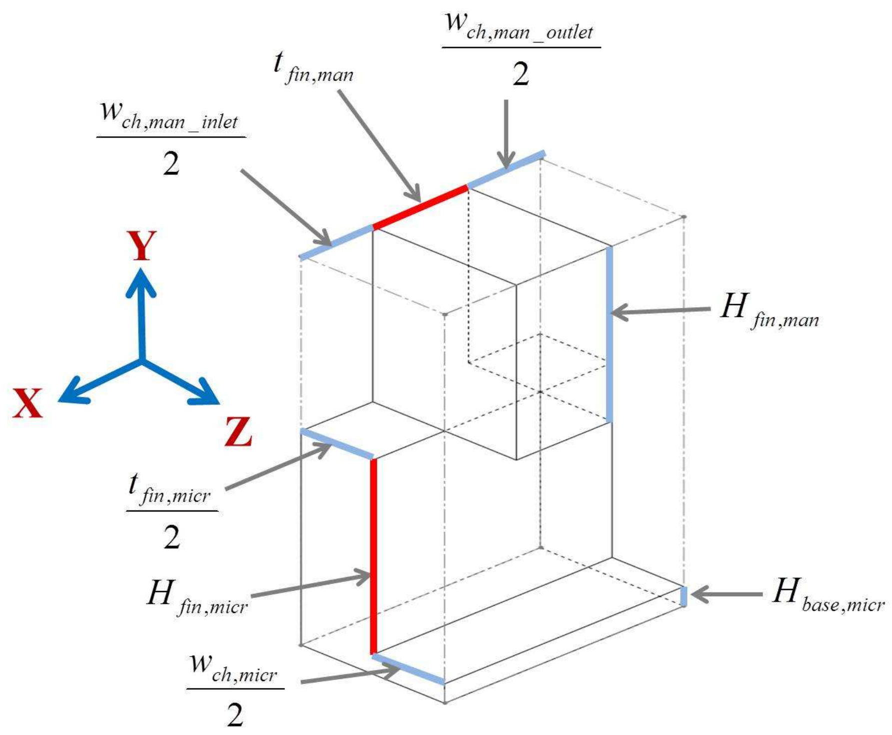

Figure 4-2: Geometrical model used for numerical simulation

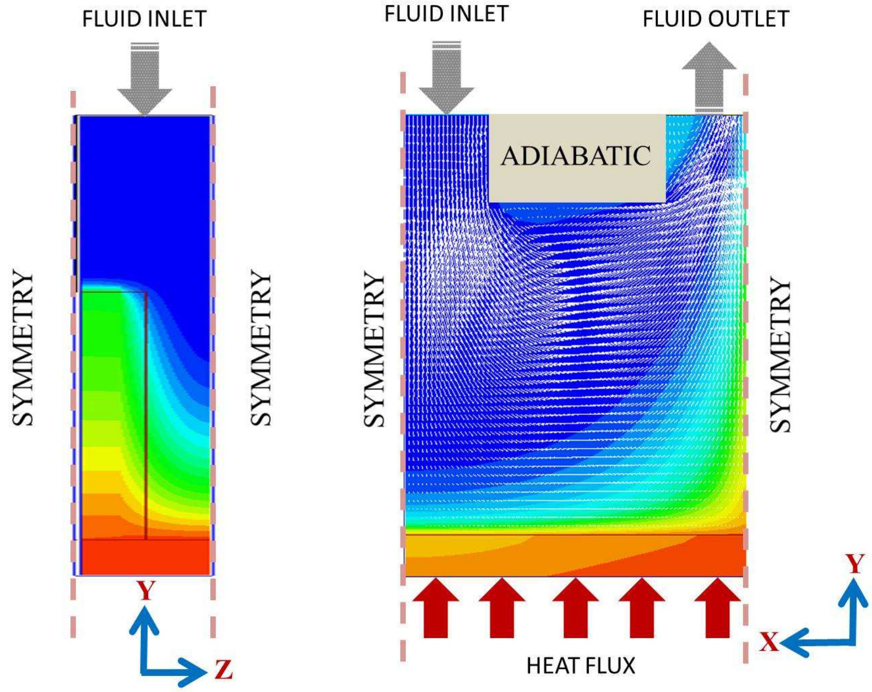

Figure 4-3: Geometrical model with boundary conditions

Numerous geometrical and flow parameters are important for heat transfer characterization as listed below:

- Inlet manifold channel width , w_{ch,man_inlet}
- Outlet manifold channel width , w_{ch,man_outlet}
- Manifold fin width, $t_{fin,man}$
- Microchannel fin thickness, $t_{fin,micr}$
- Microchannel width, $w_{ch,micr}$
- Base height , $H_{base,micr}$
- Microchannel fin height , $H_{fin,micr}$
- Manifold height , $H_{fin,man}$
- Mass flow rate through manifold inlet, $\dot{m}$

The final choice of material for the designed evaporator was a nickel alloy, discussed in a further chapter; hence this was used as the material choice for the microgroove surface in the simulation. The manifold design has been utilized both for single-phase and two-phase flow in the evaporator and only single-phase flow in the solution heat exchanger with ammonia and ammonia-water solutions, respectively. Ammonia-water solution properties can vary significantly with temperature and are heavily influenced by thermodynamic state parameters. However, at lower ammonia mass fraction, properties would be close to water. Hence, for the sake of simplicity, water was chosen as the fluid material for the simulation.

Further, the following assumptions were made for the geometrical model development:

- For single-phase flow with smaller flow length, temperature gradient across the channel would be small and hence density and other properties won't vary significantly. So, all the fluid and surface properties are treated constant with temperature variation.
- Base height is fixed and equal to 0.1 mm to minimize the conduction thermal resistance. No parametric study would be conducted on base height, as uniform heat flux would be considered at the base.
- The manifold volume is made of poor thermal conductivity material (Teflon) and hence would have adiabatic boundary condition on all surfaces. No heat exchange would occur between the manifold surface and fluid present in the channels.
- Symmetry conditions are used at Z-min, Z-max,Y-min & Y-max boundary condition.
    - Z-min is on the middle plane of the microchannel fin thickness.
    - Z-max is on the middle plane of microchannel width.
    - Y-min is on the middle plane of the manifold outlet.
    - Y-max is on the middle plane of the manifold inlet.
- Uniform and constant heat flux of 50,000 W/m^2 is supplied at the base of the computational domain at Y-min. For single-phase flow, heat flux variation was not studied, as it does not significantly affect the heat transfer coefficient or pressure drop in the parameter range studied.
- Uniform mass flow rate is specified at manifold inlet at Y-max.

- Static ambient pressure boundary condition is used at manifold outlet at Y-max. Total pressure drop across the channel is evaluated keeping outlet feed as the reference.
- All fluid properties are assumed to be constant for water at 25 °C and used from ANSYS IcePAK 13.0.2 default database :
    - Density = 998.0 kg/m^3;
    - Specific heat = 4183.0 J/Kg-K
    - Conductivity = 0.582 W/m-K
    - Viscosity = 0.001 kg/m-s
    - Molecular weight = 18.015 kg/kmol
- The microgroove material is nickel (Ni-Pure) and the following properties are used from ANSYS IcePAK 13.0.2 default database:
    - Density = 8907.0 kg/m^3
    - Specific heat curve (K, J/Kg-K ; T=0, Cp = 163 ; T = 77, Cp=163; T = 373, Cp=465; T = 1000, Cp = 465)
    - Conductivity type = Isotropic
    - Thermal Conductivity = 91.74 W/m-K

The total size of the computational domain was determined based on the above geometrical parameters and is summarized below.

$$\begin{aligned}
\Delta X &= \frac{w_{ch,man\_inlet}}{2} + t_{fin,man} + \frac{w_{ch,man\_outlet}}{2} && Comp\ domain\ X - size \\
\Delta Y &= H_{base,micr} + H_{fin,micr} + H_{fin,man} && Comp\ domain\ Y - size \\
\Delta Z &= \frac{t_{fin,micr}}{2} + \frac{w_{ch,micr}}{2} && Comp\ domain\ Z - size
\end{aligned} \tag{4-1}$$

A new set of dimensionless based parameters are also defined, which is independent of geometrical parameters:

$$\begin{aligned}
Micr\_FC\_Ratio &= \frac{t_{fin,micr}}{w_{ch,micr}} && Microchannel\ \ fin/channel\ Ratio \\
Micr\_Aspect\_Ratio &= \frac{H_{fin,micr}}{w_{ch,micr}} && Microchannel\ \ c/s\ \ Aspect\ Ratio \\
Man\_FC\_Ratio &= \frac{t_{fin,man}}{w_{ch,man\_inlet}} && Manifold\ \ fin/channel\ Ratio
\end{aligned} \tag{4-2}$$

Considering the manufacturing limits of the fins and velocity attained in the microchannel region, the following ranges for geometrical and flow parameters were considered.

$$\begin{aligned}
&q'' = 50{,}000\ \ W/m^2; \quad 0.5e-6\ kg/s \le \dot{m} \le 15e-6\,kg/s; \\
&H_{base,micr} = 0.1\ \ mm\ ; \\
&0.5 \le Micr\_FC\_Ratio \le 1.5; && 1 \le Micr\_Aspect\_Ratio \le 20 \\
&0.1\ mm < w_{ch,micr} < 1\ mm; && 0.1\ mm < w_{ch,man\_inlet} < 5\ mm \\
&0.1mm < H_{fin,man} < 5\,mm; && 0.1 < Man\_FC\_Ratio < 5
\end{aligned} \tag{4-3}$$

Two output functions, heat transfer coefficient and pumping power were considered for evaluating the fluid flow and heat transfer behavior.

The effective heat transfer coefficient is evaluated using mean area averaged surface temperature at the base (T_{base}) and the mean area averaged fluid inlet temperature (T_{in}).

$$h = \frac{q''}{(\bar{T}_{base} - \bar{T}_{in})} \tag{4-4}$$

Pumping power flux is calculated for the base area using area averaged pressure at inlet and outlet.

$$P''_{pump} = \frac{\dot{m}\left(\bar{P}_i - \bar{P}_o\right)}{\rho\left[L_{base}\left(\frac{t_{fin,micr}}{2} + \frac{w_{ch,micr}}{2}\right)\right]} \tag{4-5}$$

The Reynolds number in the microchannel flow section is a critical parameter that influences the fluid flow and heat transfer behavior for the overall manifold system.

$$\begin{aligned} \mathrm{Re}_{micr} &= \frac{G_{micr} D_h}{\mu} \\ G_{micr} &= \rho V_{micr} \\ D_h &= \frac{2H_{fin,micr} w_{ch,micr}}{(H_{fin,micr} + w_{ch,micr})} \end{aligned} \tag{4-6}$$

'G_{micr}' is the mass flux in the microchannel cross section which in turn provides the average velocity in the cross section. 'D_h' is the hydraulic diameter of the microchannel flow area. 'ν' and 'ρ' are the dynamic viscosity and density of the working fluid, respectively.

The ANSYS IcePAK settings for solving the baseline case are shown in Table 4-1.

Table 4-1: ANSYS IcePAK solver settings

Parameter	**Status/value**
Variables Solved	Flow, Temperature
Flow regime	Laminar (very small flow rate)
Gravity	Off
Time Variation	Steady
Number of iterations	500
Flow convergence criteria	1e-4
Temperature convergence criteria	1e-7

A first order unwind scheme was used for temperature and momentum equations. The under relaxation factor for pressure was kept at a default value of 0.3 and 0.7 for momentum. The exact settings for the discretization scheme, under-relaxation and linear solver are shown in Figure 4-4. Basic Navier-Stokes equations were being solved for transport of mass, momentum and energy for calculating laminar flow with heat transfer.

Conservation of mass and continuity equation is given by:

$$\frac{\partial \rho}{\partial t} + \nabla.(\rho \vec{v}) = 0 \tag{4-7}$$

For constant fluid properties or incompressible fluid, the continuity equation reduces to:

$$\nabla.(\vec{v}) = 0 \tag{4-8}$$

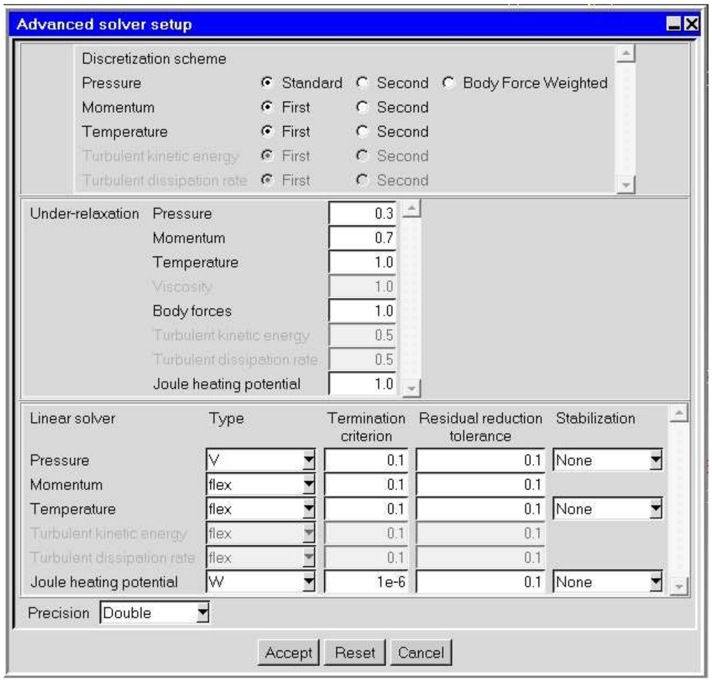

Discretization scheme
Pressure ● Standard ○ Second ○ Body Force Weighted
Momentum ● First ○ Second
Temperature ● First ○ Second
Turbulent kinetic energy ● First ○ Second
Turbulent dissipation rate ● First ○ Second

Under-relaxation		
	Pressure	0.3
	Momentum	0.7
	Temperature	1.0
	Viscosity	1.0
	Body forces	1.0
	Turbulent kinetic energy	0.5
	Turbulent dissipation rate	0.5
	Joule heating potential	1.0

Linear solver	Type	Termination criterion	Residual reduction tolerance	Stabilization
Pressure	V	0.1	0.1	None
Momentum	flex	0.1	0.1	
Temperature	flex	0.1	0.1	None
Turbulent kinetic energy	flex	0.1	0.1	
Turbulent dissipation rate	flex	0.1	0.1	
Joule heating potential	W	1e-6	0.1	None

Precision: Double

Figure 4-4: Discretization scheme & solver precision

The momentum transport for an inertial/non-accelerating reference frame is described by:

$$\begin{aligned} \nabla\cdot\left(\rho\vec{v}\,\vec{v}\right) &= -\nabla p + \nabla\cdot\left(\overline{\overline{\tau}}\right) + \rho\vec{g} + \vec{F} \\ \overline{\overline{\tau}} &= \mu\left[\left(\nabla\vec{v} + \nabla\vec{v}^{T}\right) - \frac{2}{3}\nabla\cdot\vec{v}\,I\right] \end{aligned} \tag{4-9}$$

where p is the static pressure, $\overline{\overline{\tau}}$ is the stress tensor and $\rho\vec{g}$ is the gravitational body force. $\vec{F}$ is the source term that may arise from resistances, sources, etc. μ is the dynamic viscosity and I is the unit tensor. As gravity and body forces are absent for the current problem; these would not be considered for solving the equation.

The energy equation for fluid region can be defined in terms of sensible enthalpy as:

$$\nabla \cdot \left(\rho h \vec{v} \right) = \nabla \cdot \left[(k) \nabla T \right]$$
$$h = \int_{T_{ref}}^{T} c_p dT; \; T_{ref} = 298.15 \; K; \tag{4-10}$$

where k is the molecular conductivity. For the current laminar problem, the above equation further reduces to:

$$\nabla \cdot (\rho h \vec{v}) = \nabla \cdot (k \nabla T) \tag{4-11}$$

4.1.1 Grid Independence Study

A grid independence test was conducted to find the optimum size required to carry on the parametric studies to save computation time without sacrificing accuracy. A study was conducted for low and higher mean velocity inside the microchannel which is the critical indicator of the fluid flow behavior and stability of the grid. Fifteen different grid sizes were selected from very coarse to very fine grids for low Reynolds numbers. Five different grid sizes were studied for medium to fine grid sizes for higher Reynolds number. It can be seen in Figure 4-5 that a smooth predictable trend was obtained for both base heat transfer coefficient and pumping power for all the cases. Near the grid point with 160893 nodes (Δx = 20 μm, Δy = 8 μm, Δz = 4 μm), it can be observed that the graph flattens out and the change of output functions is within 0.5%; hence, this was chosen as the optimum point. For higher Reynolds numbers (Re ~ 110) also, variation was within the same range, and the same optimum point was used. All further simulations were carried using this grid size and number of nodes.

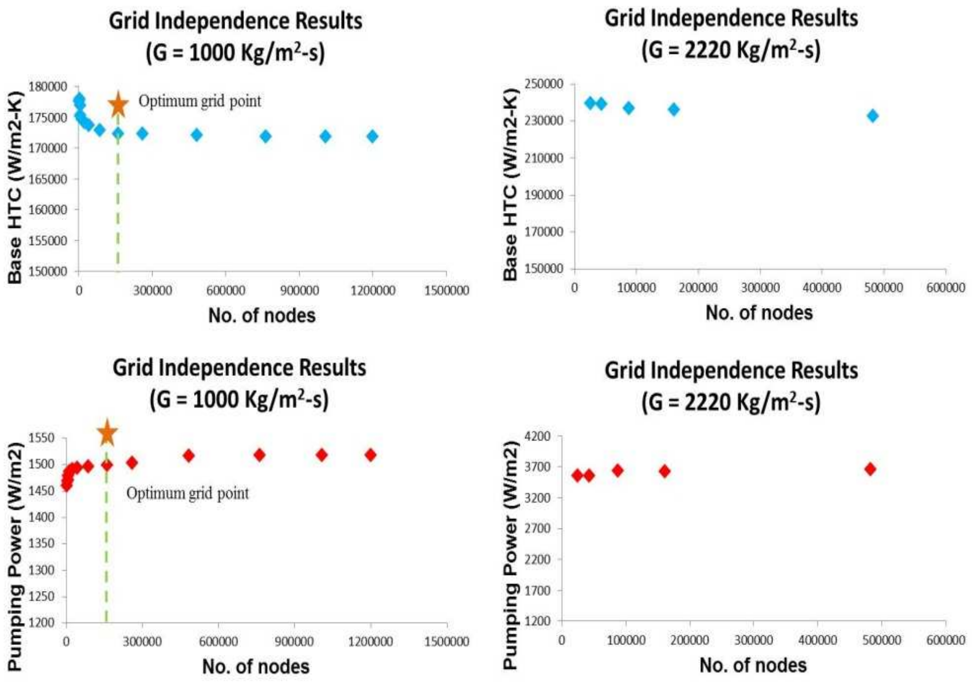

Figure 4-5: Grid independence results for low (Re = 50) and high mean microchannel velocity (Re = 110)

4.1.2 Baseline Case

A baseline case was run using the following design parameters using the nickel surface and water as the working fluid.

$$t_{fin,micr} = w_{ch,micr} = 0.3\ mm$$

$$H_{base,micr} = 0.1mm;\quad H_{fin,micr} = 0.3mm;\quad H_{fin,man} = 1mm$$

$$w_{ch,man\_inlet} = w_{ch,man\_outlet} = 1\ mm;\quad t_{fin,man} = 1\ mm$$

$$\dot{m} = 4.5x10^{-6}\ kg/s;\quad q'' = 50{,}000\ W/m^2$$

$$Micr\_FC\_Ratio = 1;\quad Micr\_Aspect\_ratio = 10; \tag{4-12}$$

$$Man\_FC\_Ratio = 1$$

For mesh control, hexa-cartesian mesh parameters were used with maximum X-size of 20 µm, maximum Y-size of 8 µm and maximum Z-size of 4 µm. The minimum gap in all directions was 1 µm. The total number of elements for the computational domain was 140800 with the total number of nodes being 160893. The quality of the mesh is 1 in a range of 0 to 1. The volume range for the elements is 5.7892e-16 < V < 6.0e-16 µm^3 and the skewness for the element is 0. The temperature contour plot for Z-max plane is shown below in Figure 4-6.

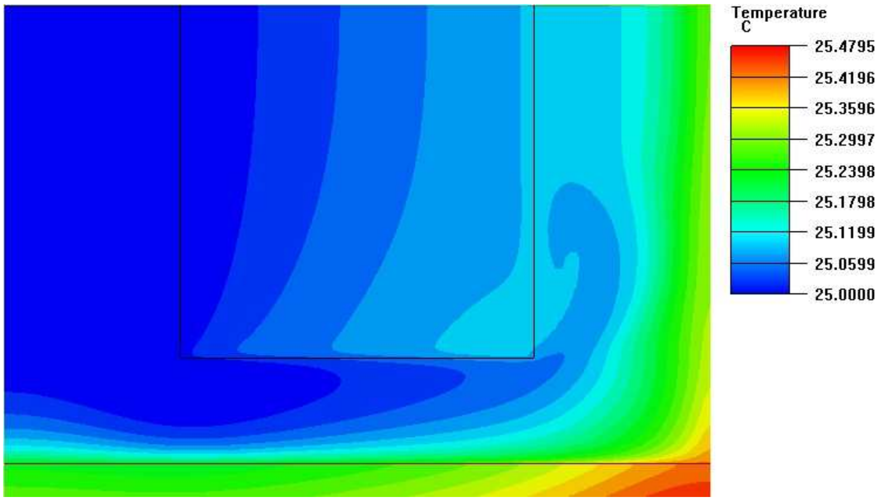

Figure 4-6: Mean temperature contour plot in Z-max plane for baseline case

It can be seen that as the base is supplied with constant heat flux, the inlet fluid gains heat and temperature distribution is non-uniform on the outlet. The initial calculated Reynolds number for the problem is 17.964 and Peclet number is 129.112. Much of the heat exchange is happening in the thin layer near the base surface and it divides the outlet fluid in two zones: the inner zone which doesn't participate in heat exchange as it is bypassed from the top layer of the microchannel and the outer zone which contributes to maximum energy transport. Further velocity distribution for the Z-max symmetry face is shown in Figure 4-7.

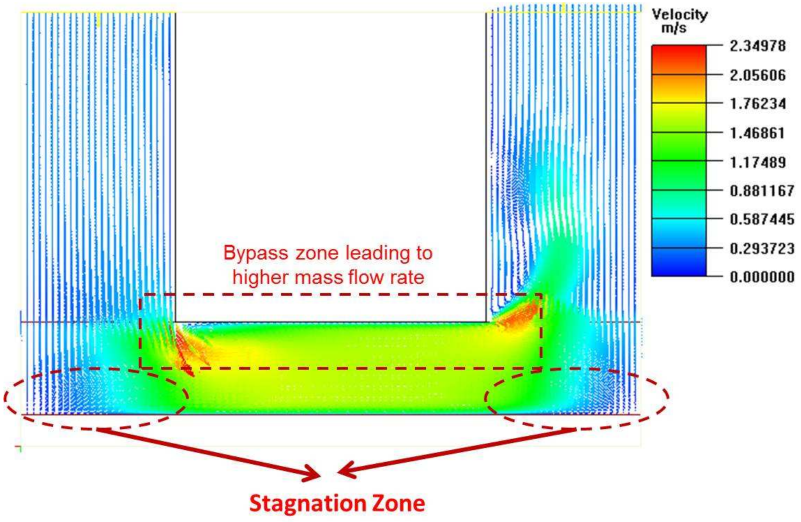

Figure 4-7: Mean velocity vector plot in Z-max plane for baseline case

Due to the creation of a stagnation zone at the bottom of the microchannel, which is also found in the literature, it can be observed that mass flow rate is higher at the top corner part of the microchannel, which effectively creates a bypass zone. A study has been conducted further in the sections to know how velocity plot is affected with increase in Reynolds number. It is also important to study static pressure distribution plot, as this would provide relative pressure distribution in the manifold and the microchannel.

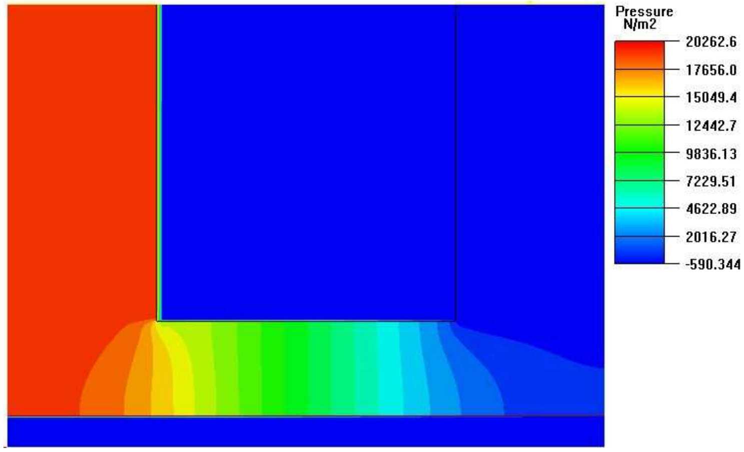

Figure 4-8: Static pressure distribution at Z-max plane for baseline case

It can be seen from the Figure 4-8 that majority of the pressure drop happens across the microchannel length and the manifold inlet/outlet section has almost uniform pressure distribution. The static pressure increases from the top part to the bottom part of the microchannel which is opposite from the velocity distribution curve and aligns with Bernoulli’s principle. Table 4-2 summarizes the output parameter of interest for the simulation.

Table 4-2: Baseline case results summary

Parameter	Value
Mean base temperature	25.2899 °C
Fluid Inlet Temperature	25.0 °C
Base Heat Flux	50,000 W/m^2
Base Heat Transfer Coefficient	172473 W/m^2-K

Mean pressure inlet	20205.4 Pa
Mean pressure outlet	0 Pa
ΔP (Total pressure drop)	20205.4 Pa
Mass flow rate,	4.5e-6 Kg/s
Microchannel mass flux	1000 Kg/m^2-s
Microchannel mean velocity	1 m/s
Reynolds number	1000
Pumping power flux	1,500 W/m^2

Convergence was monitored in terms of velocities, continuity and energy residuals as shown in Figure 4-9. The flow and energy equations are solved sequentially to save further computation time as no property variation is expected due to low thermal gradient.

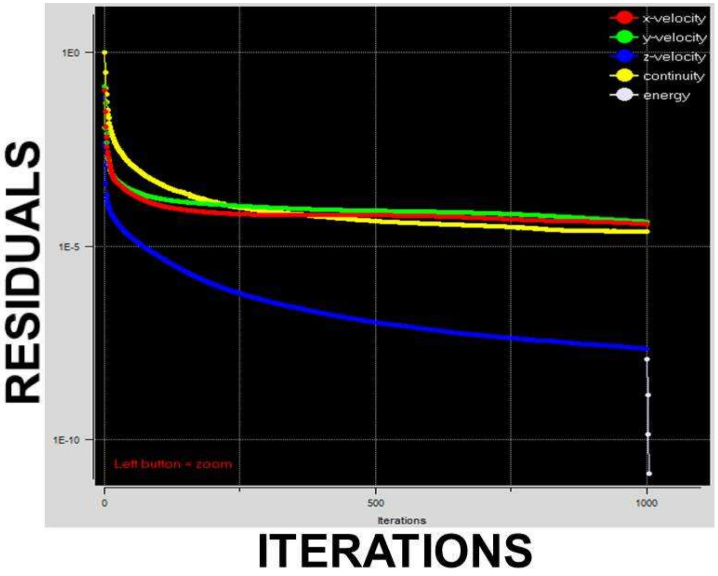

Figure 4-9: Residual plot for baseline case

4.1.3 Parametric Studies

This section of the chapter discusses the effect of important geometrical parameters for the manufacturing ranges described earlier in order to better understand the fluid flow and heat transfer behavior. Parameters were also varied and checked for various mass flux values too for both base heat transfer coefficient and mass flux.

4.1.3.1 Influence of fin width

Microchannel fin width significantly affects the base heat transfer coefficient as it tends to change the base heat transfer area. For a fixed channel width and mass flux, the area available for convection is constant but with increasing fin width provides more conduction thermal path. As the conduction thermal resistance is higher compared to microchannel convection resistance, the overall base temperature increases for increasing fin width, leading to lower average base heat transfer coefficient. However, the curve goes through a peak for much thinner fin dimensions due to fin efficiency limitations.

For a constant mass flow rate and constant channel width, the pumping power flux decreases across the channel with increasing fin width. This is due to decrease in manifold pressure drop with increasing fin width. This clearly suggests manifold pressure drop also needs to be taken into account for much thinner fin width.

A study has been conducted for a smaller (< 50 µm) and medium size (50-200 µm) microchannel hydraulic diameter for increasing mass flow rate and fin width, and the output is monitored in terms of base heat transfer coefficient and pumping power.

It can be seen in Figure 4-10 and Figure 4-12 that the heat transfer coefficient curve goes through a peak which aligns with analytical models for finned heat sinks. The peak is more pronounced for higher mass flow rate and increasing channel width. It would be desirable to keep the fin width corresponding to peak value to have a higher base heat transfer coefficient. The pumping power curves as shown in Figure 4-11 and Figure 4-13 drop down with increasing fin width and increasing mass fluxes as it is expected that the majority of the pressure drop happens inside the microchannel. However, at lower mass fluxes, it can be seen that curve drops with a noticeable gradient, which suggest that a good percentage of pressure drop happens inside the manifold itself.

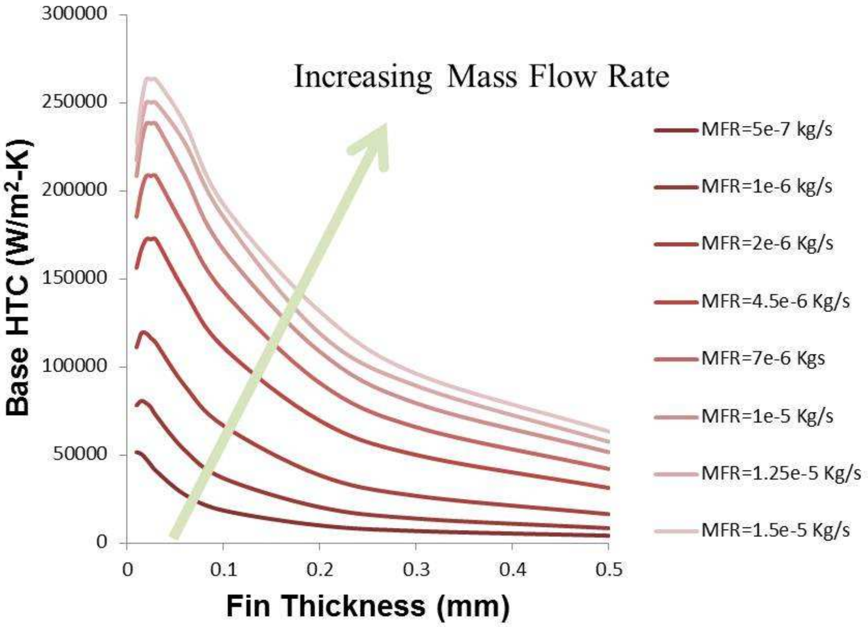

Figure 4-10: Base heat transfer coefficient variation with varying mass flux and microchannel fin thickness for channel width of 30 µm

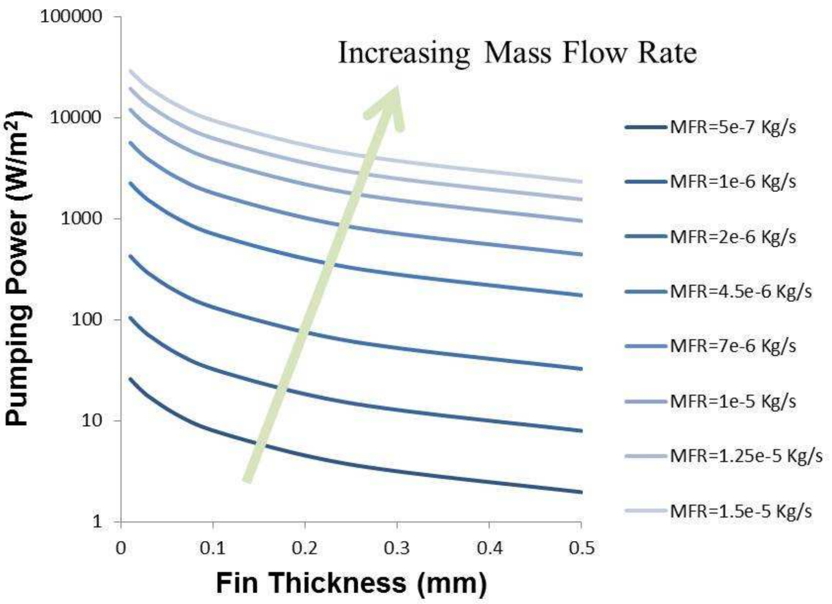

Figure 4-11: Pumping power variation with varying mass flux and microchannel fin thickness for channel width of 30 µm

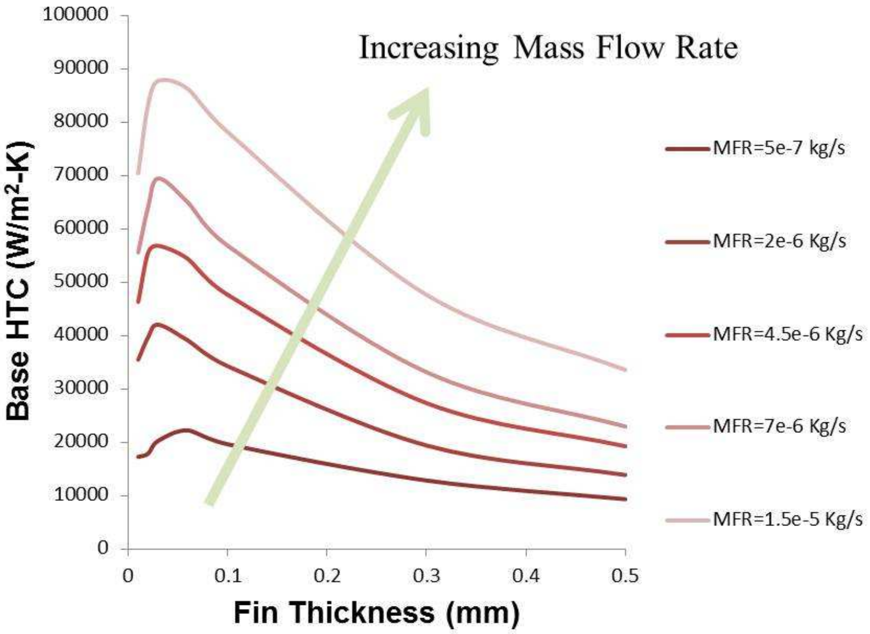

Figure 4-12: Base heat transfer coefficient variation with varying mass flux and microchannel fin thickness for channel width of 100 µm

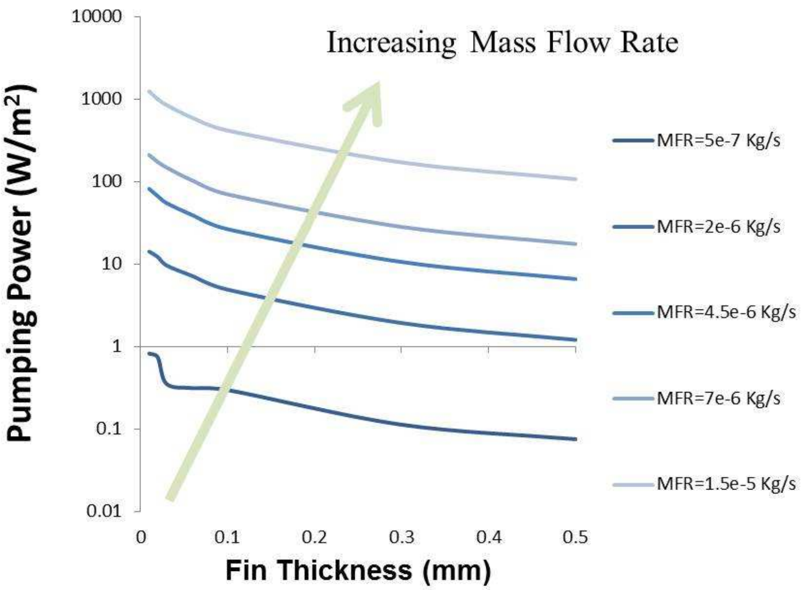

Figure 4-13: Pumping power variation with varying mass flux and microchannel fin thickness for channel width of 100 µm

4.1.3.2 Influence of microchannel width

Microchannel width is a critical parameter affecting the fluid dynamics and thermal transport behavior significantly. Change in width directly changes the Reynolds number which ultimately affects the Nusselt number. For a constant microchannel width, base heat transfer coefficient increases with increasing mass flow rate. The variation of heat transfer coefficient follows a power law and hence, low values were obtained for hydraulic diameter more than 0.1 mm for the mass fluxes studied as shown in Figure 4-14. Pumping power varies by an order of magnitude with hydraulic diameters as shown in Figure 4-15. For a constant microchannel width, pressure drop increases significantly with increasing mass flow rate. Hence the Y-axis of the plot is shown in logarithmic scale. For laminar flow with smaller Reynolds numbers (Re <100), pressure drop varies inversely with the fifth power of hydraulic diameter. The same set of results can be inverted for changing aspect ratio. As aspect ratio increases, heat transfer coefficient decreases and pressure drop increases for constant mass flux, constant fin height, and increasing channel width.

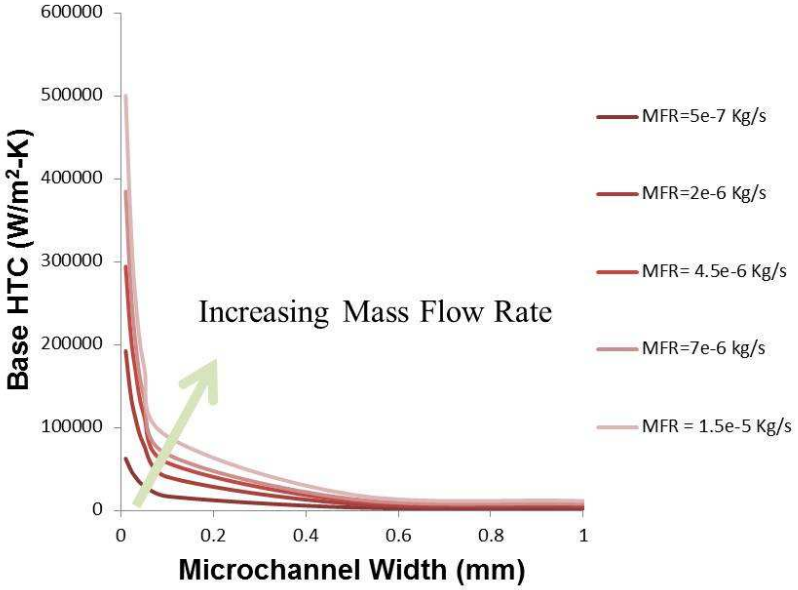

Figure 4-14: Base heat transfer coefficient variation with varying mass flow rate and microchannel width

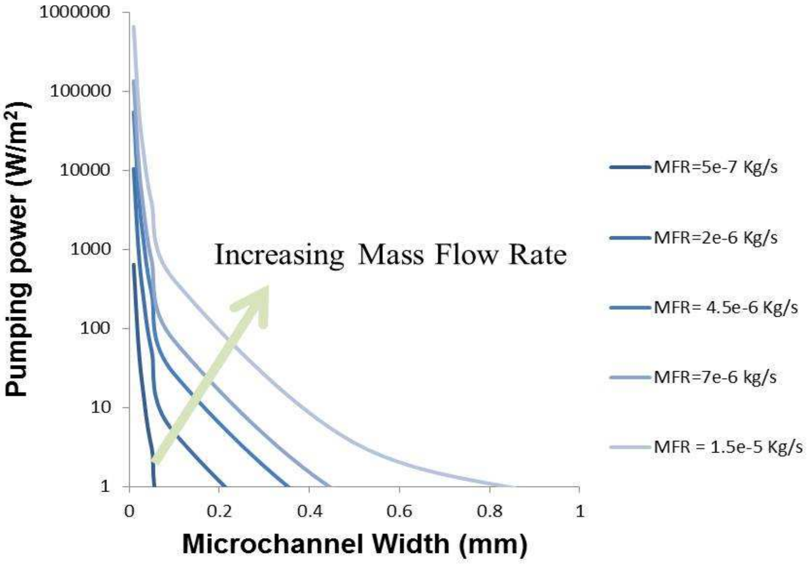

Figure 4-15: Pumping Power variation with varying mass flow rate and microchannel width

For constant microchannel width and increasing mass flux, an additional comparison is provided for velocity distribution inside the microchannels. As the mass flux increases, more fluid with higher velocity is pushed towards the bottom of the microchannel, generating more friction which leads to higher pressure drop than traditional microchannel design as shown in Figure 4-16. At lower fluxes, fluid bypasses through the top part of the microchannel, creating a stagnation zone at the bottom of the microchannel. Heat transfer coefficient would be lowered because of additional thermal resistance provided by the stagnated fluid zone.

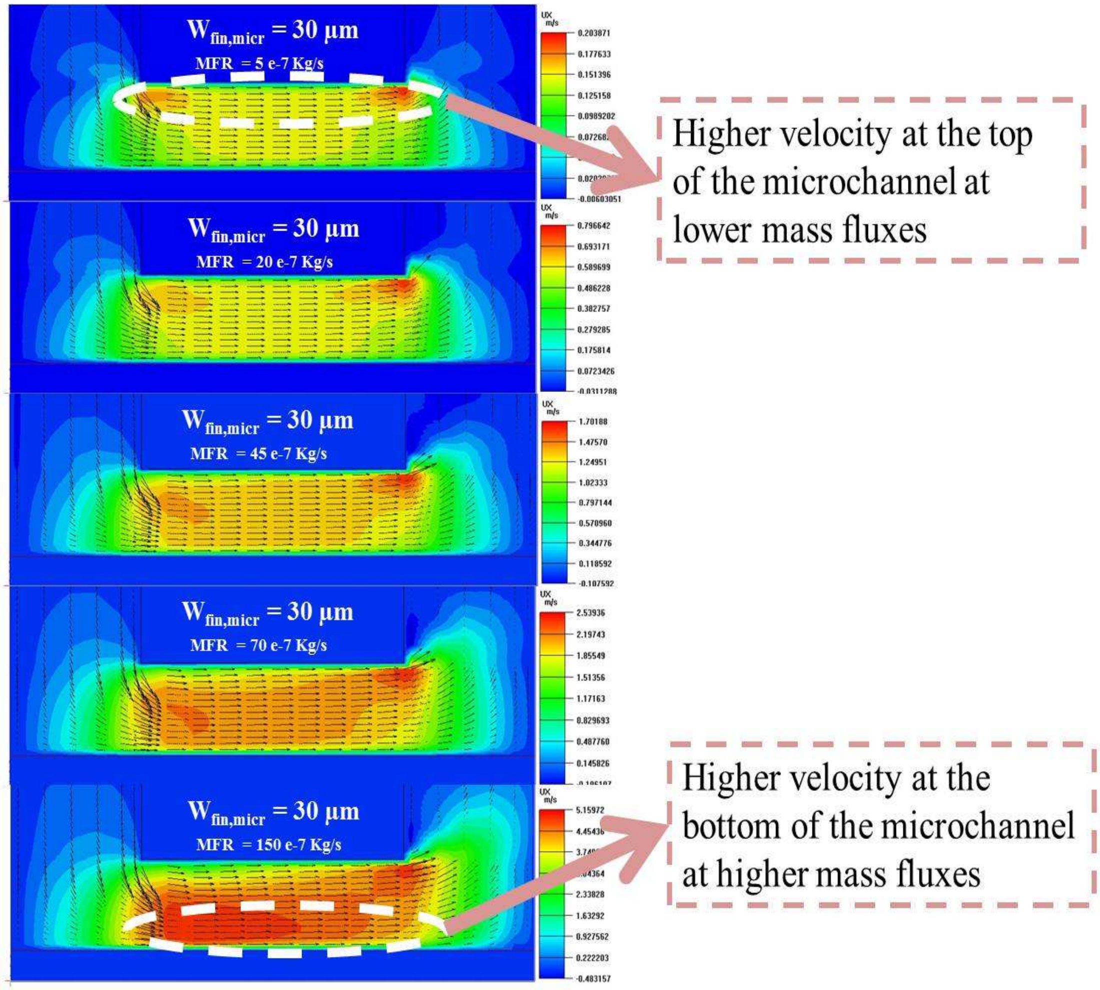

Higher velocity at the top of the microchannel at lower mass fluxes

Higher velocity at the bottom of the microchannel at higher mass fluxes

Figure 4-16: Changing velocity distribution with changing mass flux inside a manifold microchannel

4.1.3.3 Influence of microchannel fin height

Microchannel fin height is another important parameter, as it alters the aspect ratio and also affects the mass flux. With increasing fin height, a peak is obtained for base heat transfer coefficient, which suggests there is an optimum in between. With increasing mass flux, the peak is more pronounced as shown in Figure 4-17. At smaller fin height dimensions, overall heat transfer coefficient is low, as there is less area available for heat transfer enhancement. At larger fin height dimensions, mean velocity becomes smaller, which reduces the Reynolds number. Further, due to theoretical fin efficiency limitations, heat transfer coefficient goes down.

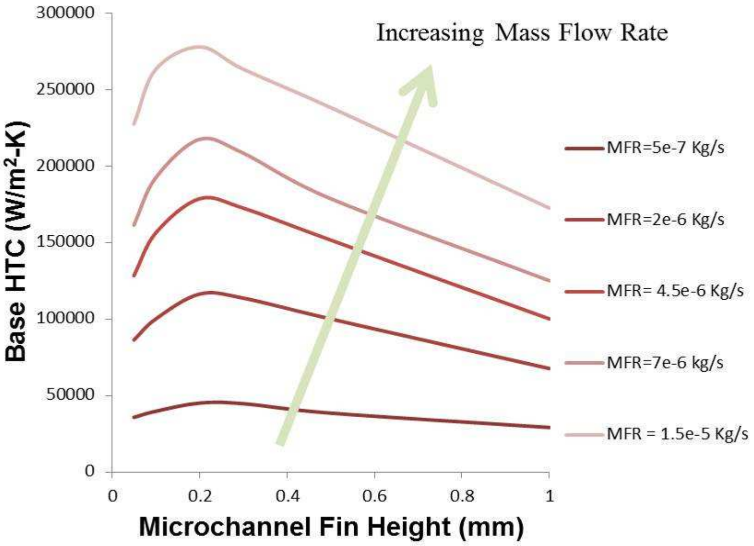

Figure 4-17: Base heat transfer coefficient variation with varying mass flow rate and microchannel fin height

Pumping power flux decreases with increasing fin height for constant mass flow rate. With increasing fin height, microchannel mass flux decreases and the hydraulic diameter increases. Both factors contribute to an order of magnitude decrease in the pressure drop as shown in Figure 4-18.

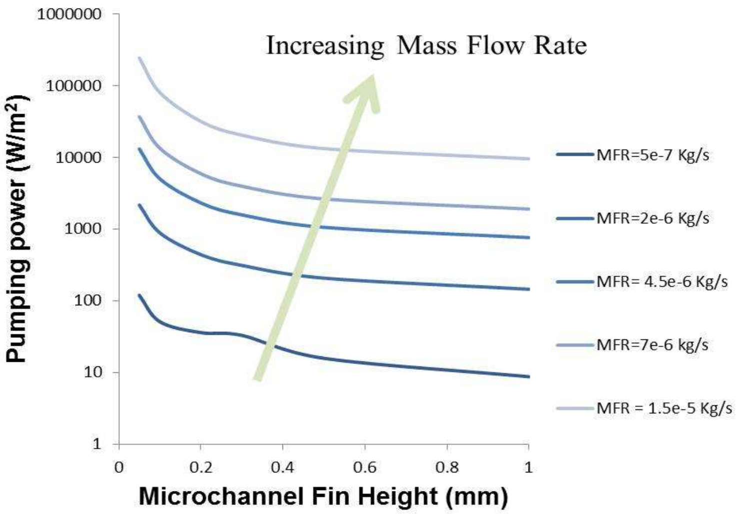

Figure 4-18: Pumping power variation with varying mass flow rate and microchannel fin height

4.1.3.4 Influence of manifold fin height

Manifold height does not appear to have considerable effect on heat transfer coefficient and pumping power flux in the parameter range studied as shown in Figure 4-19 and Figure 4-20. No change in heat transfer coefficient with change in manifold height suggests a less significant change in flow behavior at the entry region of the microchannel. The pumping power flux data have some variation within 0.1%, which can be attributed to the change in flow length of the manifold. With increasing mass flow rate, both the graphs follow predicted behavior in terms of increasing heat transfer coefficient and pumping power flux.

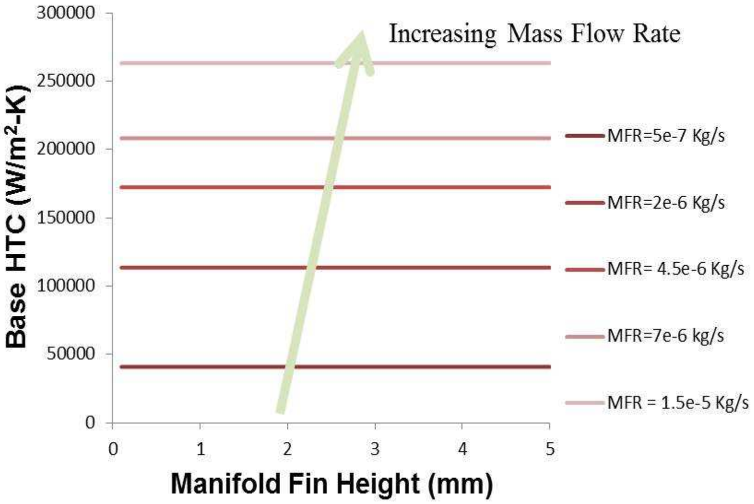

Figure 4-19: Base heat transfer coefficient variation with varying mass flow rate and manifold fin height

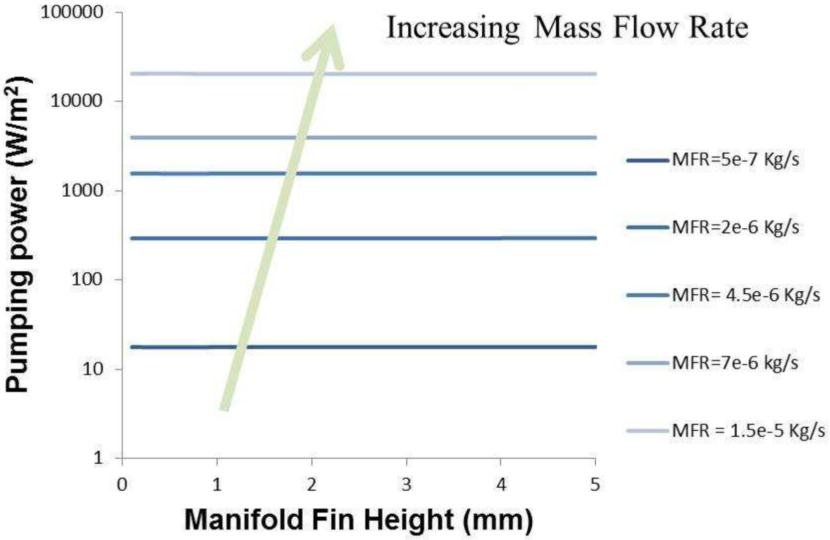

Figure 4-20: Pumping power variation with varying mass flow rate and manifold fin height

4.1.3.5 *Influence of manifold fin thickness*

Manifold fin thickness alters the flow length and affects both fluid flow and heat transfer behavior considerably, as shown in Figure 4-21 and Figure 4-22. As the flow length increases, pressure drop increases proportionately. But pumping power flux remains linear, as it is flow length independent. For lower mass fluxes, an increasing trend can be seen due to pressure drop distribution between manifold and microchannel. Heat transfer coefficient drops significantly with increasing flow length because of the transition from developing to developed flow. Due to an increase in bulk fluid temperature and a thicker boundary layer, the heat transfer coefficient decreases and the average base temperature shoots up.

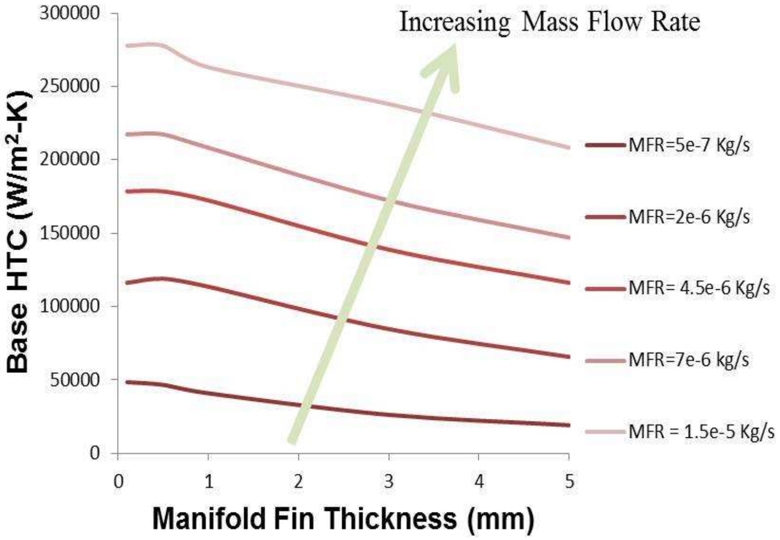

Figure 4-21: Base heat transfer coefficient variation with varying mass flow rate and manifold fin thickness

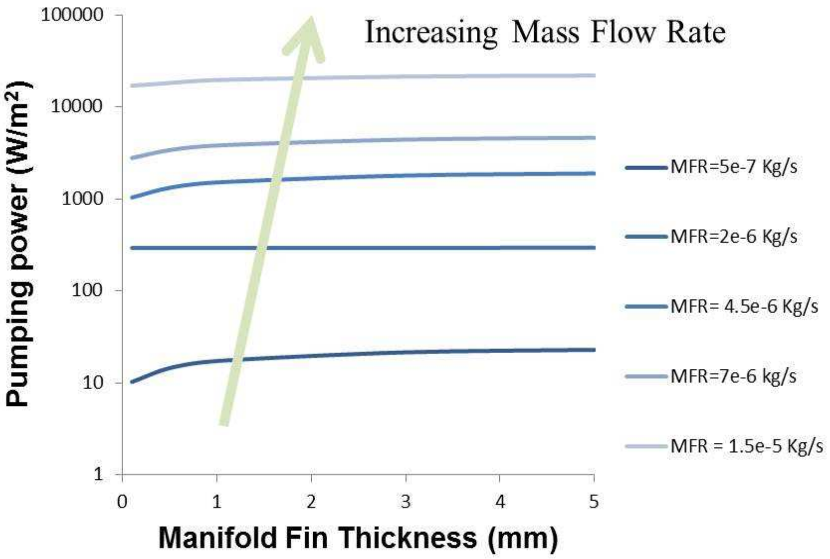

Figure 4-22: Pumping power variation with varying mass flow rate and manifold fin thickness

A comparison is provided for different manifold length where temperature variation across the base is significant, as shown in Figure 4-23. For smaller manifold length, the flow never develops and the heat transfer coefficient is lower, which results in lower average base temperature. For larger manifold fin thickness, flow tends to stratify and heat transfer coefficient decreases across the length, which results in higher average base temperature.

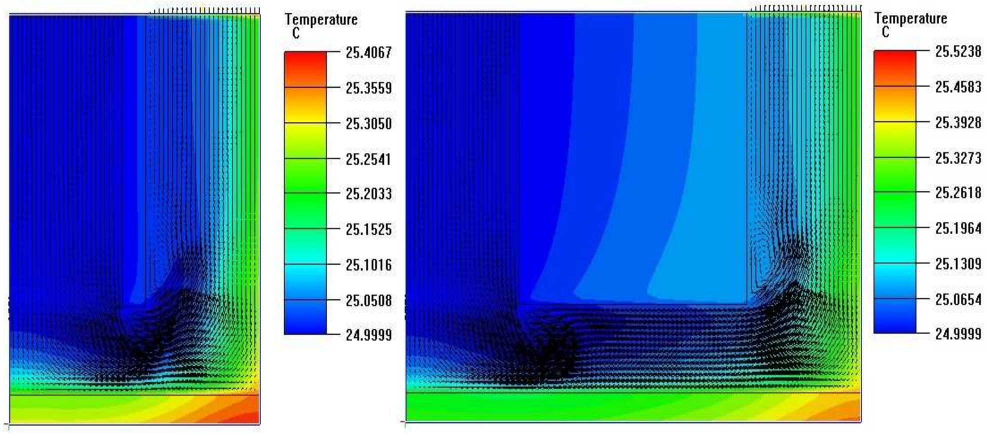

Figure 4-23: Temperature contour for manifold fin thickness of 0.1 mm (left) and 1 mm (right)

4.1.3.6 Influence of inlet manifold length

Inlet manifold length has a significant effect on heat transfer coefficient, as longer inlet length has more base area for delivery of the fluid to the microchannel and hence decreases the overall heat transfer coefficient. Pumping power exhibits an opposite trend compared to manifold fin thickness. At much smaller inlet lengths, pressure drop in the inlet manifold itself is much higher, which gets eased off with an increase in the inlet width. The numerical simulation results are provided in Figure 4-24 and Figure 4-25.

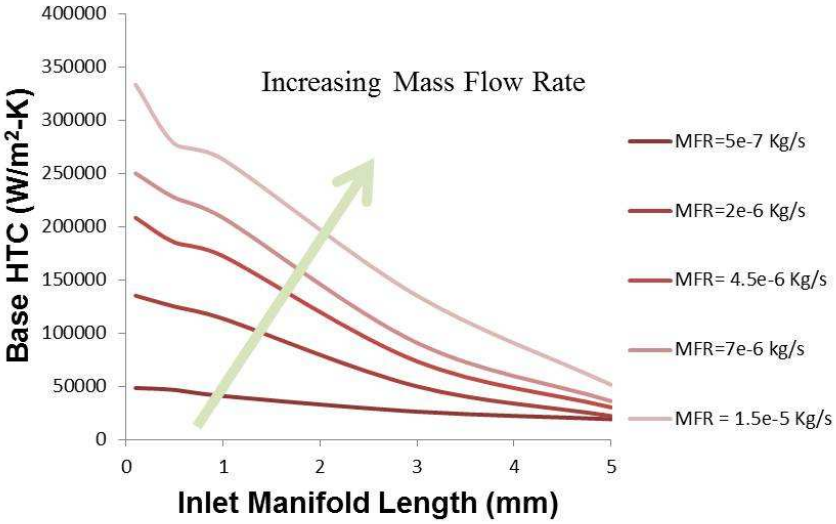

Figure 4-24: Base heat transfer coefficient variation with varying mass flow rate and manifold inlet length

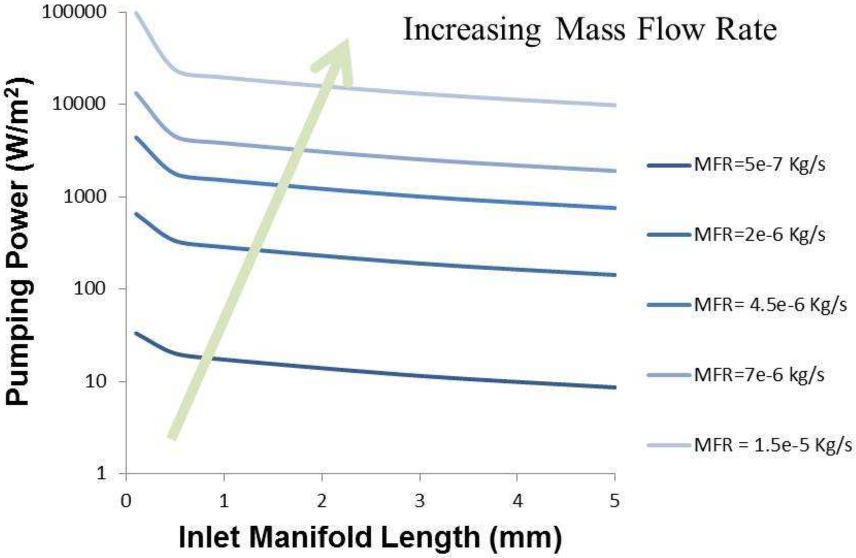

Figure 4-25: Pumping power variation with varying mass flow rate and manifold inlet length

4.1.3.7 *Influence of outlet manifold length*

Outlet manifold length has very similar effect close to effects of inlet manifold length as shown in Figure 4-26 and Figure 4-27. However, at smaller manifold outlet lengths, heat transfer coefficient asymptotes to a lower value. This is because a smaller outlet leads to higher exit velocity, which does not provide any benefit of increase in heat transfer rate as opposed to an increase in inlet velocity in the previous case. The pumping power curve is very similar to the earlier case as the sum of the individual pressure drop is same.

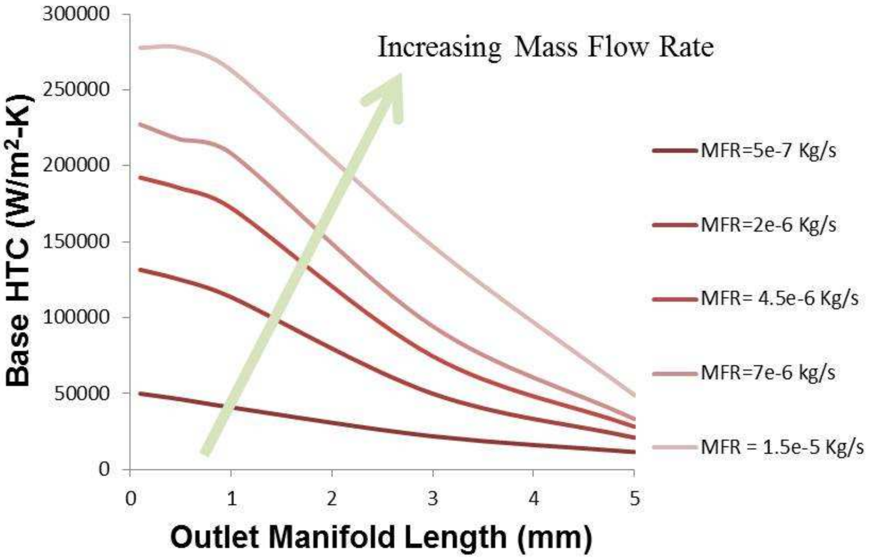

Figure 4-26: Base heat transfer coefficient variation with varying mass flow rate and manifold outlet length

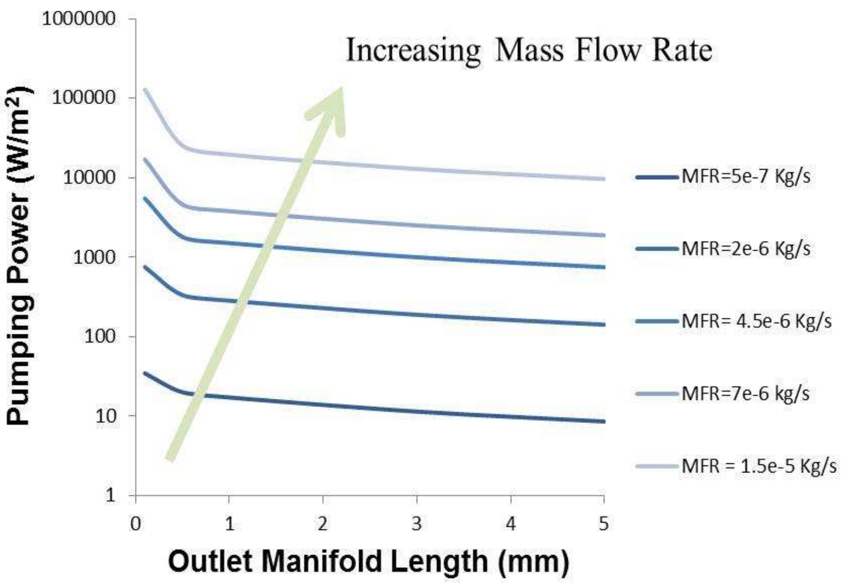

Figure 4-27: Pumping power variation with varying mass flow rate and manifold outlet length

In summary, it can be concluded from the above study that microchannel dimensions are critical for obtaining optimum heat transfer coefficient and pumping power flux. It is necessary to keep the manifold width dimensions as small as possible to obtain a higher heat transfer coefficient and lower pumping power values, which aligns with the literature review. In the next section, an optimization study has been conducted using the Dynamic-Q optimization method to further validate the findings.

4.1.4 Numerical Optimization

The design optimization problems are solved in ANSYS IcePAK using the Dynamic-Q optimization. It is an efficient constrained optimization method consisting of a dynamic trajectory optimization algorithm to successive quadratic approximations to the actual optimization problem. Compared to traditional optimization algorithms used for well-defined objective functions, Dynamic-Q is used for computationally intensive problems where time-consuming numerical simulations are required for function evaluations. For computational fluid dynamics simulations, finite element method or dynamic simulation of multi body system, relevant functions are not known analytically and numbers of variables are large; hence traditional algorithm cannot be used.

A general non-linear optimization problem looks like:

$$\begin{aligned}&\min_x f(x); x=(x_1,x_2,....,x_n)\in R^n\\&subject\,to\, g_j(x)\le 0; j=1,2....p\\&h_k(x)=0; k=1,...,q\end{aligned}\tag{4-13}$$

where $f(x)$, $g_j(x)$, $h_k(x)$ are scalar functions of x.

In the Dynamic-Q approach, successive sub problems are generated at successive approximations by constructing spherically quadratic approximations where the approximated functions are given by:

$$\begin{aligned}&\tilde{f}(x)= f(x^i)+\nabla^T f(x^i)(x-x^i)+\frac{1}{2}(x-x^i)^T A(x-x^i);\\&\tilde{g}_j(x)=g_j(x^i)+\nabla^T g_j(x^i)(x-x^i)+\frac{1}{2}(x-x^i)^T B_j(x-x^i); j=1,....,p\\&\tilde{h}_k(x)=h_k(x^i)+\nabla^T h_k(x^i)(x-x^i)+\frac{1}{2}(x-x^i)^T C_k(x-x^i); k=1,....,q\end{aligned}\tag{4-14}$$

where A, B_j and C_k are the Hessian matrices of the simple forms:

$$A=diag(a,a,....,a)=aI; B_j=b_jI; C_k=c_kI\tag{4-15}$$

where

$$\begin{aligned} a &= \frac{2\left[f\left(x^{i-1}\right)- f\left(x^{i}\right)-\nabla^{T} f\left(x^{i}\right)\left(x^{i-1}-x^{i}\right)\right]}{\left\|x^{i-1}-x^{i}\right\|^{2}} \\ b_{j} &= \frac{2\left[g_{j}\left(x^{i-1}\right)- g_{j}\left(x^{i}\right)-\nabla^{T} g_{j}\left(x^{i}\right)\left(x^{i-1}-x^{i}\right)\right]}{\left\|x^{i-1}-x^{i}\right\|^{2}} \\ h_{k} &= \frac{2\left[h_{k}\left(x^{i-1}\right)- h_{k}\left(x^{i}\right)-\nabla^{T} h_{k}\left(x^{i}\right)\left(x^{i-1}-x^{i}\right)\right]}{\left\|x^{i-1}-x^{i}\right\|^{2}} \end{aligned} \qquad (4\text{-}16)$$

In many optimization problems, additional side constraints represent upper and lower boundaries for the variables. Since these constraints have zero curvature, they are not approximated in the Dynamic-Q method. They are explicitly treated as linear inequality constraints having upper and lower bounds. Additional constraints are described which have the form:

$$\begin{aligned} &\hat{g}_{j}(x) = \hat{k}_{vl} - x_{vl} \leq 0; l = 1,2,....r \leq n \\ &\check{g}_{m}(x) = x_{wm} - \check{k}_{wm} \leq 0; m = 1,2,....,s \leq n \\ &g_{\delta}(x) = \left\|x - x^{i-1}\right\|^{2} - \delta^{2} \leq 0 \end{aligned} \qquad (4\text{-}17)$$

After constructing a local approximation optimization problem, the sub problem is further solved using a constrained optimizer LFPOC (Dynamic Trajectory Leap Frog Optimization method). The numerical optimization was performed using the above method, which went for several iterations and trails for the following parameter range defined.

$$H_{base,micr} = 0.1 \;\; mm \;; \qquad q^{"} = 50{,}000 \;\; W/m^2;$$

$$\overset{\bullet}{m} = 4.5e-6 \;\; kg/s;$$

$$0.01 \;\; mm < w_{ch,micr} < 1 \;\; mm; \qquad 0.01 \;\; mm < t_{fin,micr} < 1 \;\; mm$$

$$0.5 \;\; mm < H_{fin,man} < 2 \;\; mm; \qquad 0.1 \;\; mm < H_{fin,micr} < 1 \;\; mm$$

$$0.5 \;\; mm < W_{ch,man\_inlet} < 2 \;\; mm; \qquad 0.5 \;\; mm < W_{ch,man\_outlet} < 2 \;\; mm$$

$$0.5 \;\; mm < t_{fin,man} < 2 \;\; mm \tag{4-18}$$

$$h \geq 100{,}000 \, W/m^2 - K$$

The objective function was constructed using the ratio of heat transfer coefficient and pumping power flux. A minimum value of heat transfer coefficient is defined to get a reasonable higher value. Several iterations were run and the results are summarized in Figure 4-28. The best optimum point corresponded to the following values:

$$H_{base,micr} = 0.1 \;\; mm \;; \qquad q^{"} = 50{,}000 \;\; W/m^2; \quad \overset{\bullet}{m} = 4.5e-6 \;\; kg/s;$$

$$w_{ch,micr} = 0.01764 \, mm; \qquad t_{fin,micr} = 0.1509 \, mm;$$

$$H_{fin,man} = 0.5 \;\; mm; \qquad H_{fin,micr} = 0.2864 \;\; mm;$$

$$W_{ch,man\_inlet} = 0.5 \;\; mm; \qquad W_{ch,man\_outlet} = 0.5 \;\; mm;$$

$$t_{fin,man} = 0.5 \;\; mm; \;\; h{=}154300 \;\; W/m^2 - K; \quad P^{"} = 3634 \;\; W/m^2 \tag{4-19}$$

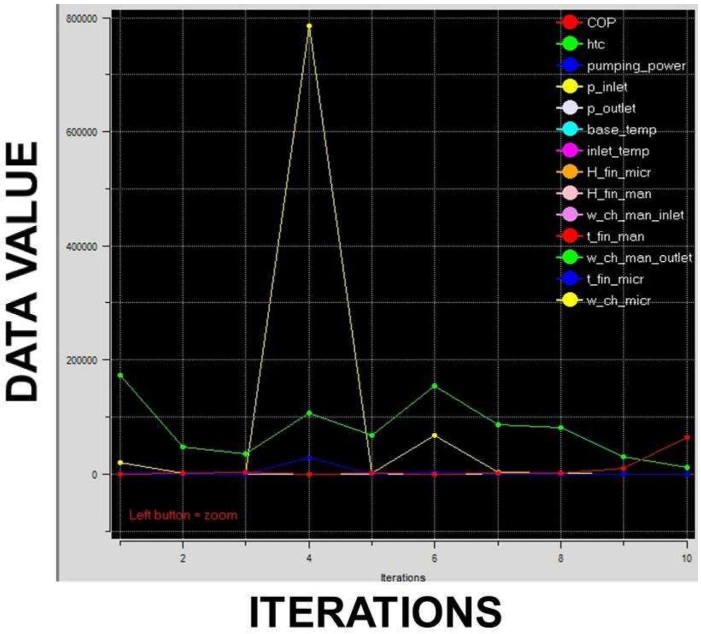

Figure 4-28: Optimization iterations in IcePAK using multiple geometrical variables

The results agree strongly with the parametric studies done where smaller manifold and microchannel dimensions are preferred. The optimization selection falls on the lower boundaries for manifold dimensions. However, the optimization takes a significant amount of computation time and further study was conducted by reducing few parameters. Also, study of mass flux variable is feasible by keeping the manifold dimensions to a lower practical value and varying the microchannel dimensions.

An optimization study was conducted for 25 iterations with various trials for a fixed mass flux and manifold dimensions but with varying microchannel dimensions. The convergence chart is shown in Figure 4-29.

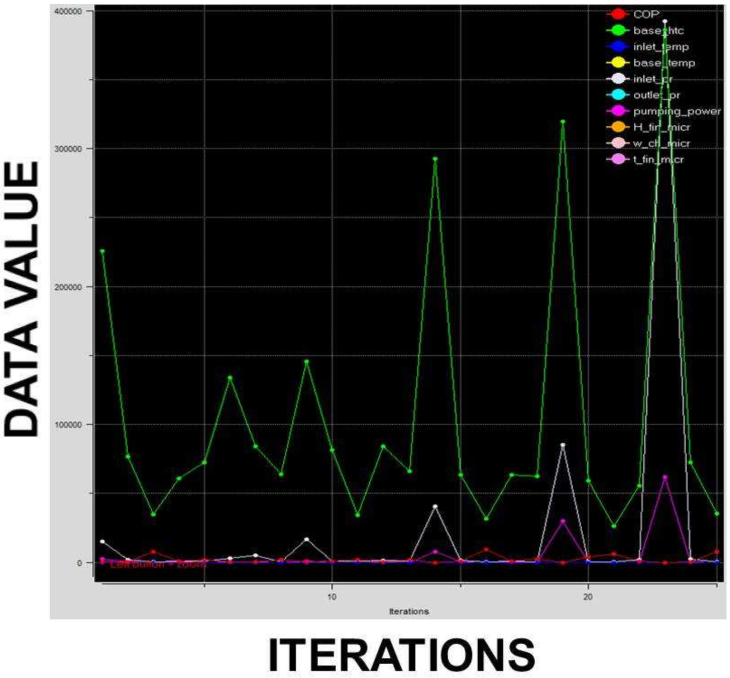

Figure 4-29: Iteration runs for fixed mass flow rate and manifold dimensions but varying microchannel dimensions

Table 4-3 shows all design points from where the optimum point can be chosen. The data marked in red shows the most optimum point where sufficiently high heat transfer coefficient value is achieved with lower pumping power flux values. The data in green shows potential design candidates for which much higher heat transfer coefficients are obtained but at a higher pressure drop penalty. It can be deduced from the data that much finer dimensions with higher aspect ratio (> 5) are needed.

Table 4-3: Design points based on optimization results for constant mass flux and manifold dimensions

Microchannel Fin Height (mm)	Microchannel Width (mm)	Microchannel Fin Width (mm)	Base HTC (W/m^2-K)	Pumping Power (W/m^2)
0.3	0.03	0.03	2.26E+05	2253
0.12	0.09903	0.01	7.66E+04	162
0.3	0.197	0.1029	3.46E+04	4.367
0.4959	0.07988	0.01	6.07E+04	82.49
0.3159	0.08567	0.108	7.27E+04	43.3
0.337	0.0518	0.0195	1.34E+05	391.5
0.157	0.05677	0.1175	8.44E+04	265.5
0.337	0.1065	0.0195	6.41E+04	35.26
0.2979	0.02906	0.1175	1.46E+05	1044
0.2965	0.087	0.0195	8.16E+04	74.66
0.1165	0.185	0.1175	3.45E+04	18.75
0.3106	0.07094	0.01	8.43E+04	156.1
0.2842	0.09412	0.108	6.62E+04	35.68
0.3076	0.02082	0.02547	2.92E+05	7915
0.1276	0.1188	0.01	6.35E+04	84.36
0.3076	0.2168	0.108	3.15E+04	3.287
0.5207	0.07477	0.01	6.33E+04	102.3
0.3407	0.104	0.108	6.23E+04	23.29
0.3628	0.01545	0.01	3.20E+05	3.01E+04
0.5428	0.1134	0.108	5.91E+04	14.74
0.3628	0.2114	0.01	2.63E+04	4.386
0.1629	0.08812	0.1495	5.56E+04	65.88
0.2281	0.01	0.04691	3.86E+05	6.20E+04
0.1	0.108	0.01	7.25E+04	171.3
0.28	0.206	0.06486	3.54E+04	4.714

A further study was conducted to vary the mass flow rate, keeping the initial solution as the optimized solution from previous study. This was done to determine whether a similar trend of design points is preferred for an optimum mass flow rate. The optimum point fell on the upper boundaries of the mass flow rate with larger microchannel dimensions (> 0.1 mm channel width). Though the pressure drops were much lower for all the iterations, heat transfer coefficient was not sufficiently good. The results indicate mass flow rate can significantly influence the design points and should be considered for optimizing the system.

4.1.5 Summary

A comprehensive study for single-phase flow for manifold microchannel was performed using ANSYS IcePAK. All important geometrical and flow parameters were considered for the parametric study, and further optimization using the Dynamic-Q algorithm was performed to validate the findings. The following conclusions can be drawn:

a) Microchannel width is the most critical parameter that basically affects the mass flux inside the channel. Fluid flow and heat transfer behavior is significantly affected for both low and high Reynolds number. For lower Reynolds number, fluid bypasses through the upper part of the microchannel creating a stagnation zone at the bottom of the channel which leads to a lower heat transfer coefficient. For higher Reynolds number, mean velocity is higher at the bottom part of the microchannel which enhances the heat transfer behavior.

b) There lies an optimum for both fin width and fin height as the graph passes through a peak. This is in agreement with analytical study where fin efficiency is an important factor to consider.

c) Manifold dimensions (fin thickness, channel width and channel height) should be kept smaller to have better heat transfer coefficient and lower pressure drops.

d) Mass flux significantly affects the pressure drop and heat transfer rate in all the cases. The optimum points would change if mass flux is also considered a separate variable for the optimization study.

The current study provides a guideline for selection of the parameter for the tubular evaporator which is the focus for next chapters. The tubular microgroove surface has high aspect ratio microchannels on the outer side and minichannels on the inner side. A preliminary design was considered utilizing manifold flow on both sides, and later the design transitioned to enhanced header designs. The manifold header on the outer side had smaller dimensions, which led to very modest pressure drop and good overall heat transfer coefficient.

CHAPTER 5: TUBULAR EVAPORATOR DESIGN AND EXPERIMENTAL SETUP

This chapter focuses on the development of the tubular evaporator and its fabrication methodologies. Further, the experimental setup used in the study is discussed along with the specific instrumentation used.

5.1 Microgrooved Tubular Evaporator – Design and Development

Several fabrication methods are used to make microchannels on different material surfaces. Silicon microchannel fabrication techniques can create fine channels with small hydraulic diameters. Micromachining is the more popular conventional method, which creates channels using electron discharge machining or micro-milling. Wolverine Microcool Inc. (Decatur, AL) has patented a novel micro-deformation technology which mechanically and plastically deforms the surface to form finite and repeatable channels [67]. It can be used on a wide range of materials, from rubber to titanium. High aspect ratio microchannels (up to 20X) can be made with a fin density of 25 to 625 per inch (based on material choice). The tubular microgrooved evaporator design utilizes this technology for making the heat exchanger surface with water flowing on the inner side (through minichannels) and refrigerant flowing on the outer side (through high aspect ratio microchannels). Several designs made of aluminum and nickel microgroove surface with different kind of inner tube inserts and outer headers were experimentally evaluated in terms of cooling capacity, heat transfer coefficient and pressure drop. The evaporator design was improved in successive iterations after collecting and analyzing experimental data. The target objective was to achieve 5 kW cooling capacity with ammonia as refrigerant and ethylene glycol as the process fluid. Due to restricted facility availability and strict ammonia regulations, initial tests had to be conducted using R134a/water instead of ammonia/ethylene-glycol, as shell and tube side fluids, respectively.

The choice of refrigerant R134a was based on its easy accessibility and higher saturation pressure which closely simulates the ammonia conditions. However, ammonia has much better thermodynamic properties in terms of latent heat of vaporization and pressure drop, which would lead to better heat transfer rate. Latent heat of vaporization of ammonia is roughly six times higher than R134a. A comparison of R134 and ammonia important properties has been provided in Table 5-1.

Table 5-1: Comparison of ammonia (NH_3) vs. R134a properties

Properties/Index	Ammonia	R134a	Comments
Ozone Depletion Potential	0	0	
Global Warming Potential	0	1300	Ammonia is an excellent natural refrigerant
Critical Temperature	132 °C	101.06 °C	Higher critical temperature enables higher COP including high condensing temperatures
Latent heat of vaporization	1369 KJ/Kg	216 KJ/Kg	Higher latent heat of NH3
Dynamic Viscosity	9.92 µPa-s (25 °C, 7 bars)	195 µPa-s (25 °C, 7 bars)	Smaller viscosity leads to lesser pressure drop
Vapor density	0.59	3.5	NH3 is lighter than air and rises in case of leak.
Odor	Strong	Odorless	NH3 can be smelled at 5 ppm, a value 100 times smaller than tolerance limit

The fabricated assembly of the microgrooved evaporator and its components are shown in Figure 5-1.

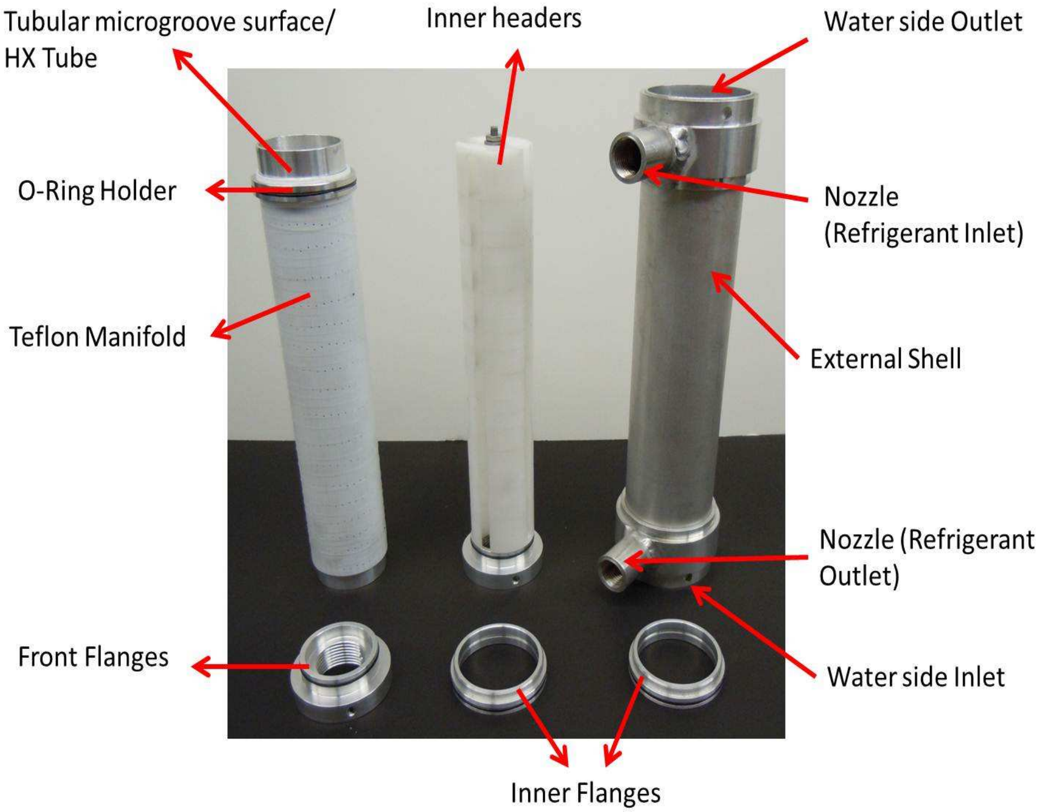

Figure 5-1: Tubular evaporator assembly made of aluminum microgroove surface and aluminum shell material

The particular example assembly shown above is for an aluminum microgroove tube with manifold headers on both sides. In other assemblies, the design methodologies changed only in terms of the water-side header design, selection of microgroove & shell material, and manifold geometrical dimensions. The rest of the construction remained the same. More details will be provided case by case in further chapters where experimental results are discussed. The assembly shown above is 1.315 Kg in weight and has external diameter of 63.5 mm and length of 305 mm. Outer headers in all cases were made of Teflon material, which has usually poor thermal conductivity but is easy to machine because it is not hard and is light weight. Inner headers are made of Delrin & PVC material, which is less expensive than Teflon.

All design assemblies and the important geometrical dimensions are shown in Table 5-2.

Table 5-2: Design assembly materials and important geometrical dimensions

Assembly No.	HX Tube: Outside diameter: 51.2 mm; Inside diameter: 46.432 mm; Axial Length = 254 mm Set 1: ➢ Material: Aluminum 6061 (Thermal conductivity: 205 W/m-K at 25 ^{o}C) ➢ Outside fin width: 102 µm; Fin height: 305 µm; Outside channel width: 102 µm; Number of fins: 1270; ➢ Triangular channel fin width: 0.8 mm ; Fin Height: 1.37 mm, 60^{o} ; Channel width: 0.8 mm ; Number of fins: ~ 320 Set 2: ➢ Material: Aluminum 6061 (Thermal conductivity: 205 W/m-K at 25 ^{o}C) ➢ Outside fin width: 60 µm; Fin height: 600 µm; Outside channel width: 60 µm; Number of fins: 2116; ➢ Triangular channel fin width: 1.01 mm ; Fin Height: 1.17 mm, 60^{o} ; Channel width: 0.8 mm ; Number of fins: ~ 250 Set 3: ➢ Material: Nickel 200 (Thermal conductivity: 90 W/m-K at 25 ^{o}C) ➢ Outside fin width: 100 µm; Fin height: 600 µm; Outside channel width: 200 µm; Number of fins: 850; ➢ Triangular channel fin width: 1.01 mm ; Fin Height: 1.17 mm, 60o ; Channel width: 0.8 mm ; Number of fins: ~ 250 Outer Header: Length = 254 mm Force-fed/Manifold Flow mechanism; Set 1: ➢ Material: Teflon (Thermal conductivity: 0.23 W/m-K at 23 ^{o}C) ➢ Slot height: 787 µm; Base height: 813 µm; Slot width: 1016

µm; Manifold width: 1270 µm; 36 slots for inlet and 36 slots for outlet

Set 2:

- Material: Teflon (Thermal conductivity: 0.23 W/m-K at 23 ^{o}C))
- Slot height: 2 mm; Base height: 813 µm; Slot width: 2 mm; Manifold width: 2 mm; 20 slots for inlet and 20 slots for outlet

Inner Header: Length = 254 mm
Set 1:

- Force-fed/ Manifold Flow mechanism
- Material: Delrin (Thermal conductivity: 0.4 W/m-K at 25 ^{o}C)
- Slot height: 787 µm; Base height: 813 µm; Slot width: 1016 µm; Manifold width: 1270 µm; 36 slots for inlet and 36 slots for outlet

Set 2:

- Annular flow mechanism
- Material: PVC
- Annular gap: 2.5 mm

Set 3:

- Annular flow mechanism
- Material: PVC
- Annular gap: 1.5 mm

External Shell/Nozzles/Flanges

Set 1: Material : Aluminum 6061(Thermal conductivity: 205 W/m-K at 25 ^{o}C)

Set 2: Material : Steel (Thermal conductivity: 10 W/m-K at 25 ^{o}C)

1	HX Tube: Set 1 ; Outer Header: Set 1; Inner Header: Set 1; External Shell/Nozzles/Flanges: Set 1
2	HX Tube: Set 1 ; Outer Header: Set 2; Inner Header: Set 1; External Shell/Nozzles/Flanges: Set 1
3	HX Tube: Set 2 ; Outer Header: Set 2; Inner Header: Set 1;

	External Shell/Nozzles/Flanges: Set 1
4	HX Tube: Set 2 ; Outer Header: Set 2; Inner Header: Set 2; External Shell/Nozzles/Flanges: Set 1
5	HX Tube: Set 3 ; Outer Header: Set 2; Inner Header: Set 2; External Shell/Nozzles/Flanges: Set 2
6	HX Tube: Set 3 ; Outer Header: Set 2; Inner Header: Set 3; External Shell/Nozzles/Flanges: Set 2

The refrigerant-side utilizes the benefits of the force-fed evaporation technique which is similar to manifold microchannel design discussed earlier. Force-fed evaporation utilizes the manifold microchannel geometry to decrease the flow length, which in turn decreases the pressure drop. It uses an inlet header placed on top of the microgrooved surface to direct the working fluid (refrigerant) into microchannels on the heat transfer surface. The liquid evaporates into vapor as it passes through a short distance through the microchannel. Vapor flows out of the channel through alternate exit channels. The net effect from the combination of multiple short channels reduces the pressure drop to a great extent and also enhances the heat transfer coefficient when compared to traditional microchannel design. Very high base heat transfer coefficient (> 3,00,000 W/m^{2}K) with a low pressure drop of 12 kPa has been obtained in earlier work done at the S2TS lab, University of Maryland , College Park [31].

The evaporator consists of following components:

a) **Tubular HX tube** – This is the core of the evaporator where actual heat exchange takes place. The inner surface utilizes the minichannels to enhance the heat transfer surface. Different headers were tested to enhance the fluid flow and heat transfer behavior in single-phase flow on the inner tube side. The outer surface has very high-density fins with a high aspect ratio microgrooved structure in combination with flow headers guiding the refrigerant flow as shown in Figure 5-2.

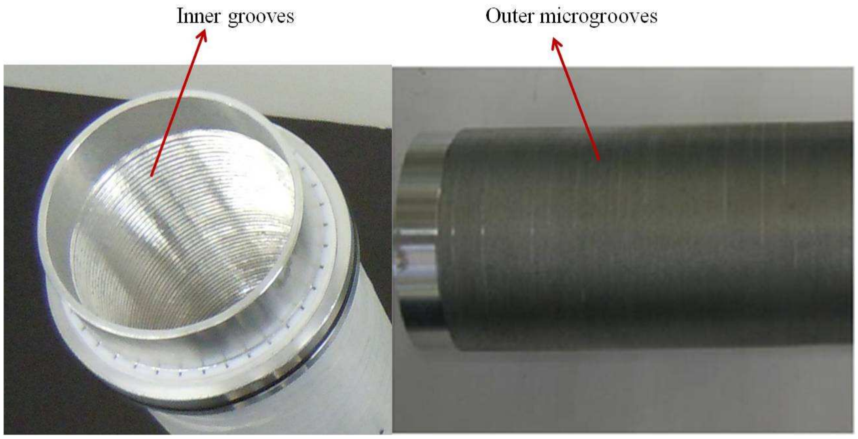

Figure 5-2: Inner HX tube

b) **Inner header** – Two different kinds of inner headers were used for enhancing the water-side heat transfer coefficient. The preliminary design consisted of a manifold guide made of Delrin material and has two cylindrical slots each, for the inlet and outlet. After entering the inlet slots, water moves circumferentially along the HX tube inner surface and exits from the two outlet cylindrical slots located at 90 degrees on each side. Due to manufacturing limitations, it was not feasible to make the whole header in one piece. So it was divided into ten segments, aligned with dowel pins and held together with long bolts. The actual header and schematic of flow mechanism is shown in Figure 5-3.

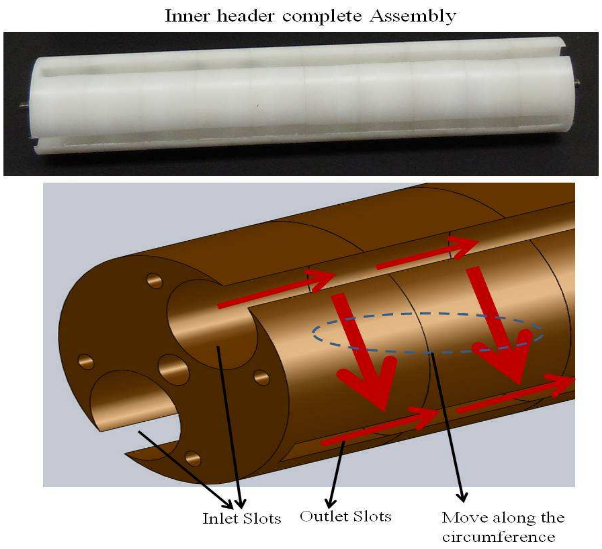

Figure 5-3: Water-side header and flow mechanism

Another design was made of straight PVC pipe which utilized annular flow for very small gaps between the surfaces as shown in Figure 5-4. The simple design was favorable over manifold design in this case because of the absence of microchannels due to manufacturing limitations.

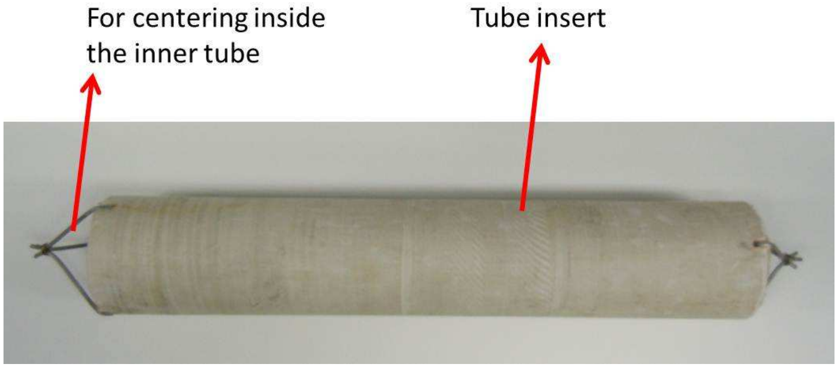

Figure 5-4: PVC tube insert for annular flow in the tube side of the HX

c) **Outer Header** – This was made with a flat Teflon sheet rolled along the cylindrical surface to cover it accurately and was fastened with strong fish strings as shown in Figure 5-5. It was important to ensure that optimum pressure was used so that it didn't damage the microgrooved fins. It was also important not to allow any gap between the surfaces in order to prevent fluid from bypassing the microgrooved channels altogether. The preliminary design has 72 rectangular slots (36 for inlet and 36 for outlet), and the force fed flow concept was utilized. Later, due to high pressure drop issues, manifold dimensions were increased and 20 inlet and outlet feeds were used. Saturated liquid enters the inlet slots, moves circumferentially along microgrooved fins, and saturated vapor exits from the outlet slots. In order to facilitate the vapor exit, several holes were perforated uniformly on the outlet slots. This will not affect the heat transfer performance, as the majority of heat transfer happens along the inner HX tube surface only.

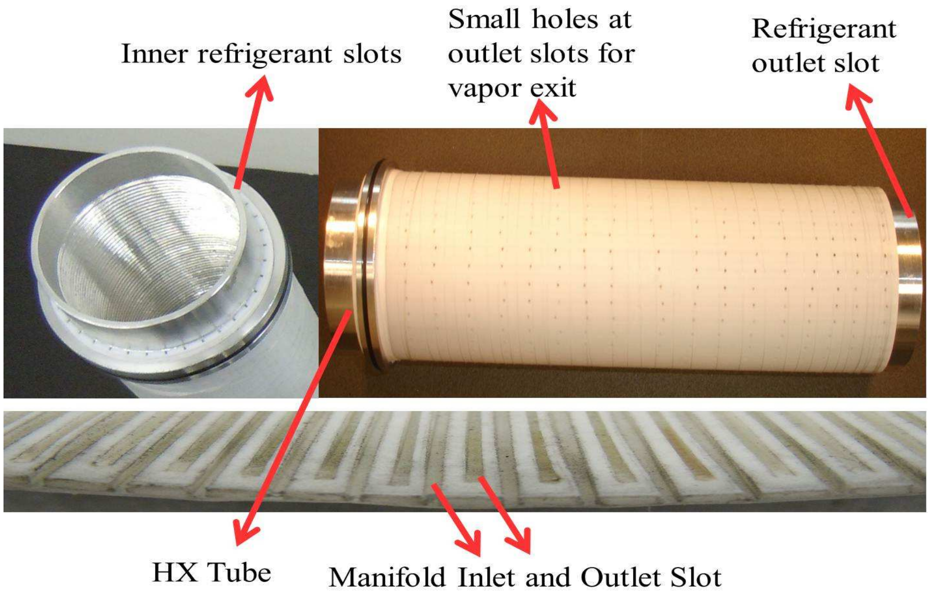

Figure 5-5: Outer header close view

d) **Inner Flanges –** The inner flange as shown in Figure 5-1 seals the volume between the inner HX tube and outer tube, which will be filled with refrigerant vapor once refrigerant exits from the outlet slot holes.

e) **Outer tube, nozzle and inner flanges –** These works as the inlet and outlet flow header for the refrigerant and is shown in Figure 5-1. Refrigerant enters through the nozzle radially and then moves axially through the Teflon rectangular slots. It exits the system also in the same way. As the vapor conductivity is low and the vapor will be continuously flowing, not enough conduction loss will occur through the outer tube to affect the exit temperature measurement. The outer flange was glued to the outer tube with high-strength, low-viscosity epoxy glue. In another improved design and to solve compatibility issues with ammonia, the nozzles and shell were made of steel and welded together.

f) **Front flanges –** These are used for facilitating the water inlet and outlet into the water-side headers as shown in Figure 5-1. Water enters axially through flanges and further directly goes to the inner header slots and exits the system in the same fashion.

g) **O-rings –** Suitable O-rings have been provided for all the flanges, and system was thoroughly tested for pressure leaks. The system has passed much higher pressure tests than the actual operating conditions.

5.1.1 Aluminum microgroove tube assembly

From the design parameters shown in earlier tables, four different assemblies were tested using the aluminum tubes. For this particular design, the nozzle had to be glued on the tube using epoxy, which sustained a pressure of 500 psi.

5.1.2 Nickel microgroove tube assembly

Nickel has much higher Bricknell hardness compared to aluminum. Hence manufacturing microgrooves using deformation was quite a challenging task. Several tubes and tool were damaged at the Wolverine facility and the process was quite expensive. On the outer shell side, the stainless steel nozzle had to be welded on the stainless steel tube. As the stainless steel tube was quite thin (1.65 mm), welding without deformation was quite challenging. Any small deformation made the assembly extremely difficult to fit and seal using O-rings. It required lot of manual correction as the welding deformation made the cross section oval in shape. An external stainless steel ring had to be fabricated and pressed on both side of the tube to maintain the cylindrical shape as shown in Figure 5-6.

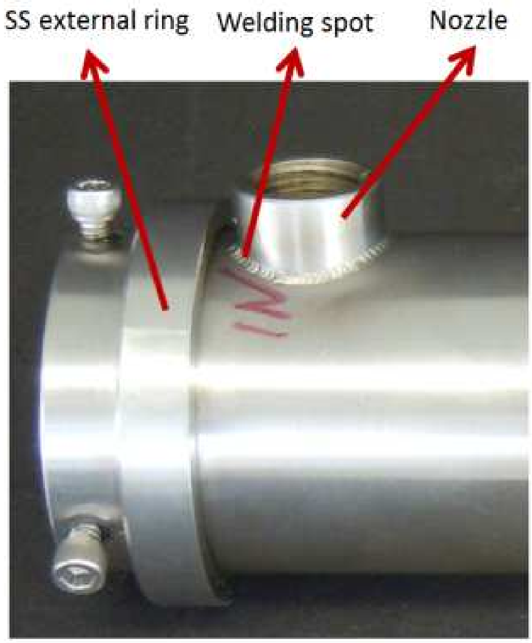

Figure 5-6: SS tube welding assembly

The nickel microgroove assembly is similar to that discussed in earlier section, except with a new outer side header with bigger dimensions and the use of tube insert instead of the manifold design on the water-side. The geometrical dimensions of the tube have been shown in earlier tables and total 2 different assemblies were built using this. The nickel tube assembly and flanges used for the assembly are shown below in Figure 5-7 and Figure 5-8, respectively.

Figure 5-7: Nickel microgroove tube and HX assembly

Figure 5-8: Steel flanges used in the assembly

5.2 Experimental setup & Instrumentations

This section discusses the experimental setup prepared for testing the evaporator at different flow rate and inlet temperature conditions. The list of sensors and transducers used for the setup is also provided. As mentioned earlier in the chapter, R134a was used as refrigerant and deionized water for the process side fluid. Later, the test section was tested with ammonia & ethylene-glycol at an independent ammonia test facility.

A schematic of the experimental flow loop followed by the experimental test setup is shown in Figure 5-9 and Figure 5-10 respectively.

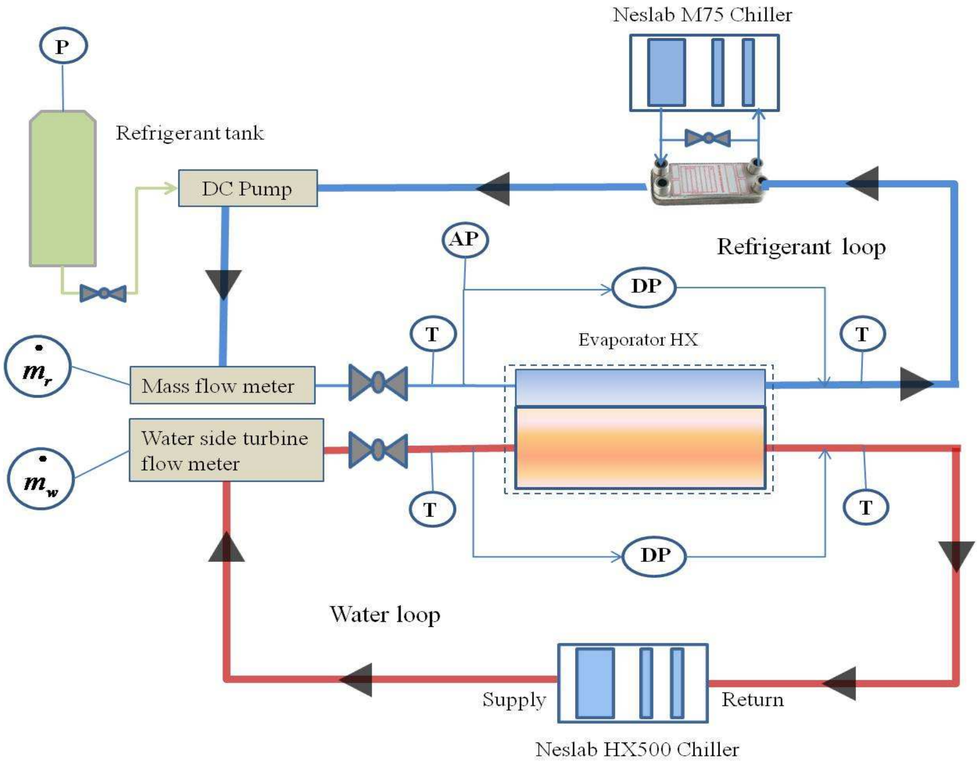

Figure 5-9: Schematic of experimental loop

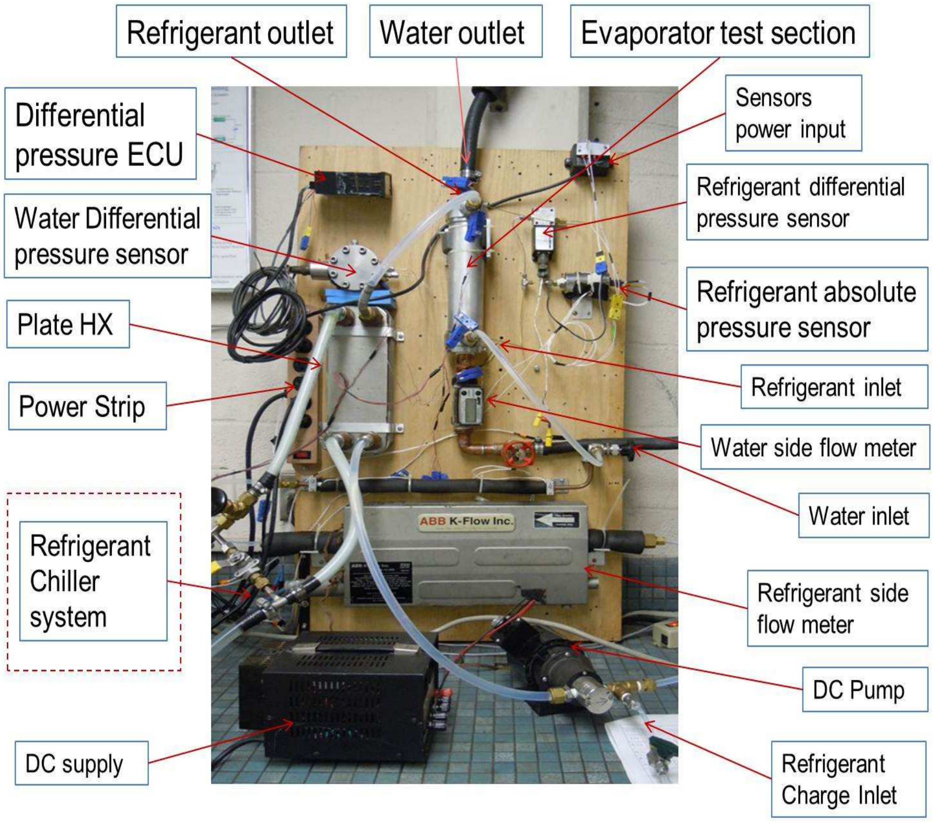

Figure 5-10: Evaporator experimental setup

All components for the setup are mentioned in the figure itself. The evaporator was tested in multiple configurations to test the effects of gravity on fluid distribution inside headers. The setup has two loops, one for the process fluid-water and another for the working fluid/refrigerant. There is a secondary loop (chiller) for keeping the refrigerant at the desired temperature. Before putting the refrigerant charge into the refrigerant loop, the system was completely evacuated using a vacuum pump, while ensuring that absolute pressure was maintained below 25 mbars. When the vacuum is observed for longer period, it is assumed that the system is leak free. The cold refrigerant tank was connected to the refrigerant charge inlet port and opened slowly to attain the desired pressure in the system. It was important to make sure that system was not over charged as this can decrease the PHX efficiency. The thumb rule is to visually observe the static head of liquid refrigerant in the PHX through loop piping and make sure that it is not more than roughly 20% of the height of the PHX. Before conducting any test, a little refrigerant was let out from the highest point of setup so that condensable gases (if any) could exit from the loop. Later, it was verified that absolute pressure data of the refrigerant-side corresponded to the saturation temperature of the refrigerant inlet within 0.2 °C.

A 12V DC supply was used to run the DC pump to obtain the desired refrigerant flow rate. Initially, it was difficult to stabilize the flow rate because of pressure fluctuations. A better control was observed by installing a flow valve in the loop after the flow meter. A flow valve was installed on water-side to get more variations within the maximum limit of differential pressure transducer. To prevent corrosion, 1 g per liter potassium acetate was added to the water reservoir.

The list of instruments used in the experimental setup and their details are given in Table 5-3.

Table 5-3: List of Instruments

Component Name	**Manufacturer**	**Model**	**Operating Range**	**Accuracy**
Water-side Chiller	NESLAB	HX500	+5 ^{o}C to +35 ^{o}C	± 0.1 ^{o}C
Water Flow Meter	GPI Electronic Digital Meter	A108GMN100NA1	3 – 50 GPM	± 1.5 % FS
Water Differential Pressure Transducer	Sensotec	A5/882-12	0 - 5 PSI	± 0.25 % FS
Refrigerant-side Chiller	NESLAB	M75	-15 ^{o}C to +35 ^{o}C	± 0.15 ^{o}C

Refrigerant-side Absolute Pressure Transducer	Setra	280F	0-100 PSI	± 0.20 % FS
Refrigerant-side Differential Pressure Transducer	Validyne	P55D	0 -5 PSI	± 0.25 % FS
Refrigerant Coriolis Flow Meter	ABB K-flow	K5	0-2 kg/min	± 0.10 % FS
Thermocouples	Omega	T-type	-200 °C to +350 °C	± 0.3 %
Plate HX	Alfa Laval	CB26-24H	-	-
DC Pump	FASCO	C4	24V, 4.5 amp	-
DC Supply	Digi Key	35A	0-30V, 3amp	-
Data Acquisition System	Agilent	34970A	20 analog input channels	NA

5.3 Experimental procedure

This section discusses how the experimental runs were conducted and how data were collected and processed. Water was maintained constant at desired temperature and only differential pressure drop was measured across the evaporator. For the refrigerant-side, absolute pressure was measured at the inlet along with the differential pressure drop to know the saturation temperature of the refrigerant. For temperature measurement, four thermocouples per measurement point were used to reduce uncertainty and obtain more accurate readings. The thermocouples were placed at different distance along the diameter of the inlet and outlet to accommodate for the thermal profile. Temperature and pressure measurements and refrigerant flow rate were recorded through a Agilent Datalogger and a GPIB interface with a PC. Water flow rate was recorded manually based on the flow meter reading. An appropriate calibration curve was performed using standard methods to determine the calibration curve incorporated in the final analysis.

The test matrix consists of the following parameters:

- Input
  - Water flow rate
  - Refrigerant flow rate
  - Water Inlet temperature
  - Refrigerant Inlet temperature
- Output
  - Water exit temperature
  - Refrigerant exit temperature
  - Water pressure drop
  - Refrigerant pressure drop

The measurement was recorded once the system reached steady state and flow rates ere stable and constant. Ninety seconds of data were collected after reaching steady state, and the average values were calculated for all measurement points using post processing written in MATLAB. The input values were limited by transducer limits, but the operating limit of the evaporator was well within the range and hence complete assessment can be done.

5.4 Summary

This chapter provides details of the fabrication assembly of the designed tubular evaporator. Six different assembly constructions are prepared using different tube materials, microgroove geometrical dimensions and flow header enhancements. Further, experimental setup is discussed along with the details of instrumentations. The next chapter will focus on presenting the experimental results obtained for different assemblies with different configurations followed by analysis. The experimental results provide the overall heat transfer coefficient and overall pressure drop on both refrigerant and water-sides. Numerical simulation for single-phase water flow provides the water-side heat transfer coefficient. Two-phase flow based on the refrigerant-side heat transfer coefficient was deduced using thermal resistance formula provided in this section.

CHAPTER 6: EXPERIMENTAL RESULTS AND ANALYSIS

This chapter discusses the experimental testing results of the tubular evaporator based on its different design. The design varies in terms of tube material selection and inner and outer flow headers. All the designs result will be discussed case by case and analysis will be given in terms of numerical simulation, wherever applicable.

6.1 Aluminum microgroove tube results – Assemblies 1 & 2

This section discusses the results from two different assemblies having two different refrigerant-side manifold dimensions. As described in Chapter 5, the preliminary design was made of an aluminum microgrooved tube with an aluminum outer tube/shell assembly. On the refrigerant-side/external HX tube side, microgroove tube had 100 µm channel width, 100 µm fin thickness and 300 µm channel height combined with manifold headers. On the water-side, manifold headers were also used which had only 2 inlet and 2 outlet feeds. The tube was tested with two different manifolds on the refrigerant-side, for which the results are presented in this section.

6.1.1 First generation of refrigeration-side manifold – Assembly 1

This section contains results for Assembly 1, for which 1000 µm X 800 µm rectangular manifold dimension were used as described on refrigerant-side as described in Chapter 5. A numerical simulation study using ANSYS IcePAK was also conducted to evaluate the water-side heat transfer coefficient.

6.1.1.1 Experimental results

The refrigerant-side manifold had a rectangular cross section with alternate inlet and outlets. The manifold channel width was 1000 µm, fin thickness was 1270 µm, base height was 810 µm, and channel height was 800 µm. The manifold comprised total 72 slots/feeds with 36 inlets and 36 outlets. The outlet slots had multiple holes for easy vapor outlet, which significantly helped in pressure drop reduction.

Experimental data were collected at a constant refrigerant mass flow rate and varying water mass flow rate and vice versa. Cooling capacity increased with increase in water flow rate but remained almost constant with variation in the refrigerant flow rate in the data studied. The data presented in Figure 6-1 show an uncertainty of ±15% for all data which is evaluated through conventional error propagation method. The refrigerant mass flow rate was varied between 5.16 to 8.02 g/s with a flow rate uncertainty of ±2.5% FS. Water flow rate was constant at 431.5 ml/s with an uncertainty of ±1.5% FS.

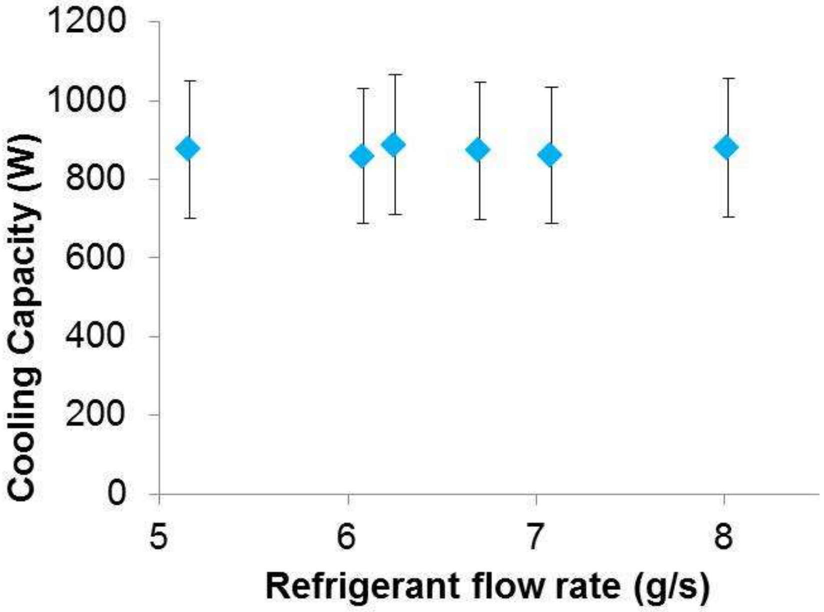

Figure 6-1: Cooling capacity variation with refrigerant flow rate; Constant water flow rate = 431.5 ml/s (6.84 GPM)

With a variation in water flow rate, cooling capacity displayed an increasing trend, as shown in Figure 6-2, with a maximum uncertainty of ±20% mostly associated with temperature measurement. The uncertainty value for these data sets is rather high because of the small temperature difference between the inlet and outlet (~0.5 °C) on the water-side, and the average thermocouple uncertainty is 0.05 °C. To tackle this issue, more thermocouples (for a total of four) were inserted at each measuring point to improve calibration, which maintains the measurement accuracy within 0.0125 °C. LMTD for the data were around 2.2 °C. Heat transfer in excess of 1.1 KW was observed at 800 ml/s water volume flow rate. As this was a preliminary trial, no particular trend could be established because of the two-phase fluid flow and heat transfer complexity on the refrigerant-side. Further, changing the refrigerant flow rate also affects the heat flux for the system, which in turns affects the refrigerant-side heat transfer coefficient.

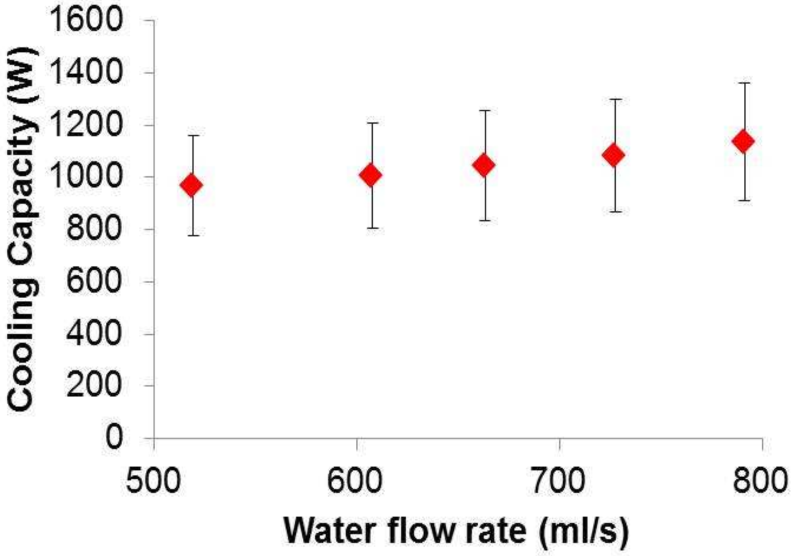

Figure 6-2: Cooling capacity with water flow rate; Constant refrigerant flow rate = 8.3 g/s

As expected, pressure drop was found to increase with mass flow rate for both refrigerant and water. But it was well within the accepted limits of the transducer limits of 300 mbars (5 psi), even for higher mass fluxes. Pressure drop in excess of 300 mbars on water-side and 25 mbar on refrigerant-side was observed as shown in Figure 6-3 & Figure 6-4 respectively. As expected, pressure drop on the water-side was much higher, due to higher mass fluxes; which limited the overall performance.

Overall heat transfer coefficient (U) value increased sharply with variation in water mass flow rate. It was also seen that with an increase in vapor quality, overall heat transfer coefficient shows an increasing trend. Overall heat transfer coefficient as high as 13,500 W/m^2-K at water volume flow rate of 800 ml/s was obtained, as shown in Figure 6-5, which is significantly higher than typical plate evaporators.

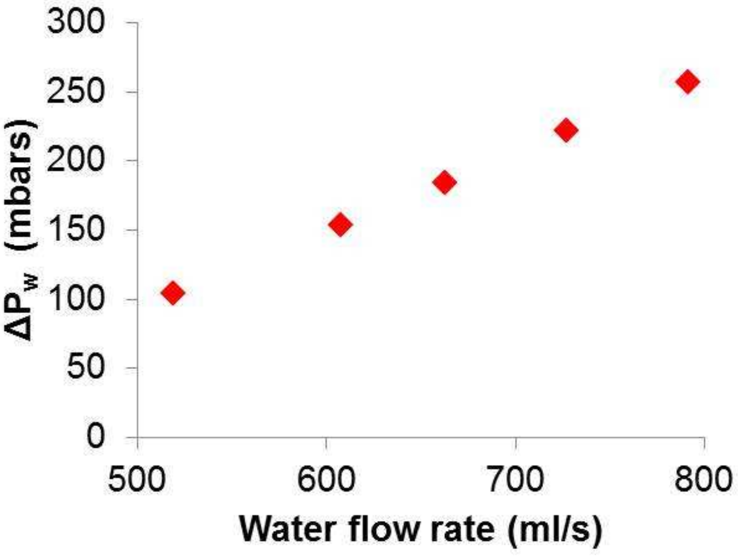

Figure 6-3: Water-side pressure drop variation with water flow rate; Constant refrigerant flow rate = 8.3 g/s

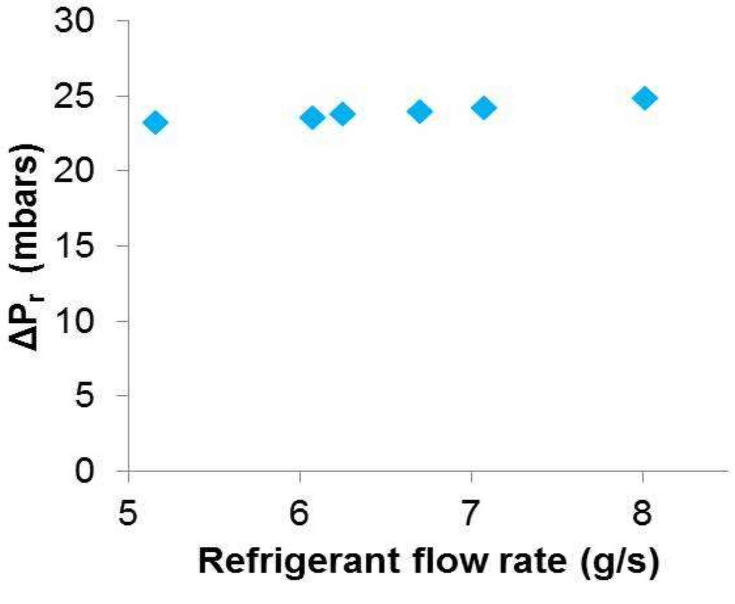

Figure 6-4: Refrigerant-side pressure drop variation with refrigerant flow rate; Constant water flow rate = 431.5 ml/s (6.84 GPM)

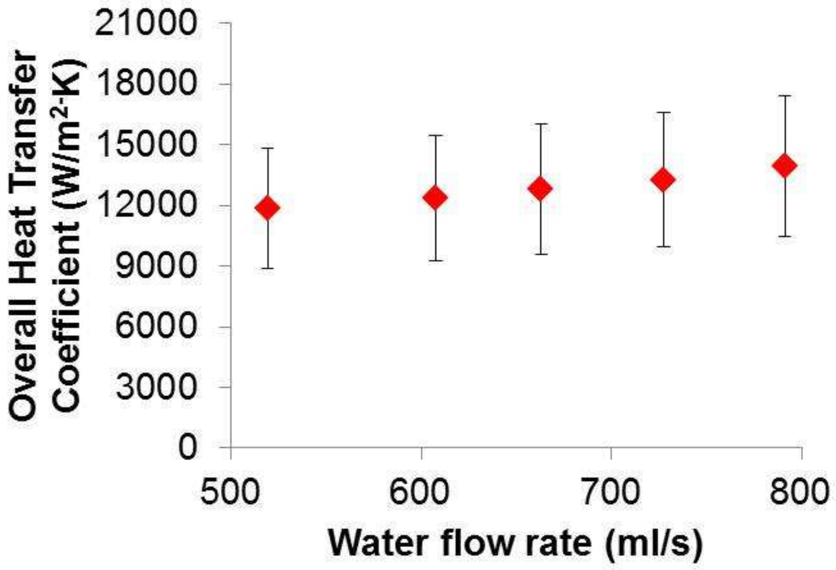

Figure 6-5: Overall heat transfer coefficient variation with water flow rate; Constant refrigerant flow rate = 8.3 g/s

6.1.1.2 Numerical simulation to evaluate water-side heat transfer coefficient

A single-phase numerical simulation was performed using ANSYS IcePAK to evaluate the water-side single-phase heat transfer coefficient. The water-side surface comprises triangular grooves with a manifold guided flow. The geometrical model used for triangular groove flow is shown in Figure 6-6. Due to multiple contraction and expansions in the fluid flow, it is expected that flow will be turbulent despite the lower to medium Reynolds number. It is difficult to predict where exactly flow transition happens. Hence, a turbulent enhanced RNG solver was chosen for carrying out the study. Fin material was considered to be Al-pure and the inlet fluid was water at 25 °C. All the standard properties were taken from the ANSYS IcePAK default database.

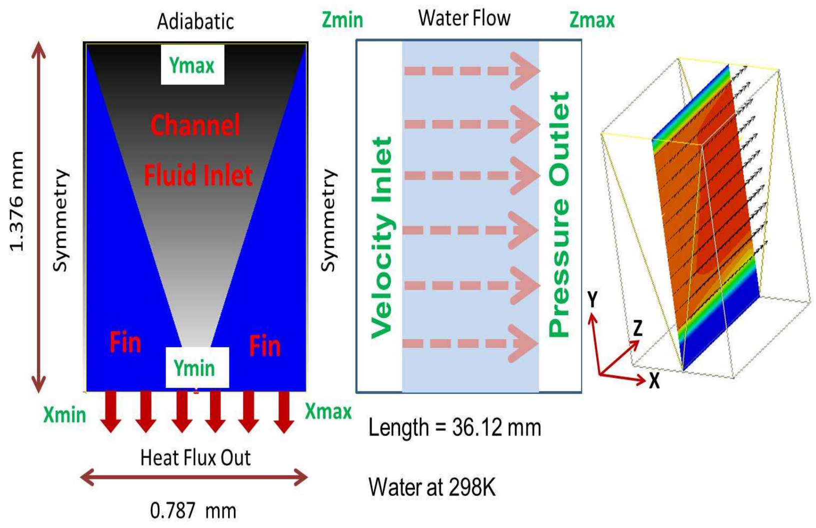

Figure 6-6: Triangular groove geometrical model

The Xmin and Xmax faces are symmetrical due to multiple channel symmetry along this plane. The Ymin face rejects heat to outside of computational domain and the Ymax face is insulated. The Zmax face is set for ambient pressure outlet conditions and the Zmin face represents the fluid inlet and was modeled with constant mass flow rate and pressure drop boundary conditions.

A grid independency study was conducted to choose the optimum size for all the parametric variations, as shown in Figure 6-7 and Figure 6-8. A simulation run is shown for the grid size variations in all spatial directions. Base heat transfer coefficient and pressure drop were monitored at different mass flow rates. It was observed that grid-independency could be achieved with a minimum of 60,000 nodes, and so this was chosen as the optimum grid size.

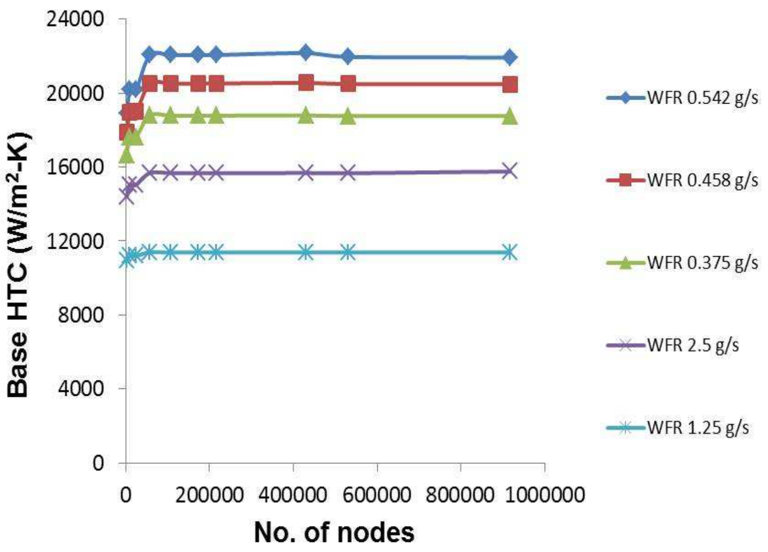

Figure 6-7: Grid independence data for base HTC: Al tube

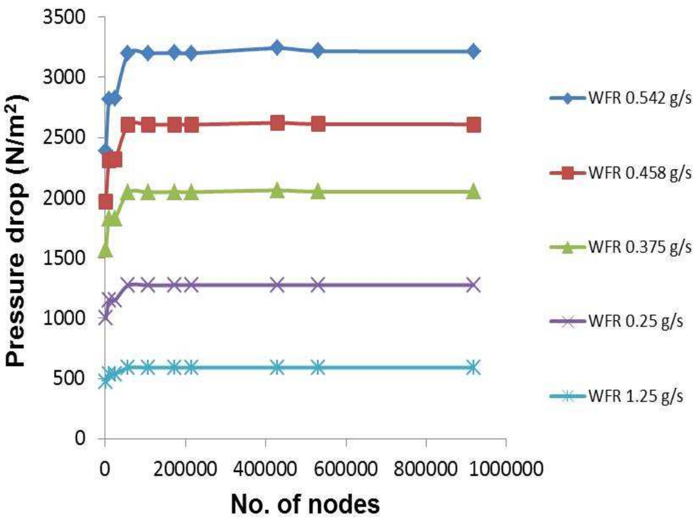

Figure 6-8: Grid independence data for pressure drop: Al tube

The water-side heat transfer coefficient was calculated for varying Reynolds numbers and the results obtained are shown in Figure 6-9. No correlations for developing turbulent flows inside triangular minigrooves was available in literature, hence analytical comparison is not feasible.

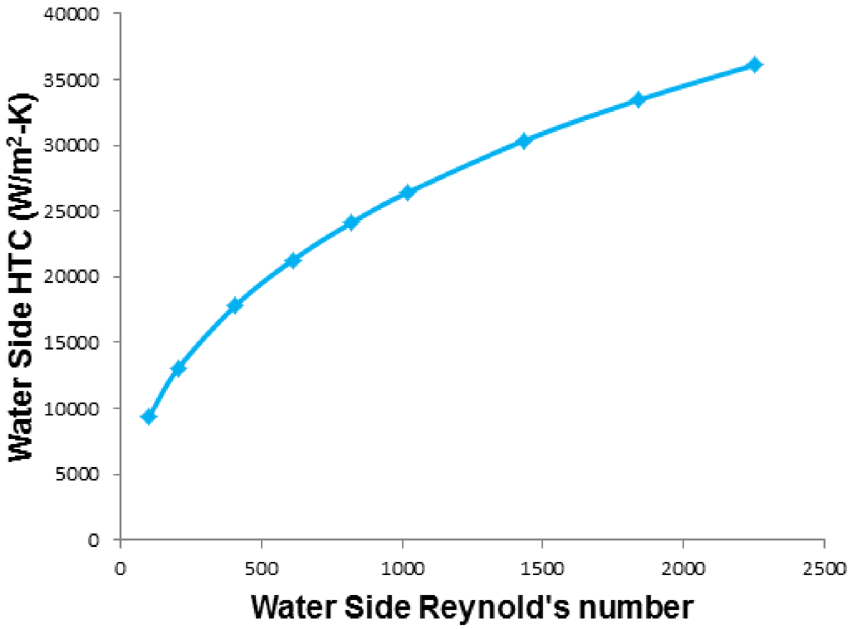

Figure 6-9: Water-side HTC vs. Water-side Reynolds number calculated using numerical modeling

Figure 6-10 shows the overall heat transfer coefficient and individual heat transfer coefficient variation with the water-side Reynolds number using the thermal resistance equation as discussed in Chapter 5. Overall heat transfer coefficient values of 20000-24000 W/m^2-K were obtained for the water-side in the range of the data studied. This heat transfer coefficient value was used further for evaluating the refrigerant-side heat transfer coefficient. The maximum refrigerant-side heat transfer coefficient close to 32,500 W/m^2-K was evaluated for this data range. None of existing literature correlations are applicable for this case and hence no comparison is provided.

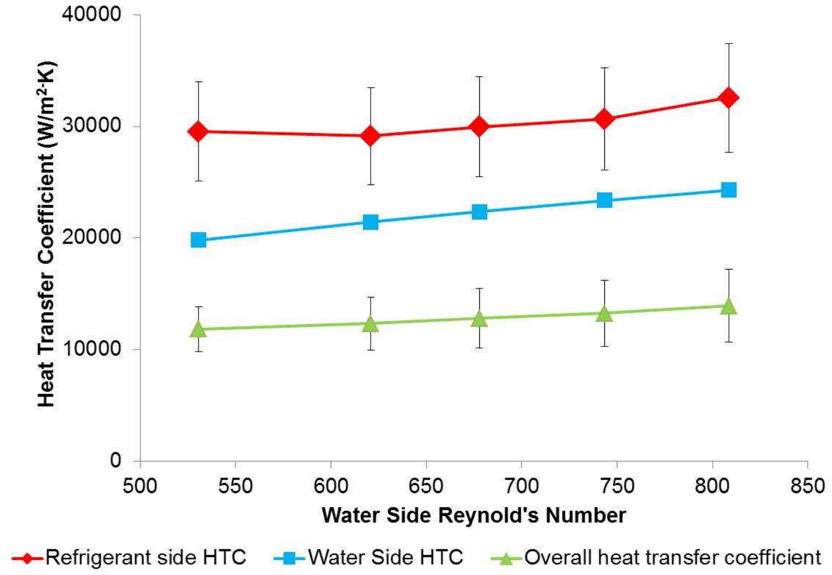

Figure 6-10: Heat transfer coefficient vs. Water-side Reynolds number

Uncertainty calculation was performed for heat transfer coefficients by using the standard error propagation approach method in terms of water-side mass flow rate, water-side inlet and outlet temperature, and saturation temperature of the refrigerant-side as it provides the heat flux.

$$\frac{\Delta U}{U}=\left(\left(\frac{\partial U}{\partial \dot{m}_w}\left(\frac{\Delta \dot{m}_w}{U}\right)\right)^2+\left(\frac{\partial U}{\partial T_{w,in}}\left(\frac{\Delta T_{w,in}}{U}\right)\right)^2+\left(\frac{\partial U}{\partial T_{w,out}}\left(\frac{\Delta T_{w,out}}{U}\right)\right)^2+\left(\frac{\partial U}{\partial T_{sat}}\left(\frac{\Delta T_{sat}}{U}\right)\right)^2\right)^{1/2} \qquad (6\text{-}1)$$

$$where \quad \frac{\Delta \dot{m}_w}{\dot{m}_w}=0.015,\ \ \Delta T_{w,in}=\Delta T_{w,out}=\Delta T_{sat}=0.025\ \ {}^\circ C$$

Table 6-1 shows the experimental parameters and their calculated uncertainties.

Table 6-1: Experimental parameters and calculated uncertainties

Parameters	Uncertainties
Water-side Pressure drop	± 0.25 %
Refrigerant-side Pressure drop	± 0.25 %

Water-side mass flow rate	± 2.5 %
Refrigerant-side mass flow rate	± 0.1 %
Cooling Capacity	± 2-3 %
Overall Heat transfer coefficient	± 1 %
Refrigerant-side heat transfer coefficient	± 10-12 %

6.1.2 Improved header with manifold size – Assembly 2

This section contains results for Assembly 2, for which enhanced manifold size of 2 mm X 2 mm on refrigerant-side was used.

There was a need for improved header design on the refrigerant-side because of lower cooling capacity achieved at higher LMTDs for which the data is not provided. All the data presented in earlier section had an LMTD of approximately 2.2 °C. Upon increasing the LMTD, cooling capacity did not appear to increase in the expected linear trend due to design issues on the refrigerant manifold. When the refrigerant-side mass flow rate was increased, it is believed that a significant portion may have come out of several exit vapor holes leading to lower heat exchange. This was further confirmed when iterative testing was performed by blocking the partial vapor holes and observing the result. Cooling capacity was found to increase but significant pressure drop was encountered on refrigerant-side. It was not feasible to run a full-scale test due to refrigerant-side pressure transducer limits of 5 psi. As the manifold dimensions were significantly small, pressure drop increase was expected if no vapor holes are present. Hence a new set of manifold was fabricated using same design philosophy with bigger channel dimensions of 2mm x 2mm compared to 1000 µm x 1270 µm.

Experimental data were collected for both constant water mass flow rates and constant refrigerant mass flow rates, as shown in Figure 6-11 and Figure 6-12, respectively. The data presented are for two different sets of LMTDs: 5 °C and 6 °C, wherein the LMTD values were estimated based on averaged temperature measurements. The cooling capacity was observed to increase with an increase in the refrigerant flow rate in the lower mass flux range, which was attributed to superheating of the vapor. That is, for low values of refrigerant flow rate, exit state is superheated. However, as the flow rate was increased above 15.3 g/s, the cooling capacity stayed constant close to 2.5 kW. The inlet quality was close to zero as the saturated temperature data at the inlet was found within 0.2 °C for the corresponding saturated pressure data for the refrigerant. The data reported are for a constant water flow rate of 640 ml/s. The refrigerant mass flow rate was varied from 6 to 22 g/s.

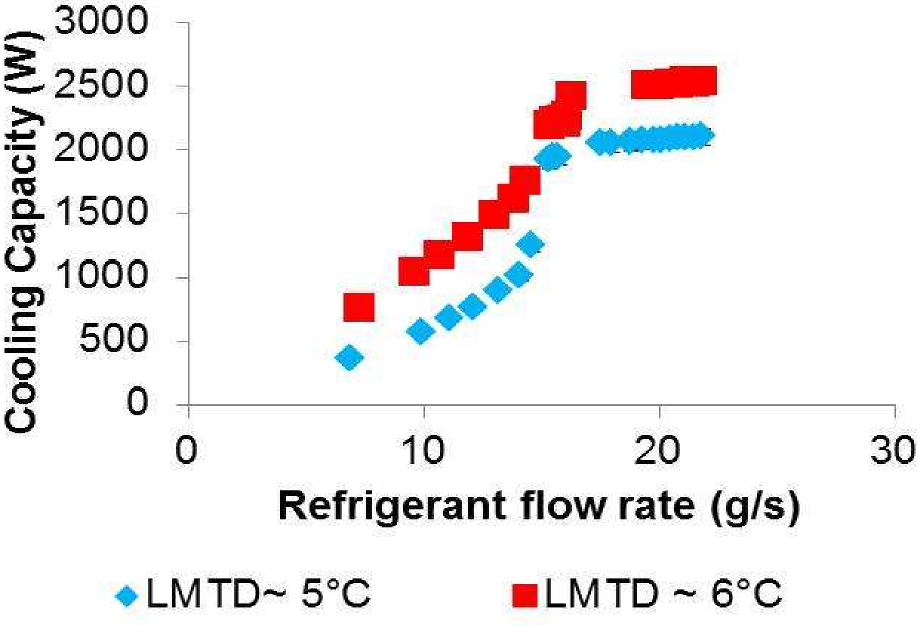

Figure 6-11: Cooling capacity variation with refrigerant flow rate for constant water flow rate of 640 ml/s

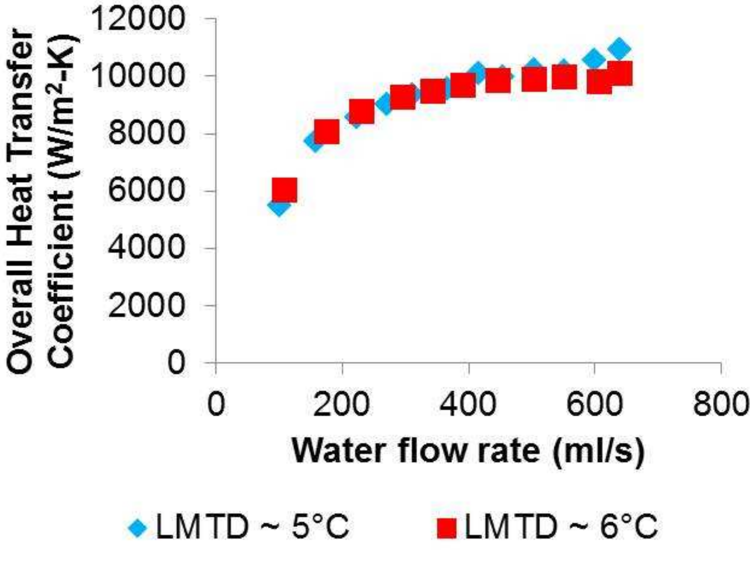

Figure 6-12: Cooling capacity variation with water flow rate for constant refrigerant flow rate of 15.3 g/s

As the refrigerant mass flux was increased, the refrigerant-side heat transfer coefficient increased due to the dominance of forced convection, but due to the decrease in LMTD, the cooling capacity appeared to be constant. While it was desirable to fix the LMTD and observe the variation in cooling capacity, this was not feasible on account of the complex dynamics of the test setup and the chiller capacity limitations, and hence the results had to be interpolated for a fixed LMTD based on linear interpolation from the raw data. The LMTD variation for a particular set of data is not high, hence it is assumed that linear interpolation for achieving constant LMTDs for data set would be accurate.

With a variation in the water mass flow rate, heat transfer rate was observed to increase for lower mass fluxes but asymptote for medium and high mass fluxes as it hits the refrigerant-side heat transfer coefficient limitation. Heat transfer in excess of 2.5 kW was observed at water mass flow rates of 640 ml/s. The refrigerant mass flux was kept constant at 15.3 g/s. As the water mass flux was increased, it was expected that the water-side heat transfer coefficient would increase. A drop of cooling capacity at very low mass fluxes was observed, and this was attributed to the effects of maldistribution that occur inside the channels where the fluid flow is against gravity.

Only moderately high values of mass fluxes were tested in the present study because the pressure transducer range (water-side) was limited to 5 psi. The pressure drop was found to increase with mass flow rate for both refrigerant and water. As shown in Figure 6-13 and Figure 6-14, the pressure drop was around 150 mbars on the water-side at 640 ml/s and 60 mbars on the refrigerant-side at 22 g/s, respectively. The water -side pressure drop curve varied exponentially with increasing water-side flow rate. It was beyond the scope of the study to establish a model for actual pressure drop curve with varying refrigerant flow rate for the refrigerant-side due to a multitude of factors, such as the change in developing flow region, change in vapor quality, the thermo-fluid dynamics of two-phase flow for U-bend , and variations in cooling capacity that would potentially alter the heat flux.

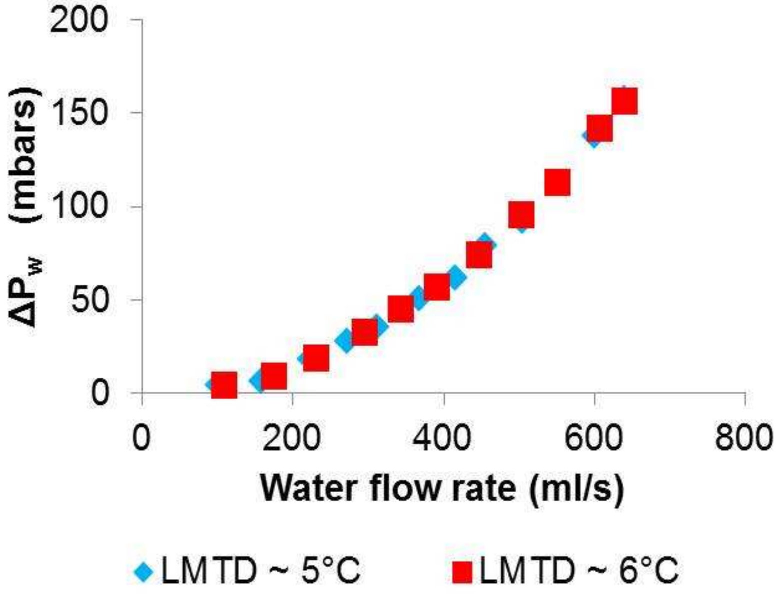

Figure 6-13: Water-side pressure drop variation with water-side flow rate

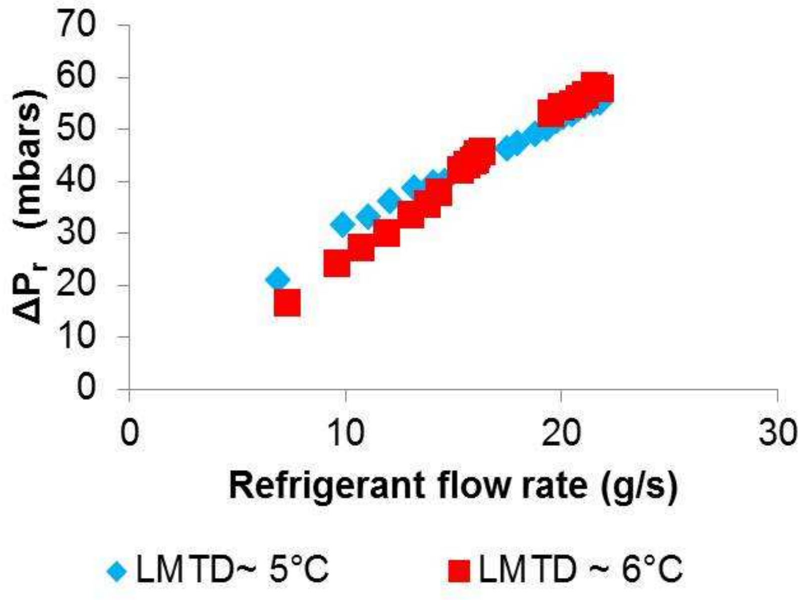

Figure 6-14: Refrigerant-side pressure drop variation with refrigerant flow rate

As shown in Figure 6-15, the overall heat transfer-coefficient increases with an increase in the water mass flow rate. The heat transfer coefficient levels off at a mass flow rate of around 400 ml/s, where it attains a heat transfer coefficient of 10,000 W/m^2-K. With further increase in mass flow rate of water, only modest improvement in the heat transfer coefficient is observed. This is because, the heat transfer coefficient increases for developing flow with an increase in the Reynolds number. Since the overall heat transfer coefficient is the harmonic sum of the waterside and refrigerant-side, it would asymptote towards the refrigerant-side heat transfer coefficient or whichever is the least value. Conduction thermal resistance is much lower compared to both side convective thermal resistance and hence won't play a significant role.

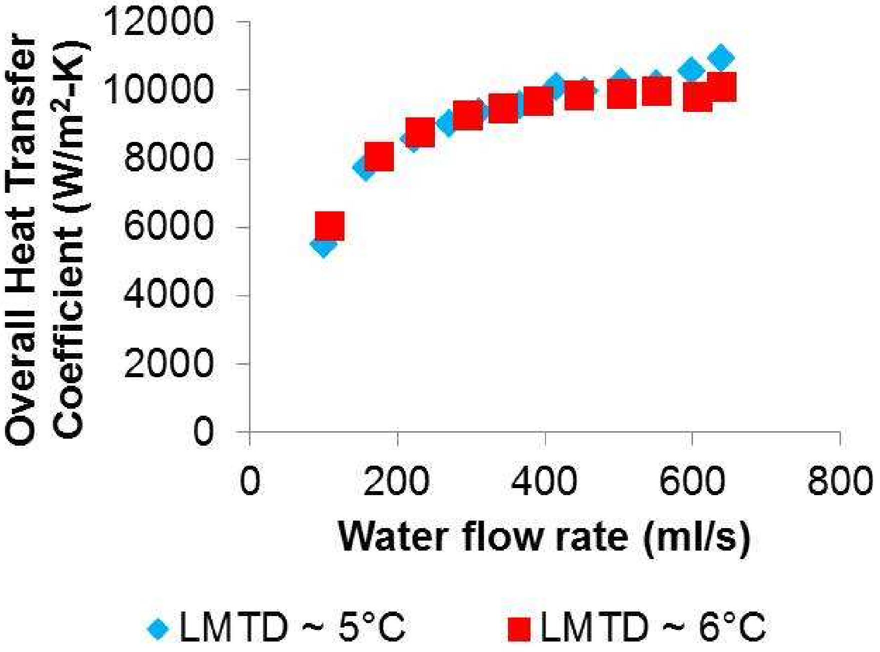

Figure 6-15: Overall heat transfer coefficient variation with water mass flow rate for constant refrigerant mass rate of 15.3 g/s

The overall heat transfer coefficient with increasing refrigerant mass flow in both the superheated and saturated regions is shown in Figure 6-16. As seen there, the heat transfer coefficient does not increase significantly in the saturated region due to the dominance of forced convection and possible maldistribution. However, the overall heat transfer coefficient seems to asymptote as the water-side heat transfer coefficient levels off. At lower refrigerant mass fluxes, superheated vapor is present in the channels and hence there is variability for different set of LMTD’s. At higher exit vapor quality, the heat transfer coefficient was observed to drop to lower values due to partial dryout of the channels. It was not possible to collect data at lower exit vapor quality, as cooling capacity/heat rate and heat transfer coefficient are mutually dependent for the system and cannot be independently studied.

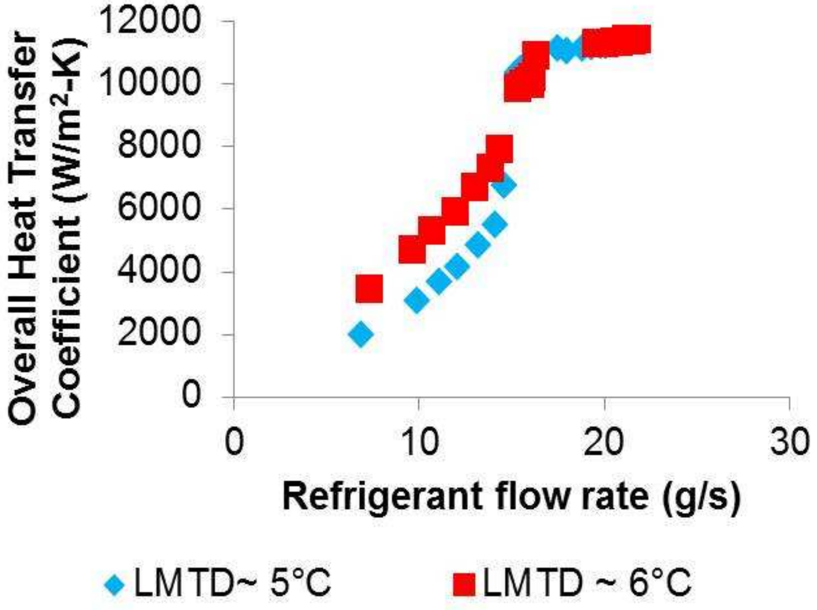

Figure 6-16: Overall heat transfer coefficient variation with refrigerant flow rate for constant water mass rate of 640 ml/s

Using the thermal resistance equation, refrigerant-side heat transfer coefficient was evaluated. The numerical simulation results from the earlier section are utilized for evaluating water-side heat transfer coefficient, since the water-side geometry has not changed. Figure 6-17 shows the overall and individual heat transfer coefficient variations with refrigerant flow rate. Heat transfer coefficient in excess of 30,000 W/m^2-K was calculated for the refrigerant-side for an effective heat flux of 5.33 W/cm^2. It can be seen that the water-side limits the overall heat transfer coefficient due to the presence of less than optimum minichannels on the water-side.

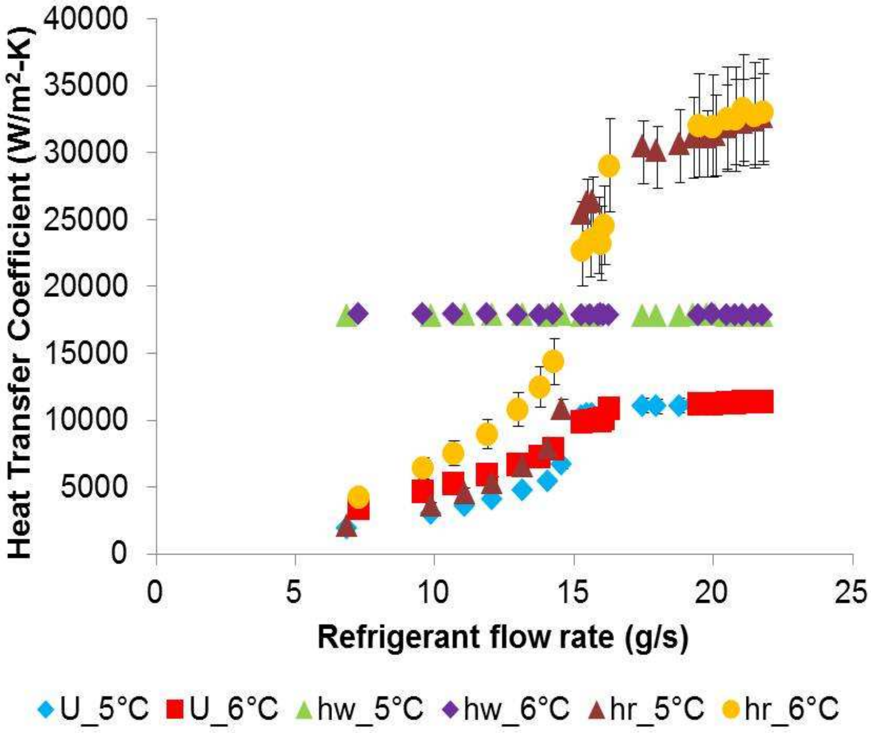

Figure 6-17: Heat transfer coefficient variation with refrigerant flow rate for constant water mass rate of 640 ml/s

In summary, more than 2 kW was achieved with some sacrifice in overall heat transfer coefficient which is attributed to the decrease in refrigerant-side heat transfer coefficient. With increasing LMTD, cooling capacity was found to increase but asymptote due to limitation on water-side heat transfer coefficient. It is difficult to compare this data with smaller manifold dimensions as there was significant maldistribution of the flow owing to vapor exit holes. Also, no higher refrigerant mass flow rate data are available for the previous case. A test was conducted with a brazed plate evaporator having similar size for comparison of the experimental data. Similar cooling capacity was achieved using same set of LMTD’s but five times more heat exchange area which makes the current results promising in terms of performance.

6.2 New aluminum microgroove tube results – Assemblies 3 & 4

Based on the promising results achieved with a larger channel width (100 µm x 300 µm), further testing with a smaller channel width and higher aspect ratio (60 µm X 600 µm) was conducted. The refrigerant-side manifold was similar to the 2mmx 2mm geometry. Based on the numerical simulation study carried out in Chapter 4, it was found that smaller channel width and low to medium aspect ratio can lead to better base heat transfer coefficient, which can lead to higher cooling capacity.

Two different water-side enhancements were also tested with the new tube in an attempt to enhance the water-side heat transfer coefficient. Results are discussed for both the cases. Experimental data were collected for both at constant water mass flow rate and constant refrigerant mass flow rate for both configurations with the force-fed manifold and tube insert on the water-side.

6.2.1 Force-fed manifold on water-side – Assembly 3

Manifolds on the water-side comprised a header made of Delrin material to guide the flow inside the minichannels. Same design principle was used on the refrigerant-side, where microchannels with 60 µm size were used. A schematic of the cross section is shown below in Figure 6-18.

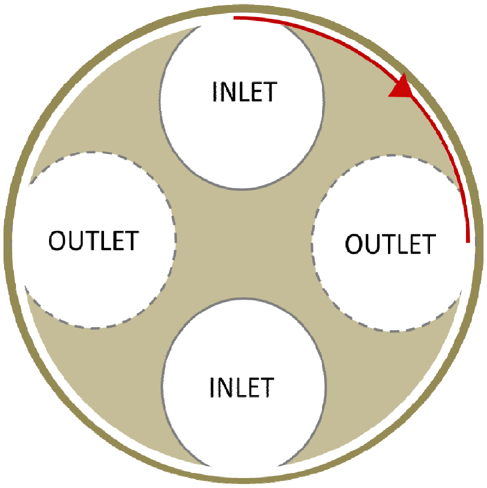

Figure 6-18: Schematic of fore fed header on water-side

Experimental data were collected for different water flow rates and different LMTD values. Cooling capacity was observed to increase with an increase in refrigerant flow rate for all data sets. For lower mass fluxes, cooling capacity data have a different slope, implying the exit state is superheated. As the flow rate increases to 26 g/s, more than 4 kW cooling capacity is seen at LMTD of 12 °C, as shown in Figure 6-19. The data shown are for variable water flow rates from 265 to 580 ml/s, based on the highest chilling capacity available on the water-side. The refrigerant mass flow rate was varied from 8 to 26 g/s. As the refrigerant mass flux increased, refrigerant-side heat transfer coefficient increased due to the dominance of forced convection.

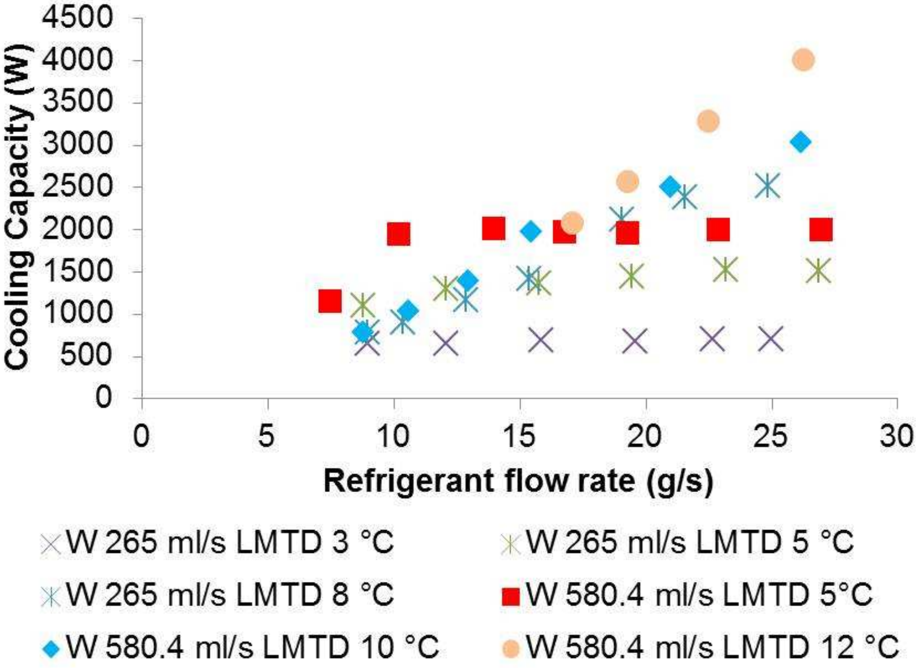

Figure 6-19: Cooling capacity variation with refrigerant flow rate for constant water mass flux

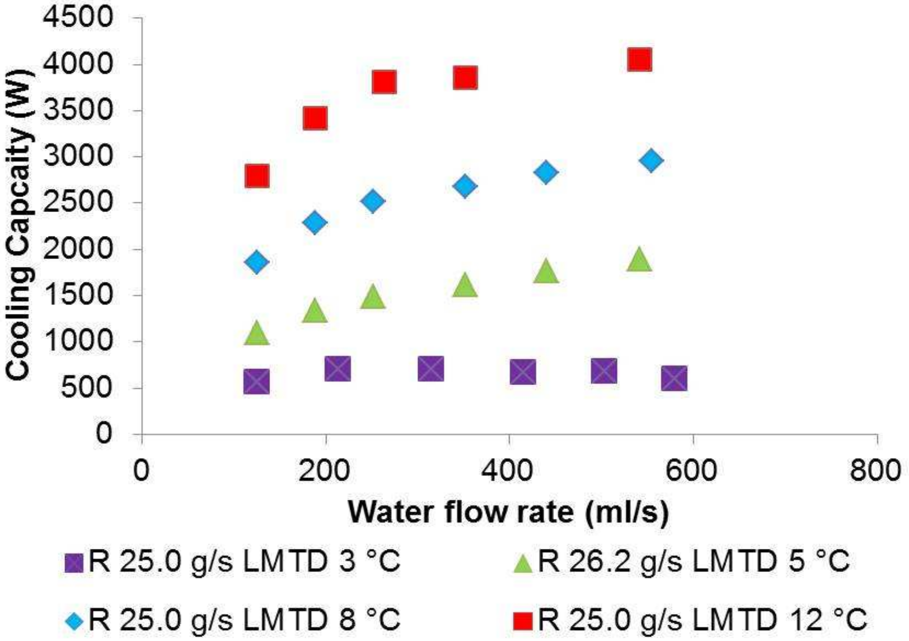

Figure 6-20: Cooling capacity variation with water flow rate for constant refrigerant mass flux

Heat transfer rate was observed to increase for lower mass fluxes but to asymptote for medium and higher mass flux. Heat transfer in excess of 3.8 KW was observed at water mass flow rate of 580.4 ml/s as shown in Figure 6-20. Refrigerant mass flux was kept constant at approximately 25 g/s. With increasing LMTD, it is observed that graph shifts to the top as expected.

As water mass flux is increased, it was expected that the water-side heat transfer coefficient would increase. But, due to a decrease in LMTD, cooling capacity was observed to level off due to refrigerant-side heat transfer coefficient limit. Lower LMTD leads to lower heat flux, which in turns affects the refrigerant-side heat transfer coefficient by reducing the channel vapor quality. As the flow is aligned in the direction of gravity, a drop of cooling capacity at very low water-side mass flux was also observed, which is due to flow maldistribution inside the channels.

Pressure drop was found to increase with increasing mass flow rate for both refrigerant and water, as expected, but it was well within the accepted limits even for higher mass fluxes. The mass fluxes tested were not very high because of transducer limits of 5 psi on the water-side. Pressure drop was in excess of 140 mbar on the water-side at 580.4 ml/s and 100 mbar on the refrigerant-side at 26.0 g/s, as shown in Figure 6-21 and Figure 6-22, respectively. The water-side pressure drop curve trend is similar to what was observed in the earlier Al-tube case but had lower values due the larger triangular groove size. Refrigerant-side pressure drop is increasing with increasing LMTD due to more vapor creation, which leads to higher vapor pressure drop.

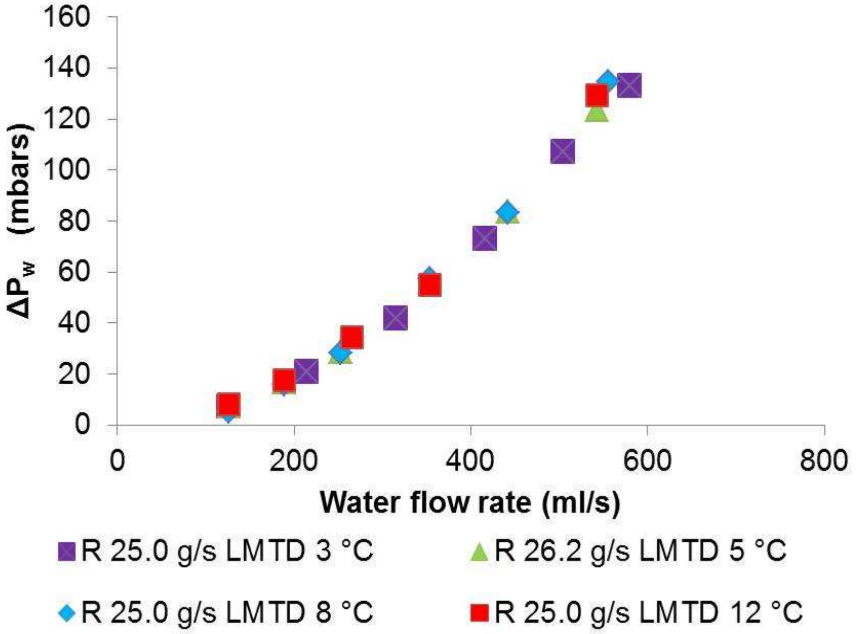

Figure 6-21: Water-side pressure drop variation with water-side flow rate

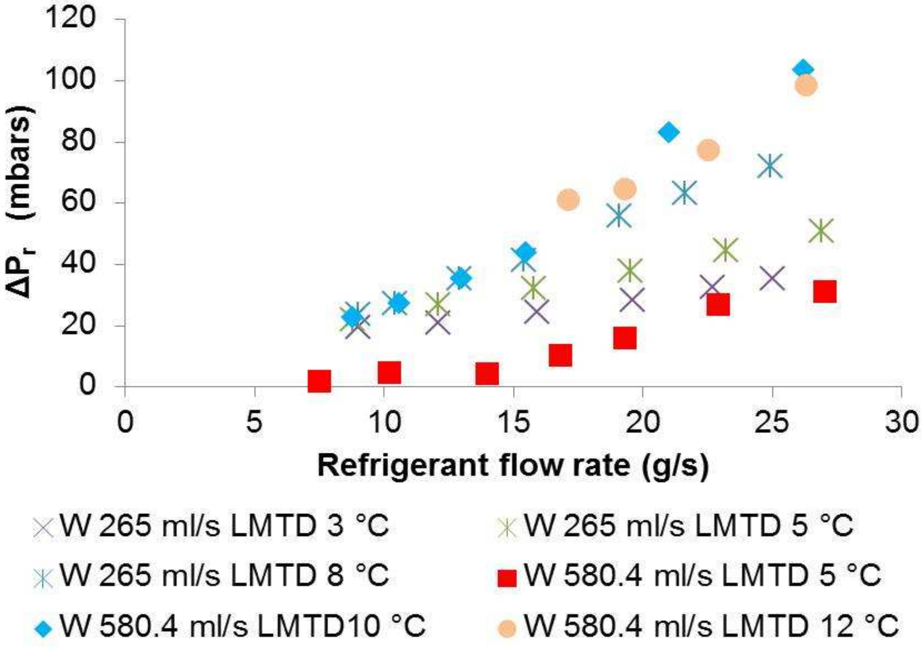

Figure 6-22: Refrigerant-side pressure drop variation with refrigerant flow rate

As shown in Figure 6-23, the overall heat transfer (U) coefficient value increases with increase in water mass flow rate until it levels off at a mass flow rate of about 580.4 ml/s where it attains a heat transfer coefficient of 10,000 W/m^2-K. With further increase in mass flow rate of water only modest improvement in the heat transfer coefficient was observed. Since the overall heat transfer coefficient is the harmonic sum of individuals, it would slowly asymptote towards the refrigerant-side heat transfer coefficient. For lower LMTDs, the overall coefficient is lower due to lower cooling capacity and heat flux.

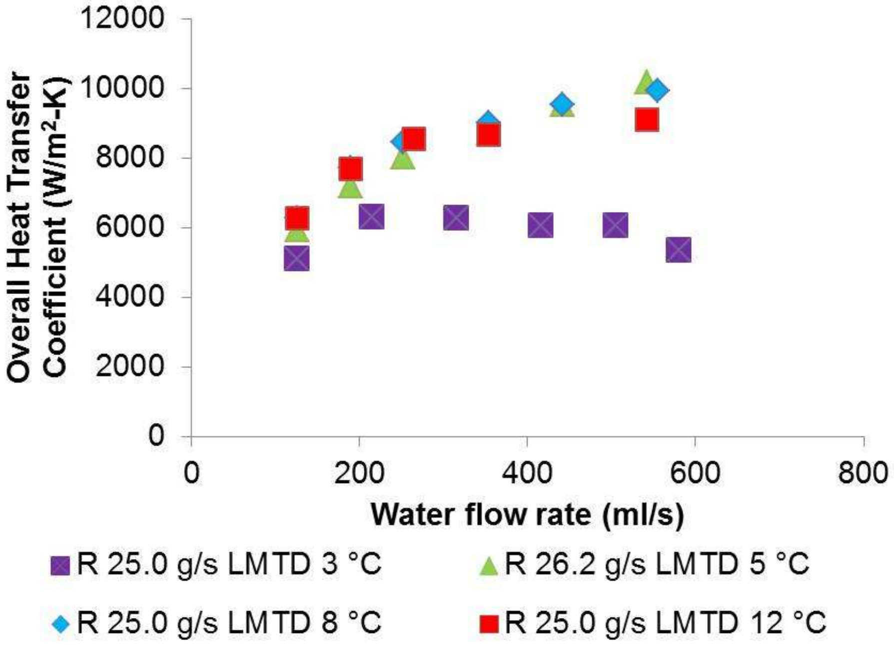

Figure 6-23: Overall heat transfer coefficient variation with water mass flow rate

Refrigerant-side heat transfer coefficient with increasing refrigerant mass flow in both the superheated and saturated regions is shown in Figure 6-24. Due to the dominance of forced convection and possible maldistribution, heat transfer coefficient doesn’t increase significantly in the saturated region. It does seem to asymptote as water-side heat transfer coefficient levels off. Heat transfer coefficient was observed to drop for higher vapor quality. It was not feasible to take data at low quality, as there was no way to directly control the heat transfer rate/heat flux for the system. It can be observed that overall heat transfer coefficient dropped by more than 20% despite using finer microchannels on the refrigerant-side. This was because the triangular grooves were not of same size and had larger dimensions (1.00 mm x 1.17mm) owing to larger hydraulic diameters. Hence, the water-side heat transfer coefficient was lower compared to earlier Al-assemblies. The improvement of the refrigerant-side heat transfer coefficient is described in next section.

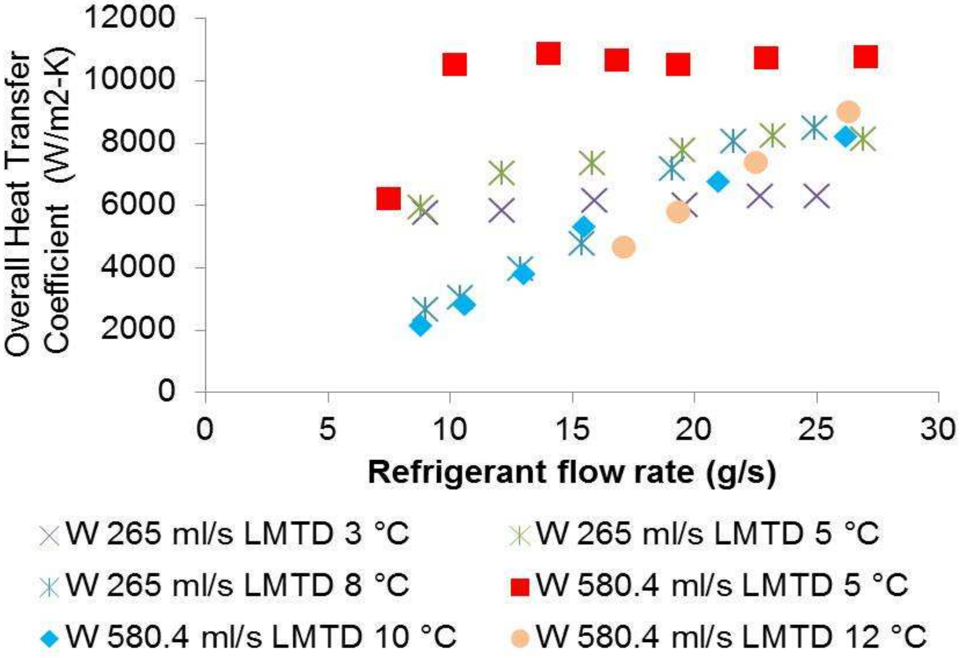

Figure 6-24: Overall heat transfer coefficient variation with refrigerant flow rate

6.2.2 Tube Insert Enhancement on water-side – Assembly 4

Microgroove manufacturability on the inner side of the HX tube was not feasible. Manifold geometry with bigger channel size doesn’t have huge advantage and hence an alternate header design approach was explored in form of tube inserts. Tube insert involves a coaxial PVC plastic insert to utilize the fins in the form of surface roughness. The distance between the inner tube surface and inner fin is close to d = 2.5 mm which is half of the hydraulic diameter of the water-side flow. A schematic of the tube insert is shown in Figure 6-25.

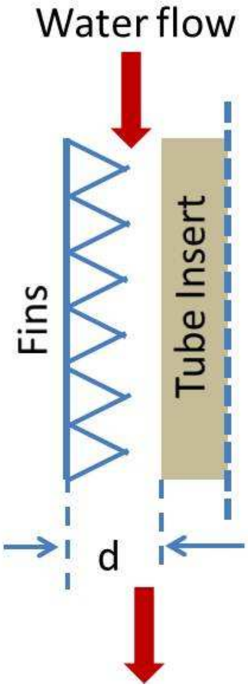

Figure 6-25 : Schematic of tube insert as water-side enhancement

Cooling capacity close to 4.5 kW was obtained at the highest water flow rate of 530 ml/s with a LMTD of 9 °C, as shown in Figure 6-26. A maximum water-side pressure drop of 100 mbars was observed at 530 ml/s, and maximum refrigerant-side pressure drop of 85 mbar was observed at 25 g/s. With increasing flow rate, cooling capacity increases linearly and starts asymptoting at higher water flow rate, as shown in Figure 6-27.

In comparison to the manifold header design, much higher numbers were obtained both in terms of cooling capacity and overall heat transfer coefficient. More than 20,000 W/m^2-K overall heat transfer coefficient was obtained for a refrigerant flow rate of 20 g/s at an LMTD of 4 °C as shown in Figure 6-28.

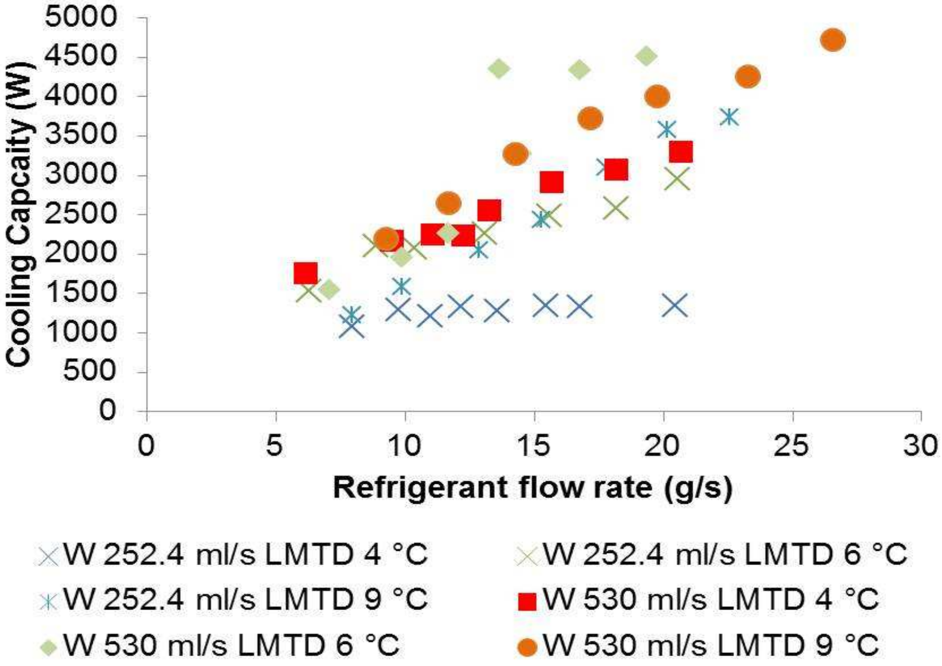

Figure 6-26: Cooling capacity variation with refrigerant flow rate for constant water mass flux

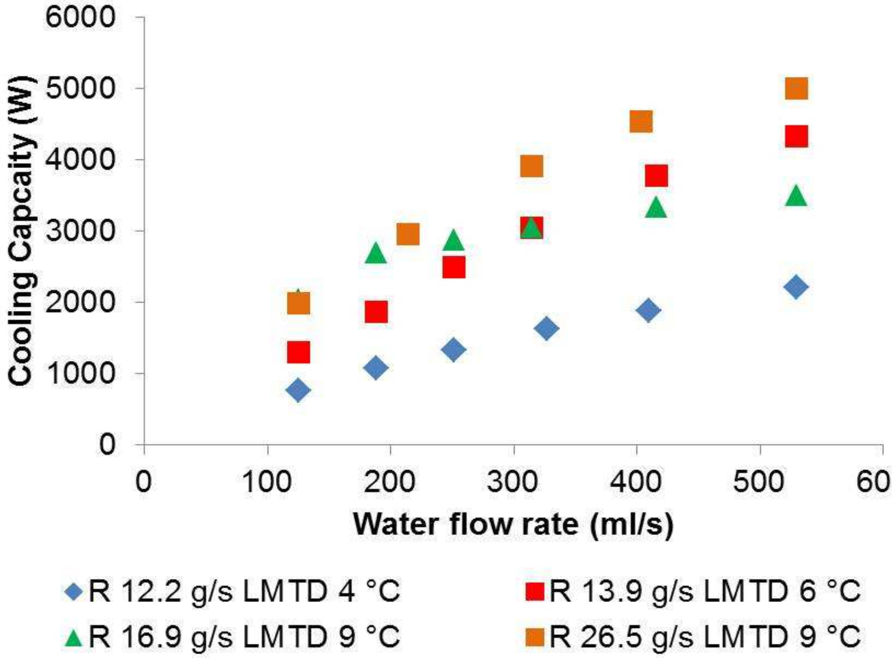

Figure 6-27: Cooling capacity variation with water flow rate

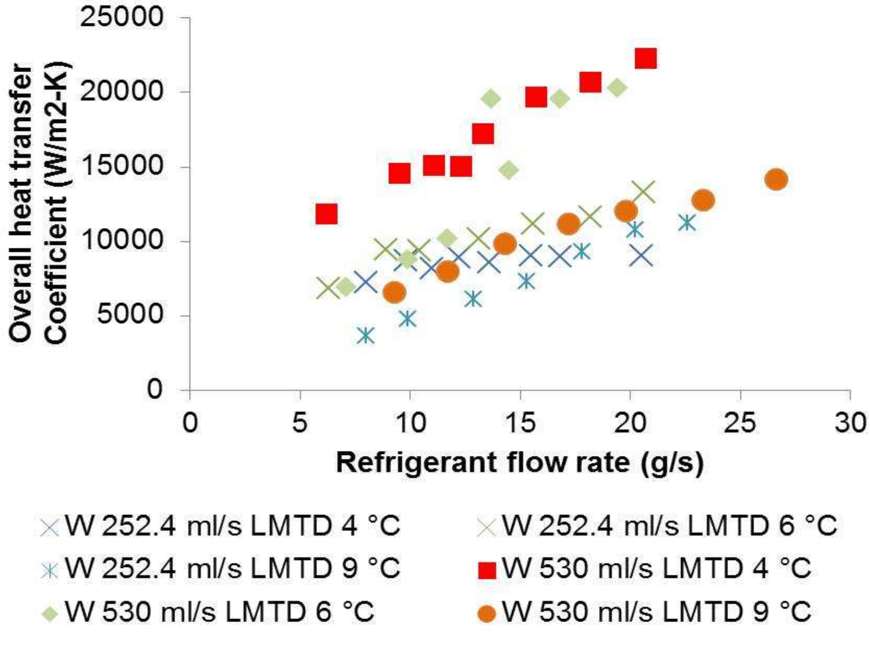

Figure 6-28: Overall heat transfer coefficient variation with refrigeration flow rate

Figure 6-29 shows the overall and individual water-side and refrigerant-side heat transfer coefficients. Water-side heat transfer coefficient was evaluated through the numerical simulation method for annular flow using ANSYS IcePAK. Refrigerant-side heat transfer coefficient was evaluated using the thermal resistance formula. Very high refrigerant-side heat transfer coefficient close to 140,000 W/m^2-K was seen at the refrigerant flow rate close to 17 g/s.

The pressure drops for both refrigerant-side and water-side is evaluated and were less than force-fed manifold design as shown in Figure 6-30 & Figure 6-31, respectively. An almost linear trend was observed on the refrigerant-side with a maximum pressure drop of 84 mbars at 26.6 g/s. Maximum water-side pressure drop was 110 mbars at 530 ml/s water mass flow rate.

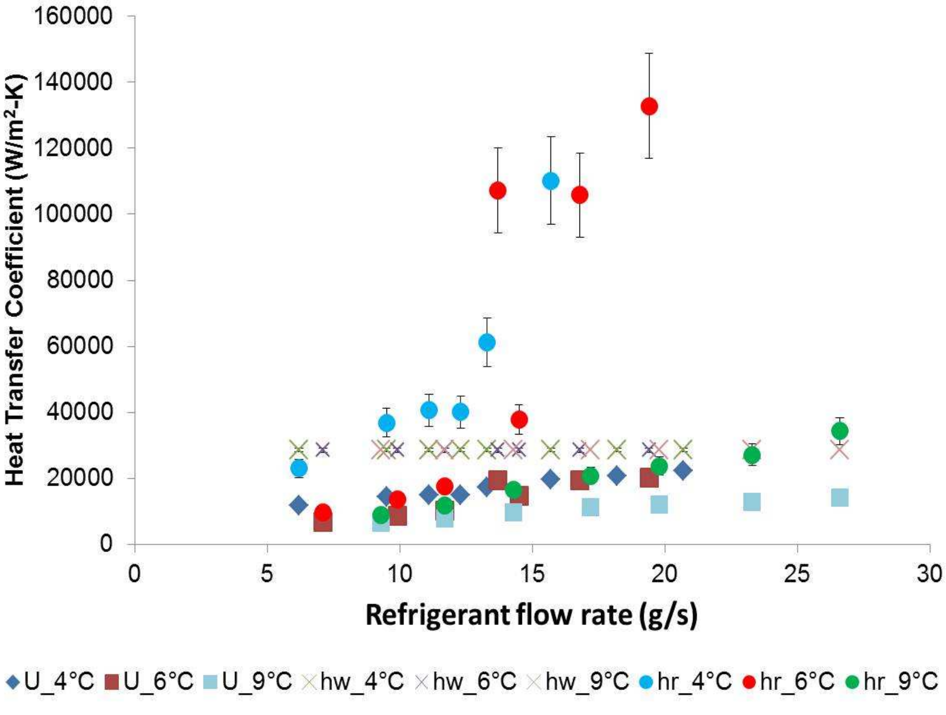

Figure 6-29: Heat transfer coefficient variation with refrigerant flow rate

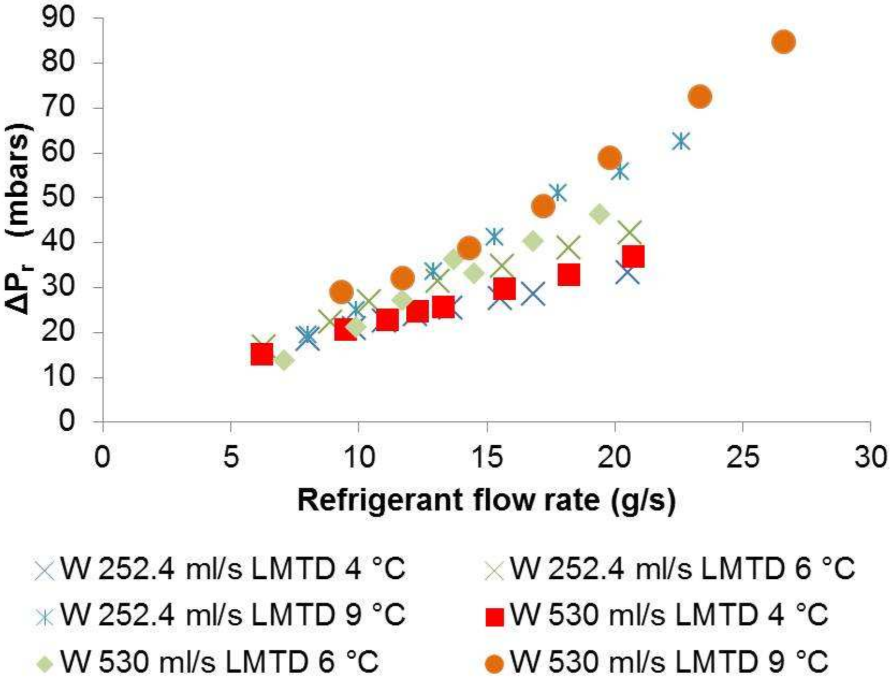

Figure 6-30: Refrigeration side pressure drop variation with refrigerant-side flow rate

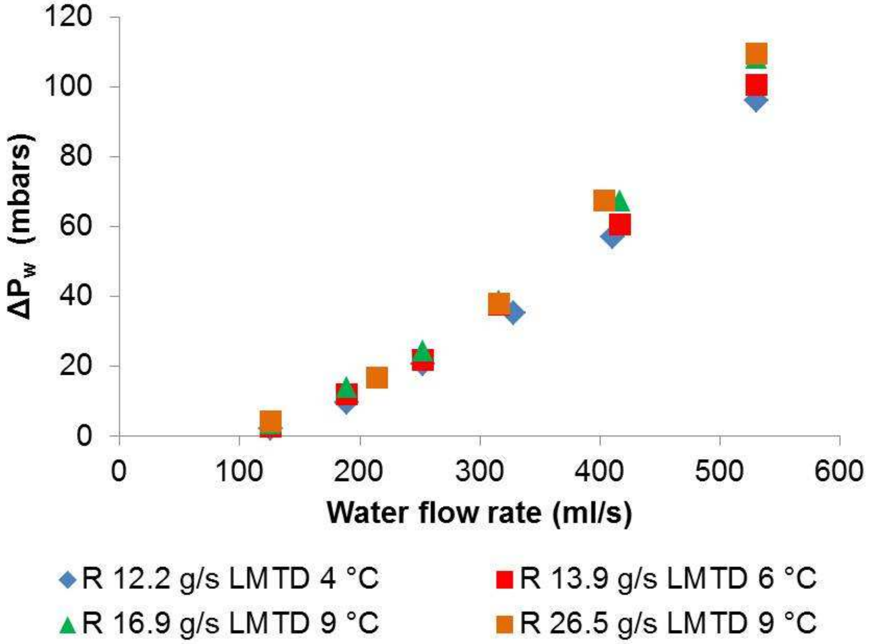

Figure 6-31: Water-side pressure drop variation with water-side flow rate

To summarizer this section for the new aluminum microgroove tube with both side headers, the following conclusions can be made:

- With the manifold header, overall heat transfer coefficients of more than 10,000 W/m^2-K were found for an LMTD of 4.7 °C. With the tube insert, more than 20,000 W/m^2-K overall heat transfer coefficient was obtained with an LMTD of 4 °C.
- With the manifold header, cooling capacity close to 4.0 kW was obtained with LMTD of 12 °C. With the tube insert, close to 5.0 kW cooling capacity was obtained using a LMTD of 9 °C.
- With the manifold header, the maximum pressure drop of 140 mbars at 580 ml/s was found on water-side and 100 mbars at 26g/s was found on refrigerant-side. With the tube insert, the maximum pressure drop of 110 mbar at 530 ml/s was found on the water-side and 85 mbar at 26 g/s on the refrigerant-side.

6.2.3 Aluminum tube corrosion and new microgroove material selection

With continued testing of the aluminum tube microgroove evaporator over a period of time, it was observed that cooling capacity decreased and the water-side pressure drop increased. The evaporator test section was disassembled, and massive corrosion was detected on the aluminum channels despite the fact that the appropriate amount of corrosion inhibitor was used. The oxides were blocking the grooves on the water-side, which was leading to pressure drop increase. Because the full surface area could not be used for heat transfer, cooling capacity was decreasing.

One of the major motivations behind the design was to reduce the weight and size of heat exchangers with easy manufacturability. Aluminum has a lower density and lower cost in comparison to other commonly used materials. It is also easy to deform and hence is easier to manufacture. There has been a significant amount of research done to study the compatibility of different aluminum alloys like 6061, 6063 and 7075, etc. for design of heat exchangers. According to aluminum association guidelines for aluminum structures, the metal remains largely corrosion resistant unless exposed to some substance or condition which can destroy the protective oxide coating. Aluminum is highly resistant to weathering, even in many industrial atmospheres, which often corrode other metals. It is also resistant to many acids [68].

According to the US army corps of engineers, an aluminum protective oxide film is generally stable in the pH range of 4.5-8.5, but the nature of compounds present can be crucial [69].

The preliminary material selection for design of the heat exchanger was aluminum 6061 alloy, as 6061 and 6063 alloys have higher strength and corrosion resistance. However, due to the presence of foreign corrosion chemicals in the process fluid, corrosion can occur, which can be further tackled by anodization or cathodic protection. Anodization is the common process used to increase aluminum corrosion resistance by artificially increasing the thickness of the oxide layer. Salt water typically does not corrode aluminum, as its pH is neutral. However, it can be a major facilitator for galvanic corrosion. As aluminum 6061 has a lower number in the galvanic table, it would corrode preferentially in presence of dissimilar metals.

The preliminary design of the evaporator was done with aluminum 6061 alloy based on the suggestion in the literature for its compatibility. However, massive corrosion was found on the water-side minichannels despite using 1g/L of corrosion inhibitor (potassium silicate). The aluminum oxides eventually blocked a significant number of channels, which led to a decrease in heat transfer rate and increase in overall pressure drop. The corroded water-side surface is shown below in Figure 6-32.

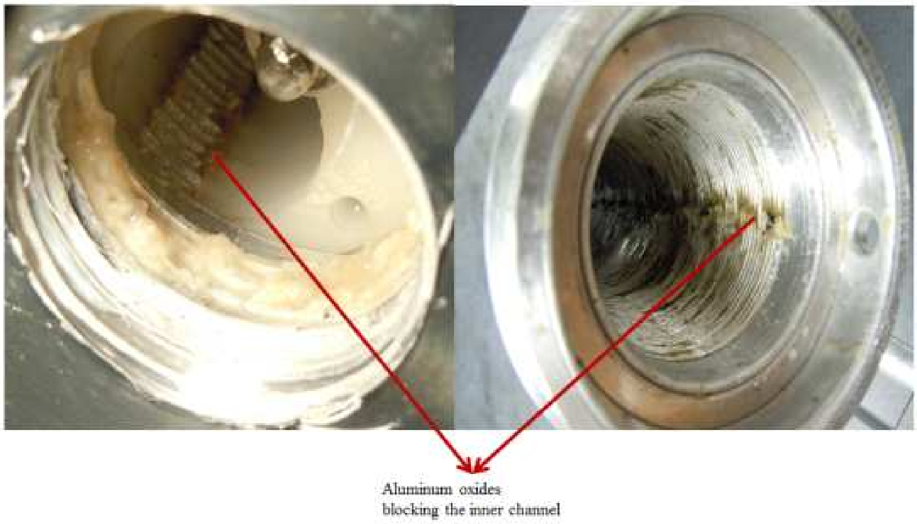

Figure 6-32: Corroded aluminum HX surface on water-side

A different concentration of corrosion inhibitor was tested to address the issue, but the problem remained. As suggested in the literature, anodization was seen as a possible solution to arrest the issue. But it was quite challenging to anodize only one side of the surface when the other side of the surface has finer microchannels (<100 µm). A special assembly had to be prepared to completely seal the outer surface from any damage, as highly corrosive sulfuric acid solution is used for the anodizing process. An image of the anodized tube is shown below in Figure 6-33.

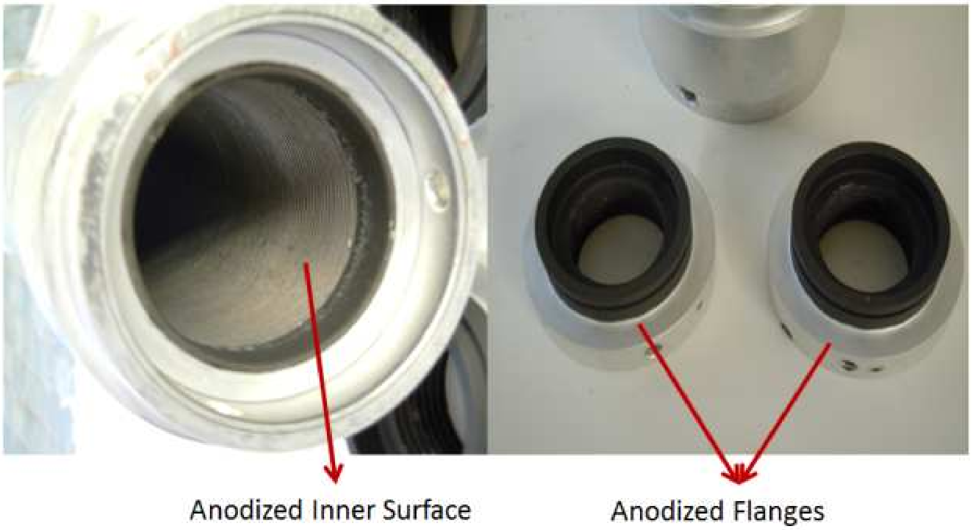

Figure 6-33: Anodized water contacting parts of tubular heat exchanger

Numerous tests with R134a as the working fluid were conducted using the anodized tube, and satisfactory results were obtained. Further corrosion testing was done by totally submerging the evaporator test section in an ammonia water solution. This resulted in massive corrosion similar to that observed on the outer shell. As the complete assembly was dipped in the solution, corrosion was observed on the entire surface that was unprotected, including the refrigerant-side. Corroded parts from ammonia water solution at the ammonia test facility are shown below in Figure 6-34. It was also indicated that the epoxy glue used in the assembly became soft and had the potential to disintegrate due to the ammonia.

Figure 6-34: Corrosion from ammonia water solution at ammonia test facility

A compatibility test of different materials for the evaporator test section was done with the ammonia water solution. The samples of materials were kept in the ammonia water solution for months and no appreciable corrosion was found. The concentration of ammonia water solution was increased by saturating it with gaseous ammonia; however, it did not visibly affect the results. Figure 6-35 and Figure 6-36 show the sample materials tested with the ammonia-water solution before and after testing.

Figure 6-35: Samples of heat exchanger materials before water-ammonia solution compatibility testing

Figure 6-36: Same materials after submerging in the ammonia –water solution for 4 months

Though contradictory results were obtained from in-house tests, it was safer to look for alternative material for the HX surface which has higher corrosion resistance.

Nickel 200 alloy was found to be suitable in terms of chemical compatibility, but the downside was lower thermal conductivity (~ 90 W/m-K) and higher density (~ 8908 Kg/m^3) compared to aluminum alloys. Also, nickel alloy is a tough material choice for manufacturability purposes. Nickel's Brinells hardness number is 700 MPa in comparison to 245 Mpa for aluminum. Also, nickel alloy has tendency to stick to the fabricating tool, resulting in the operation failure and fins destruction. It took significant time to select a proper combination of tool, lubrication and cutting regimes before the nickel microgroove tubes fabrication were fabricated. The fabrication cost was significantly higher compared to aluminum tubes. The fabricated nickel microgroove tube of 100 µm X 600 µm size is shown below in Figure 6-37.

Figure 6-37: Nickel high aspect ratio microgroove tube

6.3 Nickel microgroove tube results – Assembly 5 & 6

This section discusses the results for the nickel microgroove surface having 100 µm X 600 µm channel size and 2mm x 2mm manifold on the refrigerant-side. The water-side geometry had the same size as the new aluminum tube discussed in last section. As discussed in earlier sections, the aluminum tube gave good results in terms of cooling capacity and overall heat transfer coefficient. With the use of finer channels and higher aspect ratio, overall heat transfer coefficient increases for the same cooling capacity. Also, with use of bigger manifolds, pressure drop was modest even for higher flow rates. However, due to corrosion issues, the nickel microgroove tube had to be fabricated for better corrosion resistance both on the water and refrigerant side. Since nickel has lower thermal conductivity compared to aluminum, higher thermal resistance was expected. But the tube insert on the water-side compensated for lower conductivity by enhancing the water-side heat transfer coefficient. The tube insert helped in maintaining the smaller hydraulic diameter of the flow. The flow is mostly turbulent at higher Reynolds number as the flow surface was finned. This section discusses the results associated with different flow arrangements – co-current and counter flow. As the flow on the refrigerant-side is complex, the header entry plays an important role in refrigerant distribution and hence can affect the refrigerant-side heat transfer coefficient. It was observed that when refrigerant flows against gravity, better results are obtained compared to refrigerant flowing with gravity. Water-side flow configuration does not affect the results significantly in terms of cooling capacity. But, some localized difference in temperature makes the heat flux non-uniform which ultimately affects the refrigerant-side heat transfer coefficient.

Tube inserts with two different hydraulic diameters, 5 mm and 3 mm were tested. The desired nickel surface channel width was 30 µm (channel width) x 300 µm (channel height) but due to difficult manufacturability issues, these dimensions could not be obtained. The actual nickel surface had a channel width of 100 µm, fin width of 200 µm and channel depth of 600 µm which was significantly different from the requirement. The effect of this was highly visible in the results, as the overall heat transfer coefficient almost was cut by half. The water-side grooves were much rougher than the earlier aluminum tube fabrication, but they led to similar pressure drop curve. So, it is hypothesized that water-side heat transfer coefficient was not significantly affected. The major contributor to the lower than expected overall heat transfer coefficient is the refrigerant-side surface where fin wall occupies almost 66% of the heat transfer surface. The new aluminum tube (60µm x 600µm) provided twice the overall heat transfer coefficient compared to this tube.

Figure 6-38 shows the cooling capacity variation with varying refrigerant mass flow rate. The data is shown for both the insert tubes (Tube A & Tube B for same the microgroove surface) – one with larger and one with smaller annular gaps; which basically provides different hydraulic diameters. The data are divided in two parts: one for lower refrigerant mass flow rates (< 15 g/s) which typically falls into the superheat zone and the other in the saturated zone with higher mass flow rates. It was observed that at higher mass flow rate, the curve for lower hydraulic diameter catches up with the higher hydraulic diameter and essentially leads to similar results. The TubeB data have lesser cooling capacity when compared to TubeA data, as it was not feasible to run the test at higher mass flow rate due to water-side pressure drop limits.

For an LMTD of 5 °C, it can be seen that, cooling capacity flattens out due to water-side heat transfer coefficient limitation. This was a common trend with all smaller LMTD data. As the LMTD increases; the curve shifts up, which leads to higher cooling capacity. There is no significant difference for data corresponding to different flow arrangement. For all the cases, parallel flow has both refrigerant and water flowing against gravity. For counter flow, refrigerant is flowing against gravity, but water is flowing towards gravity. Typically for two-phase heat exchangers, flow arrangement should not affect the results, but gravity can affect the flow distribution inside the manifolds.

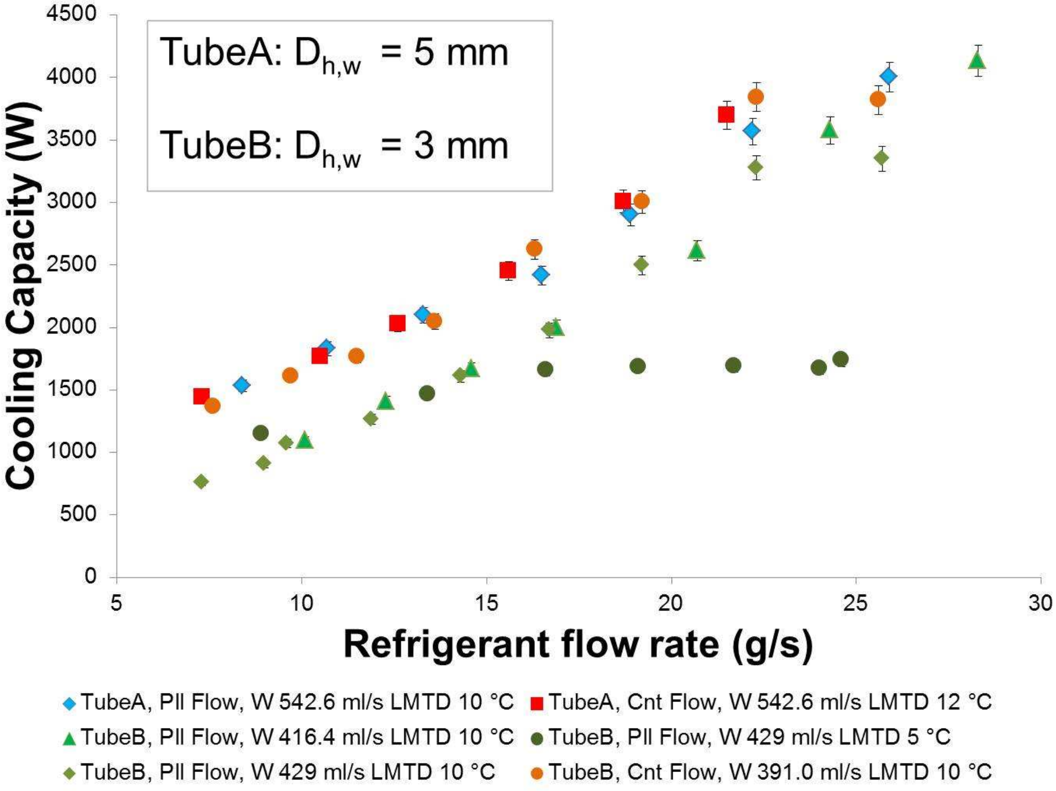

Figure 6-38: Cooling capacity variation with refrigerant mass flow rate at constant water mass flow rate

Cooling capacity variation with water flow rate increases linearly and asymptotes to a higher value as the refrigerant-side heat transfer coefficient limit is reached as shown in Figure 6-39. There is no significant difference found due to flow arrangement. With increasing LMTD, it is seen that the curve shifts to the top as expected showing higher cooling capacity.

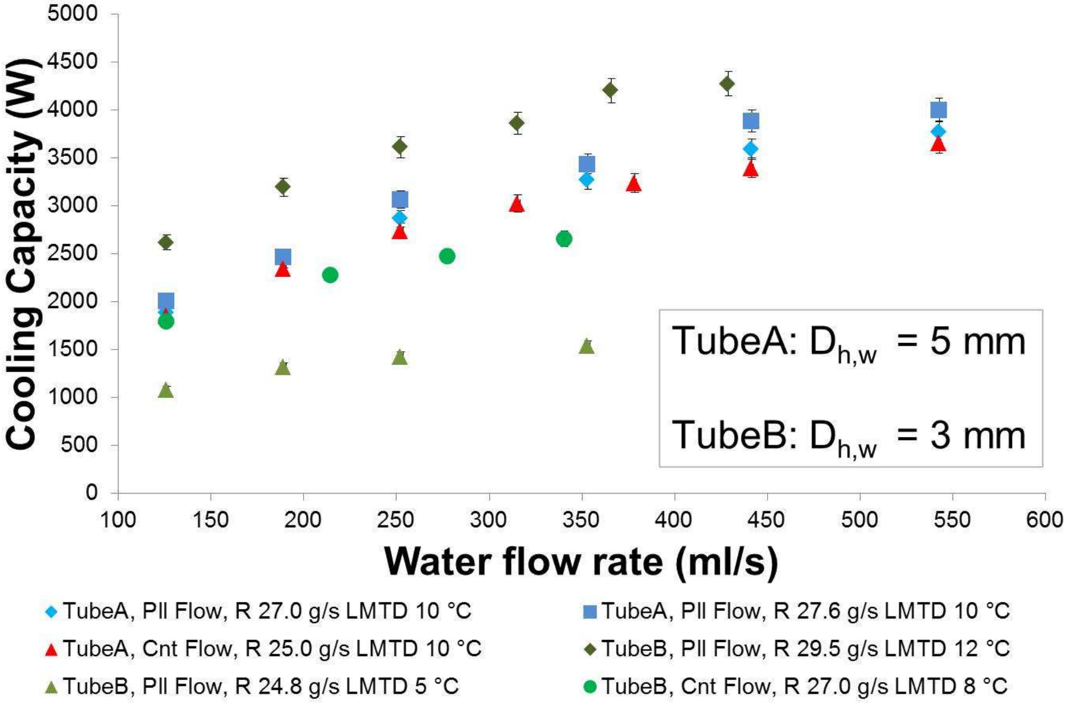

Figure 6-39: Cooling capacity variation with water mass flow rate at constant refrigerant mass flow rate

Figure 6-40 shows the overall heat transfer coefficient with varying refrigerant flow rate, which has a similar trend compared to the cooling capacity data. A maximum value of 10,800 W/m^2-K was achieved with cooling capacity close to 4 kW for an LMTD of 10 °C. There is a linear increase with mass flow rate because the convective heat transfer is dominant mechanism in the data studied. As the limit of coefficient is reached on other side, the graph flattens out due to the harmonic sum relation, which basically pulls the data to the lower value.

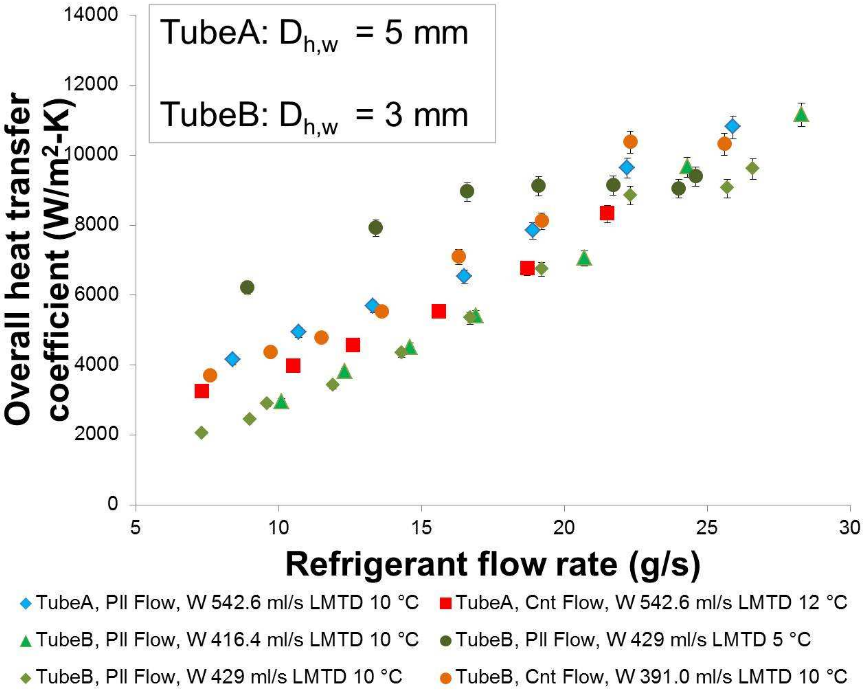

Figure 6-40: Overall heat transfer variation with refrigerant mass flow rate at constant water mass flow rate

The pressure drop data was also observed for both refrigerant and water-side, as shown in Figure 6-41 and Figure 6-42, respectively. The refrigerant-side pressure drop increases linearly in the data studied, and a maximum of 120 mbars was obtained at mass flow rate of 27.6 g/s. The water-side pressure drop curve increased with power law, and a more significant pressure drop was observed for insert Tube B compared to Tube A. Close to 350 mbars was reached at the lower water-side mass flow rate, and it was not feasible to test for more cooling capacity. Maximum water-side pressure drop close to 97 mbars was obtained at 540 ml/s for the Tube A insert. Based on the comparison, Tube A insert was chosen as the final design choice, as the pressure drop for the insert was significantly lower without any noticeable change in cooling capacity.

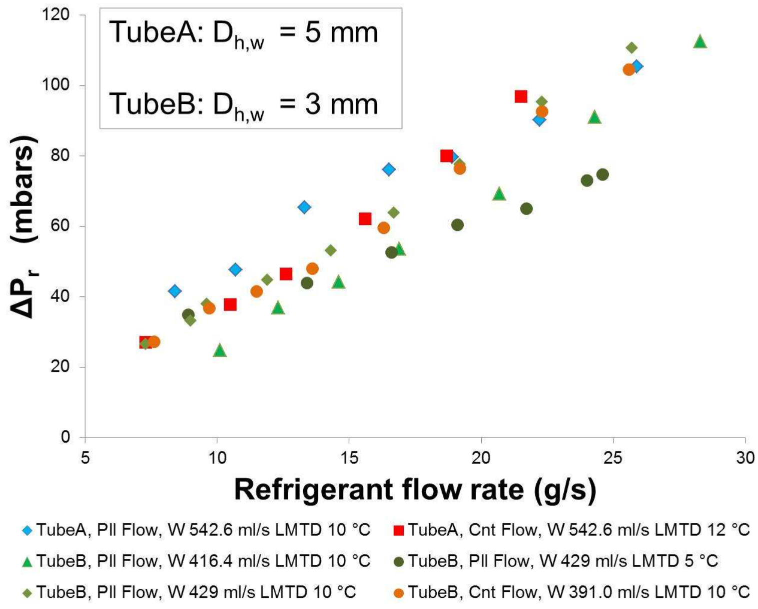

Figure 6-41: Pressure drop variation with increasing refrigerant mass flow rate

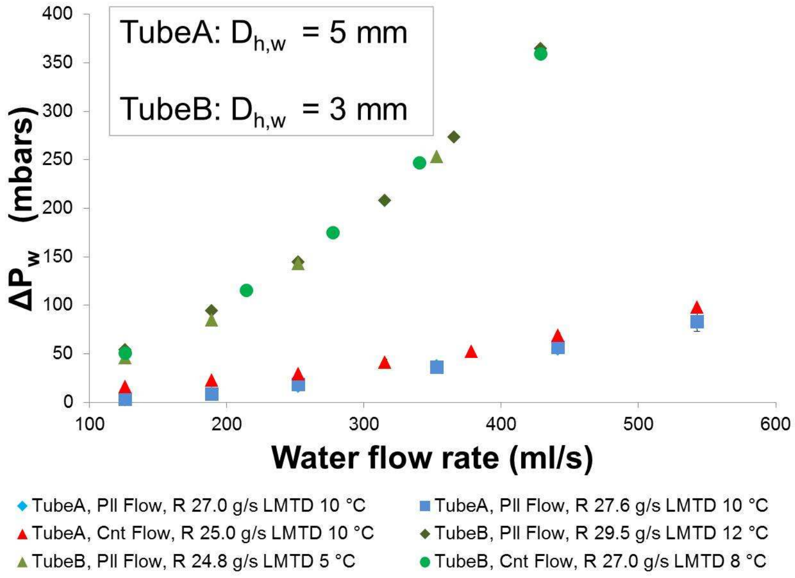

Figure 6-42: Pressure drop variation with increasing water mass flow rate

Overall heat transfer coefficient was cut by half due to poor surface availability on the microgroove outer side. A single-phase analysis was done for the actual geometry, which showed that base heat transfer coefficient is cut to close to half compared to the required surface with same manifold mass flux. However, 4 kW cooling capacity was achieved using higher LMTD which provided a good basis for testing with ammonia as refrigerant.

A numerical study was carried out to evaluate the water-side heat transfer coefficient, and further refrigerant-side heat transfer coefficient is evaluated using thermal resistance equation. Variations of individual and overall heat transfer coefficients for parallel flow with refrigerant mass flow rate of 27.0 g/s are shown in Figure 6-45. A comparison of pressure drop for both numerical and experimental was performed, as shown in Figure 6-45 and the trend is in close agreement. The numerical analysis ignores the manifold pressure drop, which explains the absolute difference.

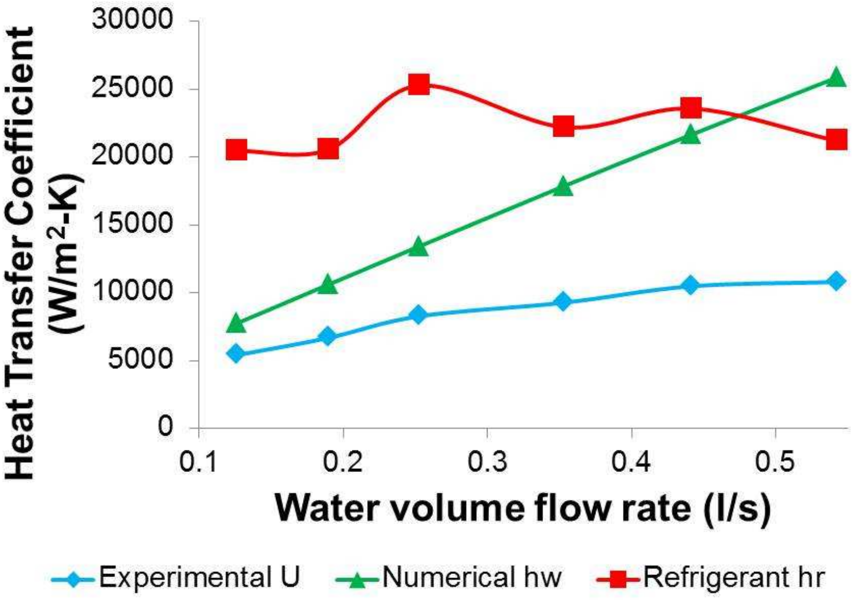

Figure 6-43: Variation of heat transfer coefficient vs. water mass flow rate

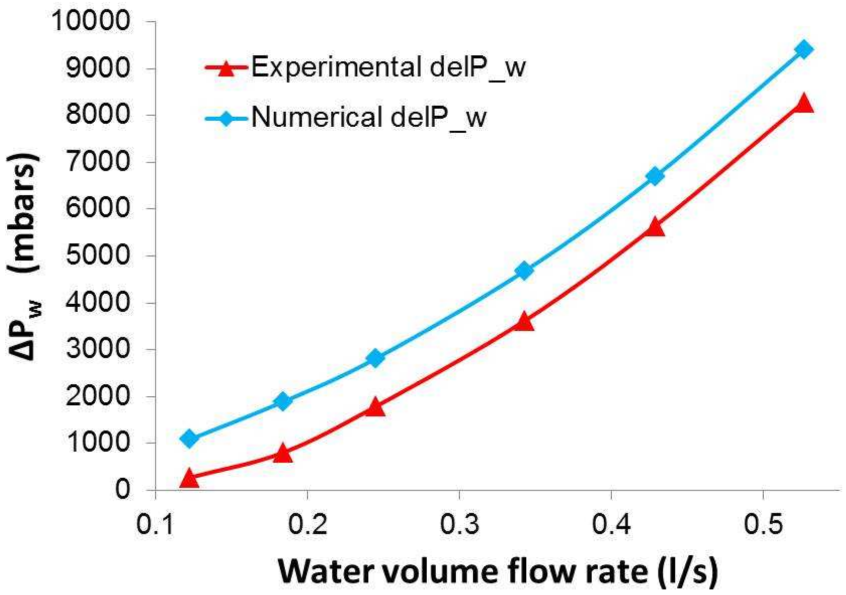

Figure 6-44: Variation of water-side pressure drop with water volume flow rate

Further a test was conducted using Assembly 5 with varying LMTDs to observe the variation of vapor quality with overall heat transfer coefficient as shown in Figure 6-45. It can be observed that for lower refrigerant mass flow rates, the graphs shifts to the bottom and the peak is obtained at higher vapor quality. With vapor dryout conditions in the channel, heat transfer coefficient significantly drops , agreeing well with Cetegen's results [31] and other flow boiling empirical literature data cited in earlier sections. Change in vapor quality is obtained by varying the LMTD as the mass fluxes on both sides are constant. For lower quality, the data are convection driven with influence of thin-film evaporation obtained for high aspect ratio microchannels. A visualization study would have been more beneficial to study the flow regime inside these channels. But as the system is non-intrusive and operates at high pressure, it was not feasible to conduct such a study.

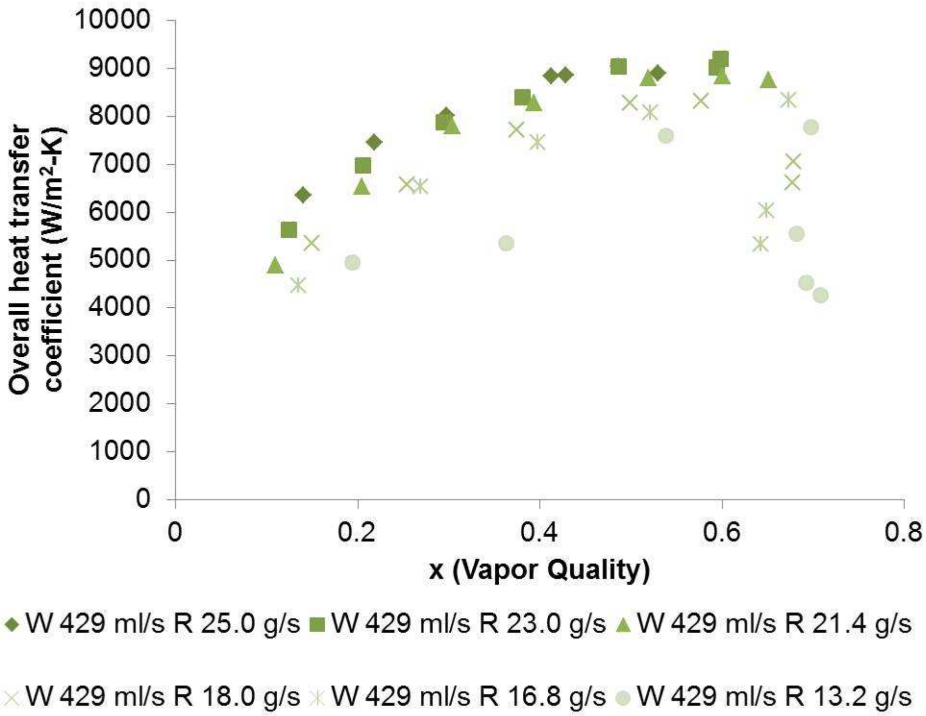

Figure 6-45: Variation of overall heat transfer coefficient with vapor quality at different refrigerant mass flow rate

To obtain a fair estimate of the flow regime, an analysis was performed using criteria given by the recent investigation, by Harirchian & Garimella [70], which is a comprehensive study of flow boiling in microchannels. In this study, experiments were conducted to determine the effects of important geometrical parameters such as fin width, channel width and cross-sectional area, mass flux, heat flux, vapor quality and fluid properties on flow regimes, heat transfer coefficients and pressure drop in microchannels. A detailed flow regime map was prepared, and a quantitative criterion was determined in terms of Boiling and Bond number for transition from macro to micro scale.

Detailed calculations are shown to map the currently obtained data based on these criteria. The calculations clearly suggest that the flow for the existing data set fall under heavily confined flow and a strictly annular region. For very smaller channels, the thin-film evaporation process would dominate the flow regime and will contribute to a higher heat transfer coefficient despite having low mass and heat fluxes.

$$G = \rho v \text{ "}Massflux\text{"}; \qquad \mathrm{Re} = \frac{GD_h}{\mu} \text{ "}\mathrm{Re}\, ynold\text{'}s\, number\text{"}$$

$$Bo = \frac{g(\rho_f - \rho_g)D_h^2}{\sigma} \text{ "}Bond \;\; number\text{"}; \quad Bl = \frac{q_w^{''}}{(Gh_{fg})} \text{ "}Boiling \;\; number\text{"}$$

$$\mathrm{Re}\; frigerant \;\; side \;\; calculatio\; ns:$$

$$Channel \;\; Width \;\; w_c = 100\ \mu m; Channel \;\; Height \;\; t_f = 600\ \mu m;$$

$$Fin \;\; Width = 200\,\mu m$$

$$D_h = 4A/P = (2*100*600*1e-6)/(100+600) = 171.43\,\mu m$$

$$D_h = \sqrt{A} = \sqrt{30*300*1e-12} = 244.95\,\mu m \;\; (U \sin g \;\; other \;\; criteria)$$

$$A_{cs} = 100*600*1e-12 = 6e-8\,m^2$$

$$N_{man} = 20 \qquad Nmicro = 254/((100+200)*1e-3) = 847$$

$$G = \dot{m}_w/(2*Nman*Nmicro*Acs) \sim 12.3\,kg/m2-s \;\; for \; \dot{m}_w = 25\,g/s$$

$$\mathrm{Re} = (12.3*245*1e-6)/0.0001949 = 15.4618$$

$$Bo = 9.81*(1280-32.1)*245\wedge 2*1e-12/0.008081 = 0.0909$$

(6-2)

$$q_b^{''} = 80{,}000 \;\; W/m^2 - K \qquad q_w^{''} = 80{,}000/6 = 13333\; W/m2-K$$

$$Bl = 80{,}00/(17.36*188*1000) = 0.0058$$

$$Bo\wedge 0.5*\mathrm{Re} = 4.6617 \ll 160 \;--> Heavily \;\; confined \;\; flow \;--> Annular$$

$$Bl > 0.017*(Bo\wedge 0.4*\mathrm{Re}\wedge -0.3) = 0.0029 \;--> \; vapor \;\; bubble \;\; coalesce$$

The next section would briefly discuss developmental effort for flat plate evaporator design and its fabrication.

6.4 Flat evaporator design and fabrication

Based on the previous development and study, it was determined that overall heat transfer coefficient is limited due to manufacturing limitations on the inner side of the tube. A different approach for enhancing the water-side heat transfer coefficient was studied, but it cannot compete with the benefits of microgrooves to enhance the surface. Hence, an alternative approach was tried by switching to a flat plate design, where it was feasible to make microgrooves on both sides. The design philosophy is similar to traditional plate heat exchangers with the exception of microgroove surface and the use of manifolds for distributing the flow. The O-ring seals were used on alternative plates to divide the flow stream, and multiple plates were stacked together to achieve the desired cooling capacity. Some of the latest existing latest literature is provided for further study on the plate heat exchanger for absorption chillers which serves as a guideline for the current design [71-78].

The scope of this section is limited to introducing the design and fabrication, as preliminary experimental testing is still ongoing and is continuing as future developmental effort. It is expected that with the use of finer high aspect ratio grooves on both sides of the plates, much better (> 50,000 W/m^2-K) than the current overall heat transfer coefficient can be achieved. This has a tremendous potential for design of two-phase heat exchangers such as evaporators and condensers and single-phase solution heat exchanger.

The flat plate heat exchanger was designed to achieve 20 kW using several flat high aspect ratio nickel 200 alloy microgroove plates for a counter flow LMTD of 5 °C. The microgroove geometry selection was based on single-phase study of manifold design. After several iterations, the following design parameters were chosen based on achieved heat transfer coefficient and pressure drop values.

$$\begin{gathered}
Base\ Surface: Ni-Pure;\quad Fluid: Water \\
H_{base,micr} = 0.1\ mm;\quad q'' = 50{,}000\ W/m^2;\quad \dot{m} = 2e-6\ kg/s; \\
w_{ch,micr} = 0.03\ mm;\quad t_{fin,micr} = 0.03\ mm; \\
H_{fin,man} = 0.5\ mm;\quad H_{fin,micr} = 0.2864\ mm; \\
W_{ch,man\_inlet} = 0.5\ mm;\quad t_{fin,man} = 0.5\ mm;\quad W_{ch,man\_outlet} = 0.5\ mm; \\
h = 161700\ W/m^2-K;\quad \Delta P = 60\, mbars
\end{gathered} \tag{6-3}$$

Based on the above results, overall heat transfer coefficient can be calculated using first order thermal resistance formula given by:

$$\frac{1}{U} = \frac{1}{h_{base,side1}} + \frac{L}{k_{base}} + \frac{1}{h_{base,side2}} \tag{6-4}$$

Taking L = 2 mm and k_{base} = 90 W/m-K, U ~ 28865 W/m^2-K.

Further, the required heat exchange area is calculated using:

$$A = \frac{Q}{UxLMTD} = \frac{20e3}{28865x5} = 0.1386\, m^2 \tag{6-5}$$

It was desired to keep a compact design having roughly the same size as a conventional plate HX. Also, as the solution heat exchanger operates under much higher system pressure (~ 500 psi), the larger area would be susceptible to uneven stresses. So, multiple plates have to be stacked together to achieve the total cooling capacity. It was also important to check the deformation from the support of the inlet and outlet. As O-rings are providing the sealing, huge deformations near the contact area can cause the assembly to fail. A preliminary structural study was carried in ANSYS to find a feasible length to width ratio for the single plate, which led to the design parameters of 300 mm length and 60 mm height. Using this area, roughly eight plates would be required to achieve the cooling capacity target. Multiple flow passage is achieved using baffles on the manifolds, which would increase the flow length and pressure drop. But it would also lead to more mixing and reduction in thermal gradient.

The fabricated component for the assembly is shown below in Figure 6-46.

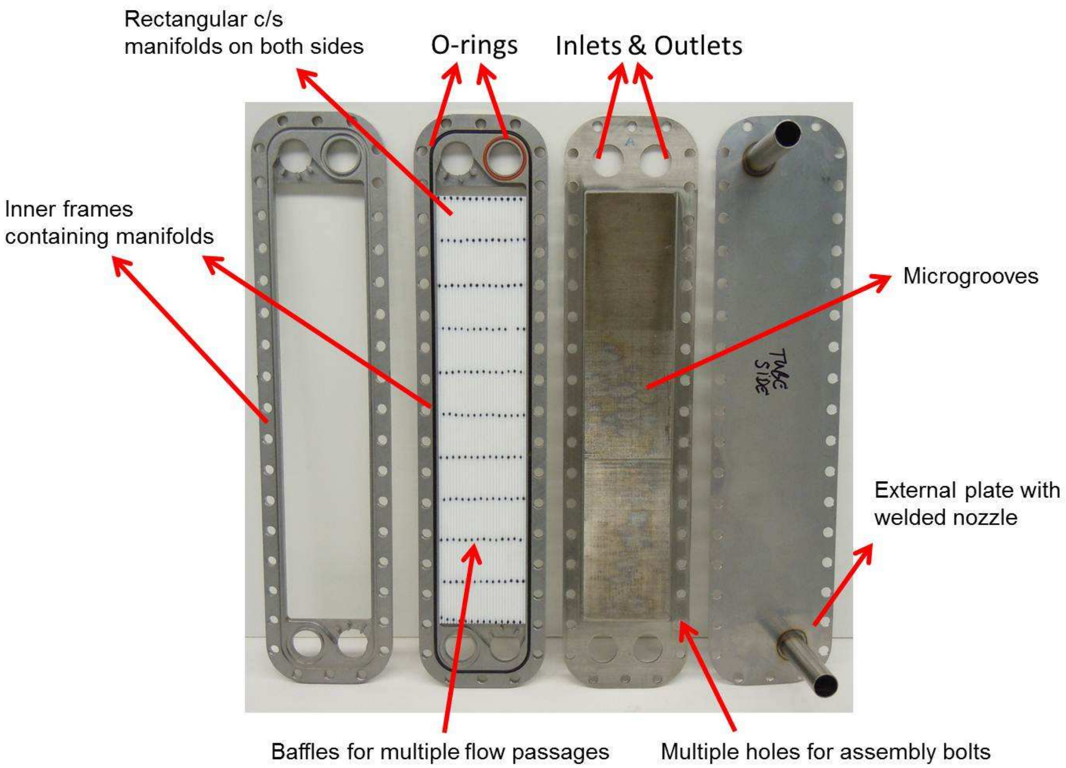

Figure 6-46: Flat SHX fabrication assembly

6.5 Summary

The tubular evaporator was tested for performance characterization with different flow configurations, microgroove materials, and microgroove geometry with header enhancements. The development basically progressed in phases building on the knowledge from earlier studies. The aluminum tube with more optimally designed evaporator surfaces (60 µm x 600 µm) yielded much better results in terms of heat transfer coefficient and pressure drop. Overall heat transfer coefficient more than 20,000 W/m^2-K was seen with a LMTD of 4 °C with tube insert enhancement. But due to corrosion issue, design was not sustainable for carrying out further studies. An alternative material based on nickel alloys was micro-machined to create the HX surface. Due to the difficult manufacturability, of nickel alloys, the desired surface features in terms of smaller channel width (30 μm) and higher aspect ratio (~10) were not achieved. Nevertheless, objective of more than 10,000 W/m^2-K overall heat transfer coefficient with more than 4 kW cooling capacity was achieved with a modest maximum pressure drop of 100 mbars on both water and refrigerant-side. Different header designs on the water-side were studied and it was concluded that the manifold design did not offer any specific benefit compared to the simple annular flow due to the manufacturing limitation to create optimum channel (groove) dimensions. The grooves hydraulic diameter obtained was in millimeter ranges, thus yielding heat transfer coefficients less than that achievable by microchannels. However, manifold design has significant advantage on the refrigerant-side leading to much higher refrigerant-side heat transfer coefficient despite low refrigerant-side mass and heat fluxes. The evaporator section was further tested with an ammonia/ethylene-glycol pair at an independent ammonia test loop facility, and similar results were obtained. Overall heat transfer coefficient values obtained from present study are significantly higher than the values for conventional plate evaporators present in literature. The test results demonstrate the applicability of the manifold microchannel concept for effective heat exchanger design with game - changing potential for the energy industry. The current development is also undergoing for flat evaporator with finer microgrooves on both sides of the plate. The fabrication has been completed and the experimental testing is underway. The next chapter would provide summary and conclusions for the whole thesis.

CHAPTER 7: CONCLUSIONS AND FUTURE WORK RECOMMENDATIONS

This chapter provides summary and conclusions highlighting the important findings and contributions of the current study. Recommendations for future work are also provided.

7.1 Summary and Conclusions

In this part of the study, a single-stage ammonia cycle simulation was conducted to identify the influence of important parameters of an absorption cycle on enhancement of the COP for an absorption refrigeration system. Critical parameters for the cycle design were identified and effects of these parameters were characterized. The following important conclusions were drawn:

a) Heat exchanger effectiveness heavily influences the cycle design and performance. COP of the cycle can be improved substantially by increasing the overall heat transfer coefficient of the heat exchangers.

b) The higher the evaporator exit temperature; the higher the COP of the cycle. However, this leads to higher system pressure drop penalty, thus a tradeoff in place and an optimum point exists for a given cycle.

c) Higher absorber and condenser exit temperature significantly decrease the COP of the cycle.

Based on the findings of the first part, a component level focus was put on enhancing the design of high performance evaporator for a waste heat activated absorption cycle. An innovative manifold microchannel with careful evaporative surface design and precise flow delivery and liquid/vapor management was designed, constructed, and experimentally characterized. The manifold design utilizes an efficient flow distribution header to reduce the pressure drop by an order of magnitude, when compared to conventional system for a given heat transfer coefficient. Due to better mixing of the flow, it enhances the heat transfer coefficient and helps in attaining uniform temperature distribution. Next, a single-phase study of manifold microchannel design was carried out to understand the effect of important geometrical and flow parameters and the following important conclusions are drawn:

a) Microchannel width significantly affects the fluid flow and heat transfer behavior and is a critical parameter for the design.
b) An optimum exists for both fin width and fin height/aspect ratio as the curve passes through a peak. This optimum is also dependent on mass flux.
c) Manifold geometrical dimensions (fin thickness, channel width and channel height) in general should be kept smaller to have better heat transfer coefficient and lower pressure drops.
d) Mass flux significantly affects the pressure drop and heat transfer rate in all the cases. The optimum points will change if mass flux is also considered a separate variable for the study. Higher mass would require larger channel width to reduce pressure drop in general.

Utilizing the above findings, a 5 kW cooling capacity tubular evaporator was successfully designed, fabricated, and tested to a pressure of 500 psi. Much higher overall heat transfer coefficients (U) were obtained when compared to the widely used state of the art plate evaporator design. Overall heat transfer coefficient greater than 20,000 W/m^2-K is obtained with a LMTD of 4 °C using aluminum microgroove tubes. A cooling capacity of more than 4 kW is achieved using R134a/water pair with modest pressure drop for both refrigerant and water-side. In a comparison with a commercial plate evaporator, it was seen that five times less surface area was required using microgroove surfaces to achieve same cooling capacity for similar LMTD and mass fluxes. Further, the tubular evaporator was tested with ammonia & ethylene-glycol solution and promising results were obtained. Due to manufacturing limitations for the tubular deign, a flat plate HX containing high aspect ratio microchannel on both sides of the plate was developed. The manifold design has much better potential in terms of design compactness and ability to achieve significantly higher overall higher heat transfer coefficient. To the author's best knowledge, this is the first working prototype based on the manifold microchannel evaporator design, offering record high heat transfer coefficients and low pressure drop penalty compared to the state of the art.

7.2 Recommended future work

Despite promising results obtained using manifold microchannel evaporator, in-depth understanding of the phenomenon is far from well understood. A systematic study of two-phase flow inside the manifold-microchannel channel is needed in order to utilize its full potential. A comprehensive understanding of the two-phase flow regimes with the aid of visualization studies will be critically useful to understand the refrigerant-side fluid flow and heat transfer behavior. To improve the evaporator design, the following future work is recommended:

a) A comprehensive two-phase fluid flow and heat transfer model for a high aspect ratio manifold microchannel system is needed to identify critical parameters influencing the design. The current design utilizes the low mass fluxes and low heat fluxes, which have never been studied in the literature and makes the validation effort difficult.

b) Optimization of the geometrical and flow parameters for better system-level design is required. Due to the large number of parameters influencing the design, optimization becomes challenging, as none of the commercial numerical solvers supports two-phase optimization. A separate study would be required from the first order physics approach to identify the trends that would be most beneficial for the final design.

c) An alternative fabrication method for microgrooved surfaces is needed to obtain accurate and uniform surface. A systematic experimental parametric study would be required for developing the empirical models for both the single-phase and two-phase side. The current fabrication technique using micro deformation has a wide variability in the geometrical dimensions, which makes the experimental study and further comparison quite difficult. MEMS based fabrication technique can be a promising possibility to achieve the desired surfaces.

d) Different manifold geometries should be tested for design enhancements. From the single-phase study, smaller flow area leading to smaller manifold channel width and channel height is preferable. But for two-phase, empirical study would be needed to make a concrete conclusion.

e) The flat microgroove evaporator design needs to be experimentally evaluated in terms of heat transfer coefficient and pressure drop.

Bibliography

[1] BCS, I., US Energy Report, March 2008, "Waste Heat Recovery: Technology and Oppurtunities in U.S. Industry."
[2] UNEP, 2006, "Energy Efficiency Guide for Industry in Asia," p. 183.
[3] Liu, P. K. T., Jan 5, 2006, "Gas Separations using Ceramic Membranes, UNITED STATES DEPARTMENT OF ENERGY."
[4] "Refrigeration and Air Conditioning," IIT Kanpur Lectures.
[5] Herold, K., Radermacher, R., and Klein, S. A., March 18, 1996, Absorption Chillers and Heat Pumps, CRC Press, Inc.
[6] Incropera, F. P., DeWitt, D. P., Bergman, T. L., and Lavine, A. S., April 7, 2006, Fundamentals of Heat and Mass Transfer, Wiley.
[7] Kakaç, S., 1991, Boilers, evaporators, and condensers, Wiley-Interscience.
[8] Schlager, L. M., Pate, M. B., and Bergles, A. E., 1988(a), "Evaporation and condensation of refrigerant-oil mixture in a smooth tube and a micro-fin tube " ASHRAE Trans, 94(1), pp. 149-166.
[9] Shah, 1982, "Chart correlation for saturated boiling heat transfer: equations and further study," ASHRAE Trans, 88, pp. 185-196.
[10] Kandlikar, S. G., 1990, "A General Correlation for Saturated Two-Phase Flow Boiling Heat Transfer Inside Horizontal and Vertical Tubes," Journal of Heat Transfer, 112(1), pp. 219-228.
[11] Eckels, S. J., and Pate, M. B., 1991, "An experimental comparison of evaporation and condensation heat transfer coefficients for HFC-134a and CFC-12," International Journal of Refrigeration, 14(2), pp. 70-77.
[12] Schlager, L. M., Pate, M. B., and Bergles, A. E., November 1989, "Performance of micro-fin tubes with refrigerant R-22 and oil mixtures " ASHRAE Journal, pp. 17-28.
[13] Gungor, K. E., and Winterton, R. H. S., 1986, "A general correlation for flow boiling in tubes and annuli," International Journal of Heat and Mass Transfer, 29(3), pp. 351-358.
[14] McQuinston, F. C., 1978a, "Correlation of heat , mass and momentum transport coefficients for plate-fin-tube heat transfer surfaces with staggered tube," ASHRAE Trans, 84(1), pp. 294-309.
[15] K., F. S., and K., R. C., Aug 1983, "*The Oak Ridge Heat Pump Models: I. A Steady-State Computer Design Model for Air-to-Air Heat Pumps*."
[16] Gray, D. L., and Webb, R. L., "Heat transfer and friction correlations for plate fin-and-tube heat exchangers having plain fins," Proc. 9th International Heat Transfer Conference, pp. 2745-2750.
[17] Sensku, Hatade, and Ishibane, 1979, "Surface heat transfer coefficients of fins used in air cooled heat exchangers," Heat Transfer-Japanese Research 8(8), pp. 16-26.
[18] Arima, H., Kim, J. H., Okamoto, A., and Ikegami, Y., 2010, "Local boiling heat transfer characteristics of ammonia in a vertical plate evaporator," International Journal of Refrigeration, 33(2), pp. 359-370.

[19] Kandlikar, S. G., 2002, "Fundamental issues related to flow boiling in minichannels and microchannels," Experimental Thermal and Fluid Science, 26(2–4), pp. 389-407.
[20] Garimella, S. V., and Sobhan, C. B., 2003, "Transport in microchannels–a critical review," Ann. Rev. Heat Transfer, 13(13), pp. 1-50.
[21] Morini, G. L., 2004, "Single-phase convective heat transfer in microchannels: a review of experimental results," International Journal of Thermal Sciences, 43(7), pp. 631-651.
[22] Thome, J. R., 2004, "Boiling in microchannels: a review of experiment and theory," International Journal of Heat and Fluid Flow, 25(2), pp. 128-139.
[23] Bertsch, S. S., Groll, E. A., and Garimella, S. V., 2008, "Review and comparative analysis of studies on saturated flow boiling in small channels," Nanoscale and Microscale Thermophysical Engineering, 12(3), pp. 187-227.
[24] Kandlikar, S. G., 2006, Heat transfer and fluid flow in minichannels and microchannels, Elsevier Science.
[25] Delphi, "Delphi MCHX Evaporator," http://delphi.com/shared/pdf/ppd/other/mchx-evaporator.pdf.
[26] Kim, M. H., and Bullard, C. W., 2001, "Development of a microchannel evaporator model for a CO2 air-conditioning system," Energy, 26(10), pp. 931-948.
[27] Lee, J., and Mudawar, I., 2006, "Implementation of microchannel evaporator for high-heat-flux refrigeration cooling applications," Journal of electronic packaging, 128(1), pp. 30,31-38.
[28] Yun, R., Hyeok Heo, J., and Kim, Y., 2006, "Evaporative heat transfer and pressure drop of R410A in microchannels," International journal of refrigeration, 29(1), pp. 92-100.
[29] Mongia, R., Masahiro, K., DiStefano, E., Barry, J., Chen, W., Izenson, M., Possamai, F., Zimmermann, A., and Mochizuki, M., "Small scale refrigeration system for electronics cooling within a notebook computer," IEEE, pp. 751-758.
[30] Wadell, R., Joshi, Y. K., and Fedorov, A. G., 2007, "Experimental investigation of compact evaporators for ultralow temperature refrigeration of microprocessors," Journal of Electronic Packaging, 129(3), pp. 1-9.
[31] Cetegen, E., 2010, "Force Fed Microchannel High Heat Flux Cooling Utilizing Microgrooved surfaces," PhD Dissertation, University of Maryland, College Park, College park.
[32] Hrnjak, P. S., and Litch, A. D., 2008, "Microchannel heat exchangers for charge minimization in air-cooled ammonia condensers and chillers," International Journal Of Refrigeration(31), pp. 658-668.
[33] Cao, H., Chen, G., and Yuan, Q., 2009, "Testing and Design of a Microchannel Heat Exchanger with Multiple Plates," Industrial & Engineering Chemistry Research, 48(9), pp. 4535-4541.
[34] Anurjew, E., Hansjosten, E., Maikowske, S., Schygulla, U., and Brandner, J. J., 2011, "Microstructure devices for water evaporation," Applied Thermal Engineering, 31(5), pp. 602-609.

[35] Qi, Z., Zhao, Y., and Chen, J., 2010, "Performance enhancement study of mobile air conditioning system using microchannel heat exchangers," International Journal of Refrigeration, 33(2), pp. 301-312.
[36] Marcinichen, J. B., Thome, J. R., and Michel, B., 2010, "Cooling of microprocessors with micro-evaporation: A novel two-phase cooling cycle," International Journal of Refrigeration, 33(7), pp. 1264-1276.
[37] Harpole, G. M., and Eninger, J. E., "Micro-channel heat exchanger optimization," Proc. Semiconductor Thermal Measurement and Management Symposium, 1991. SEMI-THERM VII. Proceedings., Seventh Annual IEEE, pp. 59-63.
[38] Copeland, D., Behnia, M., and Nakayama, W., 1997, "Manifold microchannel heat sinks: isothermal analysis," Components, Packaging, and Manufacturing Technology, Part A, IEEE Transactions on, 20(2), pp. 96-102.
[39] Kim, Y. H., Chun, W. C., Kim, J. T., Pak, B. C., and Baek, B. J., 1998, "Forced air cooling by using manifold microchannel heat sinks," Journal of Mechanical Science and Technology, 12(4), pp. 709-718.
[40] Poh, S. T., and Ng, E. Y. K., "Heat transfer and flow issues in manifold microchannel heat sinks: a CFD approach," IEEE, pp. 246-250.
[41] Ryu, J. H., Choi, D. H., and Kim, S. J., 2003, "Three-dimensional numerical optimization of a manifold microchannel heat sink," International journal of heat and mass transfer, 46(9), pp. 1553-1562.
[42] Jang, S. P., and Kim, S. J., 2005, "Fluid flow and thermal characteristics of a microchannel heat sink subject to an impinging air jet," Journal of heat transfer, 127(7), pp. 770,771-710.
[43] Jankowski, N. R., Everhart, L., Morgan, B., Geil, B., and McCluskey, P., "Comparing microchannel technologies to minimize the thermal stack and improve thermal performance in hybrid electric vehicles," IEEE, pp. 124-130.
[44] Wang, Y., Ding, G. F., and Fu, S., 2007, "Highly efficient manifold microchannel heatsink," Electronics Letters, 43(18), pp. 978-980.
[45] Wang, Y., and Ding, G. F., 2008, "Numerical analysis of heat transfer in a manifold microchannel heat sink with high efficient copper heat spreader," Microsystem Technologies, 14(3), pp. 389-395.
[46] Xia, G., Liu, Q., Qi, J., and Xu, J., 2008, "Influence of surfactant on friction pressure drop in a manifold microchannel," International Journal of Thermal Sciences, 47(12), pp. 1658-1664.
[47] Haller, D., Woias, P., and Kockmann, N., 2009, "Simulation and experimental investigation of pressure loss and heat transfer in microchannel networks containing bends and T-junctions," International Journal of Heat and Mass Transfer, 52(11-12), pp. 2678-2689.
[48] Kermani, E., Dessiatoun, S., Shooshtari, A., and Ohadi, M. M., "Experimental investigation of heat transfer performance of a manifold microchannel heat sink for cooling of concentrated solar cells," IEEE, pp. 453-459.
[49] Escher, W., Brunschwiler, T., Michel, B., and Poulikakos, D., 2010, "Experimental Investigation of an Ultrathin Manifold Microchannel Heat Sink for Liquid-Cooled Chips," Journal of Heat Transfer, 132(8), pp. 081402,081401-081410.

[50] Sharar, D. J., Jankowski, N. R., and Morgan, B., "Thermal performance of a Direct-Bond-Copper Aluminum Nitride manifold-microchannel cooler," IEEE, pp. 68-73.
[51] Campbell, D. A., and Perkns, H. C., 1968, "Variable property turbulent heat and momentum transfer for air in a vertical rounded corner triangular duct," International Journal of Heat and Mass Transfer, 11(6), pp. 1003-1012.
[52] Shah, R. K., and London, A. L., 1978, Laminar Flow Forced Convection in Ducts: Supplement 1 to Advances in Heat Transfer, Academic Press, New York.
[53] Malák, J., Hejna, J., and Schmid, J., 1975, "Pressure losses and heat transfer in non-circular channels with hydraulically smooth walls," International Journal of Heat and Mass Transfer, 18(1), pp. 139-149.
[54] Altemani, C. A. C., and Sparrow, E. M., 1980, "Turbulent Heat Transfer and Fluid Flow in an Unsymmetrically Heated Triangular Duct," Journal of Heat Transfer, 102(4), pp. 590-597.
[55] Phillips, 1987, "Forced convection, liquid cooled, microchannel heat sinks, MS Thesis," Massachusetts Institute of Technology, Cambridge,MA.
[56] Kays, W. M., and London, A. L., January 1998 Compact Heat Exchangers, Krieger Pub Co.
[57] J., P. R., 1990, Microchannel Heat Sinks", in Advances in thermal modeling of electronic components and system Hemisphere PublishingCorp, New York.
[58] Lazarek, G. M., and Black, S. H., 1982, "Evaporative heat transfer, pressure drop and critical heat flux in a small vertical tube with R-113," International Journal of Heat and Mass Transfer, 25(7), pp. 945-960.
[59] Tran, T. N., Wambsganss, M. W., and France, D. M., 1996, "Small circular- and rectangular-channel boiling with two refrigerants," International Journal of Multiphase Flow, 22(3), pp. 485-498.
[60] Yan, Y.-Y., and Lin, T.-F., 1998, "Evaporation heat transfer and pressure drop of refrigerant R-134a in a small pipe," International Journal of Heat and Mass Transfer, 41(24), pp. 4183-4194.
[61] Bao, Z. Y., Fletcher, D. F., and Haynes, B. S., 2000, "Flow boiling heat transfer of Freon R11 and HCFC123 in narrow passages," International Journal of Heat and Mass Transfer, 43(18), pp. 3347-3358.
[62] Yu, W., France, D. M., Wambsganss, M. W., and Hull, J. R., 2002, "Two-phase pressure drop, boiling heat transfer, and critical heat flux to water in a small-diameter horizontal tube," International Journal of Multiphase Flow, 28(6), pp. 927-941.
[63] Kandlikar, S., and Steinke, M., 2003, "Predicting heat transfer during flow boiling in minichannels and microchannels," ASHRAE Trans, 109(1), pp. 1-9.
[64] Kandlikar, S. G., and Balasubramanian, P., 2004, "An extension of the flow boiling correlation to transition, laminar, and deep laminar flows in minichannels and microchannels," Heat Transfer Engineering, 25(3), pp. 86-93.
[65] Lee, J., and Mudawar, I., 2005, "Two-phase flow in high-heat-flux micro-channel heat sink for refrigeration cooling applications: Part II—heat transfer characteristics," International Journal of Heat and Mass Transfer, 48(5), pp. 941-955.

[66] Lee, J., and Mudawar, I., 2005, "Two-phase flow in high-heat-flux micro-channel heat sink for refrigeration cooling applications: Part I—pressure drop characteristics," International Journal of Heat and Mass Transfer, 48(5), pp. 928-940.
[67] 2001, "Wolverine Tube Inc., Micro Deformation Technology," www.wlv.com.
[68] Association, T. A., 2005, The Aluminum Association. Specifications & Guidelines forAluminum Structures, Arlington, VA.
[69] 1995, "United States Army Corps of Engineers, Engineering and Design,Design of Coastal Revetments, Seawalls and Bulkheads," USACE, Washington DC.
[70] Harirchian, T., and Garimella, S. V., 2011, "Boiling Heat Transfer and Flow Regimes in Microchannels---A Comprehensive Understanding," Journal of Electronic Packaging, 133(1), pp. 011001-011010.
[71] Sozen, A., 2001, "Effect of heat exchangers on performance of absorption refrigeration systems," Energy Conversion and Management, 42(14), pp. 1699-1716.
[72] de Vega, M., Almendros-Ibañez, J. A., and Ruiz, G., 2006, "Performance of a LiBr–water absorption chiller operating with plate heat exchangers," Energy Conversion and Management, 47(18–19), pp. 3393-3407.
[73] Dović, D., Palm, B., and Švaić, S., 2009, "Generalized correlations for predicting heat transfer and pressure drop in plate heat exchanger channels of arbitrary geometry," International Journal of Heat and Mass Transfer, 52(19–20), pp. 4553-4563.
[74] Jeong, J. Y., Hong, H. k., Kim, S. K., and Kang, Y. T., 2009, "Impact of plate design on the performance of welded type plate heat exchangers for sorption cycles," International Journal of Refrigeration, 32(4), pp. 705-711.
[75] Rosa, P., Karayiannis, T. G., and Collins, M. W., 2009, "Single-phase heat transfer in microchannels: The importance of scaling effects," Applied Thermal Engineering, 29(17–18), pp. 3447-3468.
[76] Chiriac, V., and Chiriac, F., "Absorption refrigeration method with alternative water-ammonia solution circulation system for microelectronics cooling," Proc. Thermal and Thermomechanical Phenomena in Electronic Systems (ITherm), 2010 12th IEEE Intersociety Conference on, pp. 1-8.
[77] Khan, T. S., Khan, M. S., Chyu, M.-C., and Ayub, Z. H., 2010, "Experimental investigation of single-phase convective heat transfer coefficient in a corrugated plate heat exchanger for multiple plate configurations," Applied Thermal Engineering, 30(8–9), pp. 1058-1065.
[78] Sui, Y., Teo, C. J., Lee, P. S., Chew, Y. T., and Shu, C., 2010, "Fluid flow and heat transfer in wavy microchannels," International Journal of Heat and Mass Transfer, 53(13–14), pp. 2760-2772.